Master's thesis

NTNU
Norwegian University of Science and Technology
Faculty of Natural Sciences
Department of Materials Science and Engineering

Vilma Helena Erika Kristiansson

# Temperature-dependent carrier lifetime measurements on silicon wafers and bricks

Master's thesis in Innovative Sustainable Energy Engineering (Nordic Master's Programme)
Supervisor: Marisa Di Sabatino (NTNU), Eugen Stamate (DTU), Sune Thorsteinsson (DTU)
Co-supervisor: Alfredo Sanchez Garcia (SINTEF)

June 2023

NTNU
Norwegian University of Science and Technology

Vilma Helena Erika Kristiansson

# Temperature-dependent carrier lifetime measurements on silicon wafers and bricks

Master’s thesis in Innovative Sustainable Energy Engineering (Nordic Master's Programme)
Supervisor: Marisa Di Sabatino (NTNU), Eugen Stamate (DTU), Sune Thorsteinsson (DTU)
Co-supervisor: Alfredo Sanchez Garcia (SINTEF)
June 2023

Norwegian University of Science and Technology
Faculty of Natural Sciences
Department of Materials Science and Engineering

NTNU
Norwegian University of
Science and Technology

# ABSTRACT

This work presents a novel method to measure the temperature-dependent carrier lifetime of crystalline silicon wafers, bricks and ingots. The method uses a BCT-300 from Sinton Instruments paired with a Peltier element connected to a temperature controller. To ensure electrical insulation between the measured sample and the Peltier element a 5 mm thick quartz plate is mounted on the Peltier element.

The BCT-300 instrument allows measurements with the Quasi-Steady-State Photoconductance (QSSPC) technique and transient photoconductance decay technique. The method has been tested in a temperature range of 10-75 °C representing the Nordic climate. The silicon samples measured consist of 4 monocrystalline bricks, 2 multi-crystalline (mc-Si) bricks, 2 mc-Si wafers, and 8 monocrystalline wafers. All samples are p-typed boron doped, except 2 of the monocrystalline wafers that are n-typed phosphorus doped. The results show that the proposed method effectively measures temperature-dependent minority carrier lifetimes higher than 1 $\mu$s within the studied temperature range. The temperature dependence found for most samples aligns with the Shockley-Read-Hall equation under low-level injection conditions. The limitations of the method are related to the physical setup of the BCT-300 instrument and the Peltier element.

The thesis also investigates the temporal stability of stack passivation using a-Si:H/a-$Si_xN_y$:H on two p-type boron-doped monocrystalline wafers through a 10-week study. The first sample, a Czochralski-grown wafer, shows stabilization of the passivation layer after 600 hours with degradation of 50% from the initial carrier lifetime measurement. The second sample, a float zone-produced wafer, shows a continuous decrease in the carrier lifetime through the 10-week period. It is concluded that light-induced degradation, a nonuniform passivation layer and a damaged passivation layer is responsible for the degradation. Lastly, the thesis investigates the possibility of performing temperature-dependent lifetime spectroscopy (TDLS) analysis on the obtained data. Simplifications and assumptions are taken into account while performing this analysis which offers limitations in the accuracy of the obtained results. However, by using the developed method TDLS analysis can be performed.

# SAMMENDRAG

Dette arbeidet presenterer en ny metode for å måle temperaturavhengig ladninsbærer levetid i krystallinske silisium wafere, bricks og ingots. Det eksperimentelle oppsettet består av en BCT-300 ladningsbærer levetidsmåler fra Sinton Instruments sammenkoblet med et Peltier-element og en temperatur kontroll. For å sikre elektrisk isolasjon mellom silisum prøven og Peltier-elementet, er en 5 mm tykk kvartsplate montert på Peltier-elementet.

BCT-300-instrumentet mulligjør to måleteknikker, kvasi-likevektstilstand fotokonduktans (QSSPC) og transient fotokondutans decay. Metoden er testet i et temperaturintervall på 10-75 °C, som representerer det nordiske klimaet. De målte silisiumprøvene inkluderer 4 monokrystallinske bricks, 2 multikrystallinske (mc-Si) bricks, 2 mc-Si-wafere og 8 monokrystallinske wafere. Alle prøvene er p-type, bor-dopet, med unntak av 2 av monokrystallinske wafere som er n-type, forfor-dopet. Resultatene viser at den utviklede metoden effektivt måler temperaturavhengigheten til ladningsbærer levetiden høyere enn 1 $\mu$s innenfor det undersøkte temperaturområdet. Temperaturavhengigheten som ble observert for de fleste prøvene er i samsvar med Shockley-Read-Hall-ligningen under betingelser med lavt injeksjonsnivå. Begrensningene til metoden er knyttet til det fysiske oppsettet til BCT-300-instrumentet og Peltier-elementet.

I tillegg er den tidsmessige stabiliteten til en passivering bestående av a-Si:H/a-$Si_xN_y$:H på to p-typede bor-doped monokrystallinske wafere gjennom en 10-ukers studie undersøkt. Den første prøven, en czochralski silisium wafer viser stabilisering av passiveringslaget etter 600 timer med en degradering på 50% fra den initielle målingen av ladningsbærer levetiden. Den andre prøven, en float-zone silisium wafer, viser en kontinuerlig negang i ladningsbører levetiden gjennom de 10-ukene. Degraderingen som er observert konkluderes å være et resultat av lysindusert nedbrytning, et ikke-uniformt passiveringslag og et skadd passiveringslag.

Avlustende ser arbeitet på muligheten til å utføre en temperaturavhengig levetidsspektroskopi (TDLS) analyse ut fra den oppnådde dataen. Forenklinger og antagelser ble tatt i betraktning under utførelsen av denne analysen. Dette begrenser nøyaktigheten til de oppnådde resultatene. Den utviklede metoden kan brukes til å utføre en TDLS-analyse.

# PREFACE

This master thesis completes my Master of Science degree in the joint Nordic five tech program *Innovative Sustainable Energy Engineering, Solar Cell Systems and Materials* as a collaboration between the Technical University of Denmark (DTU) and the Norwegian University of Science and Technology (NTNU). The thesis is performed in cooperation with SINTEF in Trondheim and is a continuation of the specialization project *Lifetime and resistivity measurements on silicon wafers and bricks* performed in the course TMT4520 during the fall of 2022. The specialization project focused on the effect the sample thickness and passivation had on the carrier lifetime of Czochralski boron-doped monocrystalline silicon samples, and learning the process of resistivity measurements which was crucial to measure accurate carrier lifetime.

The master thesis investigates a method for measuring the carrier lifetime at various temperatures to gain knowledge about the temperature effect on the carrier lifetime. The thesis includes basic knowledge about semiconductor physics chapter 2, charge carrier transport Section 2.2, and experimental details chapter 4. These chapters are partly or entirely based on the work performed through the specialization project. In addition, the master thesis includes a poster presented at *The Norwegian Solar Cell Conference (NSCC) 2023*, attached in Appendix 6.2.

# ACKNOWLEDGEMENTS

This work was performed within the Norwegian Research Center for Sustainable Solar Cell Technology (FME SUSOLTECH, project number 275639/E20). The centre is co-sponsored by the Research Council of Norway and its research and industry partners.

First and foremost I would like to express my gratitude to my main supervisor Prof Marisa Di Sabatino (NTNU) for your excellent guidance, insightful comments, for proofreading, and for being a great mentor.

Secondly, I would like to express my gratitude to my day-to-day co-supervisor Dr. Alfredo Sanchez Garcia (SINTEF). From the very start, you created a safe learning environment and taught me everything about the lab including setting it up. Despite your busy schedule, you were always available with an open door and made time for my endless questions, and series of discussions, helping me with my Python script, and your fine detailed feedback and countless coffee breaks. For this, I am forever grateful.

To my DTU supervisors Eugen Stamate and Sune Thorsteinsson. For always being available online, answering my countless questions and proofreading.

I would also like to thank the N5T for a great experience being both at DTU and NTNU during the 2-year master's degree. These 2 years have been challenging, and full of new experiences and great people.

Lastly, I would like to thank my family for their love, support, patience, and guidance.

# TABLE OF CONTENTS

# LIST OF FIGURES

# LIST OF TABLES

CHAPTER

# ONE

# INTRODUCTION

The consequences the world is facing if the global temperature exceeds the temperature limit of 1.5 °C set by the Intergovernmental Panel on Climate Change (IPCC) can be detrimental [1]. In light of ongoing challenges such as the energy crisis and population growth, the demand for energy continues to escalate. The Energy Information Administration (EIA) projects a nearly 50% increase in world energy consumption by 2050 due to population growth and an increase in standards of living in non-Organization for Economic Cooperation and Development (OECD) countries [2]. The situation today where most of the world's energy needs are met by fossil fuels, whose energy conversion results in greenhouse gas (GHG) emissions contributes to global warming [3]. For these reasons, the need for renewable sources of energy and utilization technologies is essential.

Through the European Economic Area (EEA) Norway is committed to be *Determined to preserve, protect and improve the quality of the environment and to ensure prudent and rational utilization of natural resources on the basis, in particular, of the principle of sustainable development, as well as the principle that precautionary and preventive action should be taken* [4]. Consequently, Norway, along with other nations worldwide, is actively transitioning away from fossil fuel-based energy systems. By doing so, the energy mix that today consists of 81% (2021) fossil fuels (when 5% nuclear is counted as sustainable energy) will become greener [5]. This however requires reducing the costs of renewable energy sources and simultaneously increasing their efficiencies.

A renewable energy source that is expected to be one of the most important contributors is solar energy. Solar energy is seen as one of the fastest-growing energy sources between 2018-2050 together with wind and hydroelectric power [5]. Solar energy is abundant, free and available everywhere. Through the photovoltaic (PV) effect it is possible to convert sunlight directly to electricity to power devices [6]. The PV energy sector is rapidly growing by more than 40% per year since the beginning of 2000 with a current (2022) global capacity of 940 $GW_p$ [7, 8]. Photovoltaic energy has a great number of advantages, however, the limitations

are mainly related to efficiency as this property is a compromise between cost, material, and efficiency [9]. Other challenges are mainly related to maintenance, energy storage, and weather dependencies [9]. The trend observed in the PV market is a continuation of a price reduction of the price of PV modules [8].

Silicon solar cells are today a mature technology with the highest reaching efficiency being 26.8% for the single crystal (non-concentrator) silicon solar cells [10]. The maximum efficiency a single homojunction silicon solar cell can reach is approximately 32% [11]. The most important photovoltaic material today is silicon which makes up 95% of all solar cell material used. One of the reasons for this extensive use of silicon can be explained through its abundance in silicon oxide ($SiO_2$) which makes up 27.7% of the earth's crust [3, 12].

## 1.1 Motivation

Solar cell efficiency is essentially the most important factor for assessing quantitatively the quality of solar cells. The quality of the solar cell is directly dependent on the quality of the material [9]. To increase the efficiency of a solar cell it is important to understand the parameters influencing the efficiency of the material. Solar cells are sensitive to temperature and suffer from recombination losses, ohmic resistance losses, shadowing losses etc [9]. The effect of an increase in temperature is observed to have a direct negative effect on both the efficiency and power output of the solar cell [13]. This can be observed in Figure 1.1 where increased temperature results in a linear decrease in the efficiency for several PV technologies. This phenomenon can be attributed to the accelerated rate of recombination processes that occur at elevated temperatures [13]. A decrease in solar cell efficiency corresponds to a decrease in the power output of the solar cell.

To assess the quality and efficiency of a solar cell, or a solar cell material, the carrier lifetime can be measured. A high carrier lifetime is associated with high efficiency and vice versa [14]. The carrier lifetime represents the time it takes for a charge carrier, a hole or an electron, to recombine [9]. This parameter depends on various factors such as impurity concentration and defects in the material. Impurities and defects have a detrimental influence on the carrier lifetime. The decay of charge carriers through defect states in the material is commonly known as the Shockley-Read-Hall (SRH) recombination mechanism and is dominant in silicon [14].

In monocrystalline silicon samples defects are most likely to occur at the surface of the sample due to abrupt discontinuities in the crystal structure seen by the edges of the surface or grain boundaries. These abrupt discontinuities represent unbonded or partially bonded atoms also referred to as dangling bonds [14]. The unbonded atoms introduce vacant positions in the lattice where unwanted vacancy atoms or extrinsic impurities from the environment can connect to the material [9]. Consequently, these impurities introduce energy levels within the band gap, acting as trap states or recombination centres that have a detrimental impact on both efficiency and carrier lifetime [14].

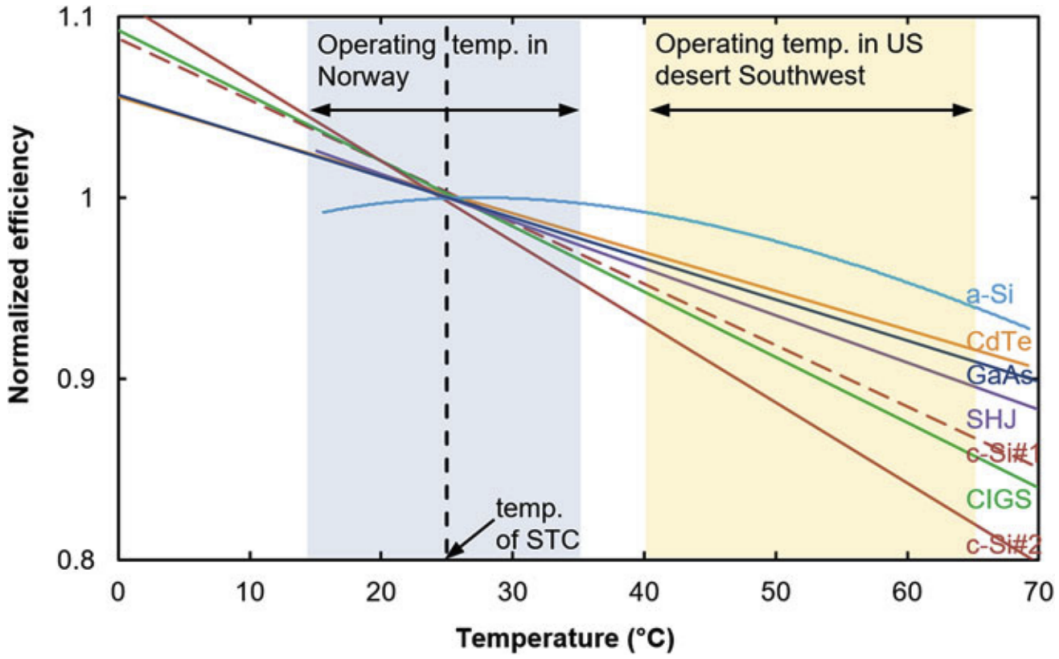


**Figure 1.1:** Normalized efficiency as a function of operating temperature for various PV-cell technologies. The figure illustrates a decrease in efficiency with an increase in temperature [13].

The carrier lifetime can be measured through various techniques, two of these are the quasi-steady-state photoconductance (QSSPC) technique and the transient photoconductance decay (PCD) method, first described by Sinton et. al in 1996 [14, 15]. The QSSPC regime is used for materials with low carrier lifetimes, while the PCD method is used for materials with high carrier lifetimes.

To better understand the temperature effects on the carrier lifetime, this thesis develops a method for measuring the carrier lifetime at various temperatures. Samples of different ingots, doping and crystal structures will be measured. To ensure that the method developed in this thesis can be utilized at a later time, there will be multiple measurements on chosen samples to ensure that results are reproducible. Through these measurements and focus areas, the thesis will answer the following research question:

- Is the carrier lifetime in mono and multi-crystalline silicon samples influenced differently by temperature and is the temperature effect more significant in one sample than the other?
- What is the temporal stability of the stack passivation of a-Si:H and a-$SiN_x$:H and how does the passivation performance differ ten weeks after initial testing?
- Through temperature-dependent lifetime spectroscopy, can we from the developed model gain information about the defect level in the materials?

The thesis is a continuation of a 15 ECTS specialization project report, part

of the course TMT4520. The focus area of the specialisation project *Lifetime and resistivity measurements on silicon wafers and bricks* was to learn the working principles of the Sinton Instrument BCT-300 and how to perform four-point probe measurements on different samples. In addition, the influence of the sample thickness of wafers and bricks (164 $\mu$m - 1 cm), passivated and unpassivated wafers, on the carrier lifetime was investigated [16].

CHAPTER

# TWO

# THEORY

## 2.1 Basic semiconductor physics

This chapter aims at providing the reader with the necessary theoretical background to understand the measurements, results, and discussion in the later chapters. The most important concepts on basic semiconductor physics are provided in the following chapters, however, more thorough information is given as part of the specialization project report, attached in Appendix 6.2.

A semiconductor is suitable for use in solar cells due to its properties. These include the ability to absorb visible light, and the band gap between initial, occupied, and unoccupied states which are involved in the absorption of photons, seen in Figure 2.1 [9]. Insulators and metals also have bandgaps however the distance between the lowest energy level that can accept an electron (Lowest Unoccupied Molecular Orbital - LUMO) and the highest energy level containing valence electrons (highest occupied molecular orbital - HOMO) is too long or overlapping [18]. The distance between the HOMO and LUMO plays a fundamental role in determining the wavelength and intensity of light absorption [18]. The efficiency of the solar cell is directly related to the bandgap and the maximum efficiency is seen at a band gap width of 1.4 eV. The efficiency is also dependent on the incident photon energy as shown in Equation 2.1 [9].

$$E_{\mathbf{ph}} = \frac{hc}{\lambda}, \tag{2.1}$$

where $E_{\mathbf{ph}}$ [eV] is the photon energy, $h$ is the Planck constant [eVs], $c$ [m/s] is the speed of light, and $\lambda$ [nm] is the wavelength of the incident light [9].

The lowest unoccupied band is the *conduction band* (CB) and the highest occupied band is commonly known as the *valence band* (VB). The VB edge ($E_{\mathrm{V}}$) and the CB edge ($E_{\mathrm{C}}$) are separated by a band gap: $E_{\mathrm{g}} = E_{\mathrm{C}} - E_{\mathrm{V}}$, in which electrons are not able to populate [9]. The reason is that there are no energy

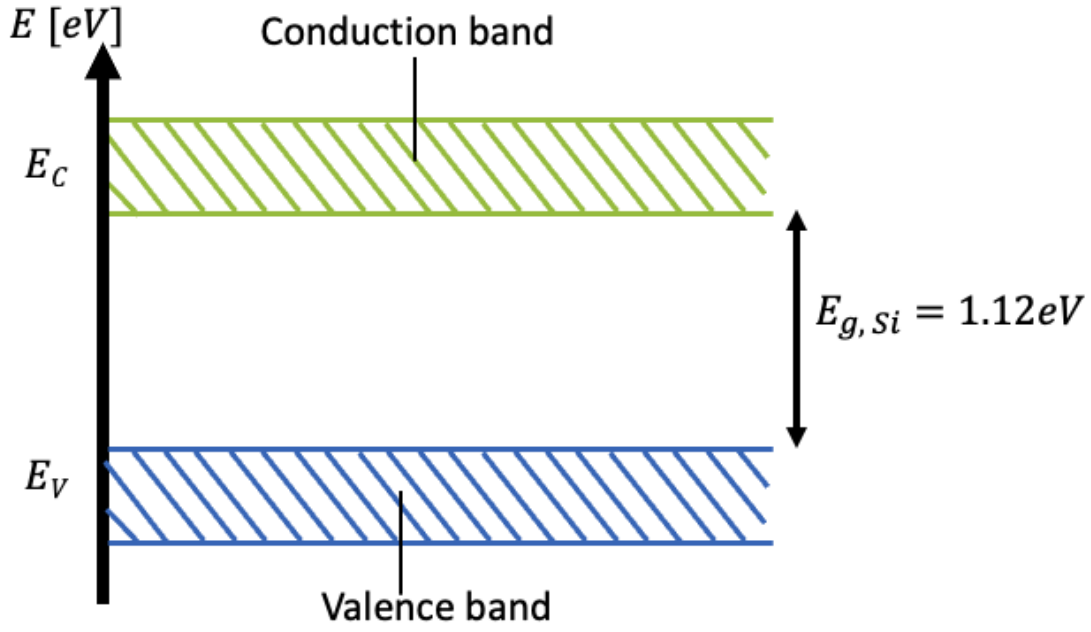


**Figure 2.1:** The figure illustrates the silicon energy band diagram where $E_{\mathrm{C}}$ and $E_{\mathrm{V}}$ are energy levels of the conduction band and valence band respectively The energy bands are separated by the forbidden band gap $E_{\mathrm{g}}$. The band gap energy or the width of the forbidden band is $E_{\mathrm{g}} = 1.12$ [eV] for silicon [17].

levels within the band gap of an intrinsic semiconductor, meaning that there are no electrons present. To promote an electron from the VB to the CB energy equal to or larger than the band gap is required. The excess energy generated from the promotion of the electron is converted into electrical energy, commonly known as the photovoltaic effect (PE) [9]. Materials that require momentum together with a photon in order to promote an electron from the VB to the CB are commonly known as indirect band gap materials. In these materials, the CB minimum and the VB maximum occur at different wave number values (k). In direct band gap materials, the VB maximum and the CB minimum occur at the same wave number value and only a photon is needed to promote the electron from the VB to the CB [9].

The properties of a semiconductor can be tailored by means of their electrical and conductive properties and for more efficient transport of charges. This can be achieved through the addition of an atom with a higher valence number by adding, for instance, phosphorus which has five valence electrons. This is commonly referred to as donor doping as electrons are the majority carrier in the material and donate away the excess electron. Another possible way to dope the semiconductor material is by adding a material with a lower valence number. This can be achieved by adding for instance boron which has three valence electrons. The addition of a lower valence atom is commonly referred to as acceptor doping as electrons are accepted to the empty positively charged position in the outer shell of silicon. The absence of an electron is treated as a particle known as a hole. More information on semiconductor doping is elaborated in Appendix 6.2 section 2.2.

In thermal equilibrium (T=0K) the VB states are occupied and the CB states are unoccupied, as all electrons are involved in bonding. For this reason, they do not conduct heat or electricity easily [9]. The probability of allowed electron states at a given energy level $E$ in thermal equilibrium can be described through the Fermi-Dirac (F-D) distribution presented in Equation 2.2.

$$f(E) = \left[1 + \exp\left(\frac{E - E_{\mathrm{F}}}{k_{\mathrm{B}}T}\right)\right]^{-1}, \tag{2.2}$$

where $E_{\mathrm{F}}$ [eV] is the Fermi energy, $k_{\mathrm{B}}$ [eV/K] is Boltzmann's constant and $T$ [K] is the absolute temperature. To calculate the densities of electrons and holes in the CB and the VB, respectively, at thermal equilibrium Equation 2.3 and Equation 2.4 can be used for electrons and holes respectively [9].

$$n_0 = N_{\mathrm{C\,exp}}\left(\frac{E_{\mathrm{F}} - E_{\mathrm{C}}}{k_{\mathrm{B}}T}\right), \tag{2.3}$$

$$p_0 = N_{\mathrm{V\,exp}}\left(\frac{E_{\mathrm{V}} - E_{\mathrm{F}}}{k_{\mathrm{B}}T}\right). \tag{2.4}$$

Equation 2.3 and Equation 2.4 show that $n_0$ [$\mathrm{cm}^{-3}$] and $p_0$ [$\mathrm{cm}^{-3}$] strongly depend on both the Fermi level and the temperature [9]. $N_{\mathrm{C}}$ [$\mathrm{cm}^{-3}$] in Equation 2.3 and $N_{\mathrm{V}}$ [$\mathrm{cm}^{-3}$] in Equation 2.4 denote the effective density of state in the CB and VB, respectively. These values can be calculated through Equation 2.5 [9].

$$N_{\mathrm{C/V}} = 2\left(\frac{m^*_{\mathrm{e/h}} k_{\mathrm{B}} T}{2\pi\hbar^2}\right)^{\frac{3}{2}}, \tag{2.5}$$

where $m^*_{\mathrm{e/h}}$ [-] are the effective masses of electrons (e) and holes (h) respectively, and $\hbar$ [Js] is the reduced Planck constant. The equations above, 2.2-2.5, indicate that the product of the $n_0$ and $p_0$ is constant for any given material at a given temperature and is independent of $E_{\mathrm{F}}$ [9]. This is the intrinsic carrier density, $n_{\mathrm{i}}$ and equals the equilibrium concentrations of electrons and holes, expressed in Equation 2.6, commonly known as the law of mass action [9].

$$n_0 p_0 = N_{\mathrm{C}} N_{\mathrm{V}} exp\left(-\frac{E_{\mathrm{gap}}}{k_{\mathrm{b}}T}\right) = n_{\mathrm{i}}^2. \tag{2.6}$$

## 2.2 Generation and Recombination

When light is incident on a semiconductor material, the electrons absorb light as photons and are excited from the VB to the CB. Simultaneously a hole in the CB is promoted to the VB and an electron hole (e-h) pair is generated. Generation is seen as a process that increases the number of charge carriers in the semiconductors [14].

The opposite process of generation is recombination. The recombination process takes place as a spontaneous transition of an excited electron from the CB to an unoccupied state, a hole, in the VB. Therefore this process is referred to as recombination. Here an e-h pair is annihilated. This process decreases the number of charge carriers in the semiconductor. Recombination is one of the major limiting factors on solar cell efficiency and is therefore important to investigate.

The recombination rate ($R$, [$\mathrm{cm^{-3}s^{-1}}$]) and the generation rate (G, [$\mathrm{cm^{-3}s^{-1}}$]) are proportional to each other. This proportionality is based on the probability of an electron moving from the CB to the VB, through the F-D distribution. In thermal equilibrium, the thermal generation rate ($G_0$, [$\mathrm{cm^{-3}s^{-1}}$]) and the recombination rate ($R_0$, [$\mathrm{cm^{-3}s^{-1}}$]) are balanced [14]. When a system is exposed to constant light, it reaches a new stationary state where the generation rate exceeds the equilibrium generation rate and the total recombination rate exceeds the equilibrium recombination rate. When the light is turned off, the system tries to return to equilibrium. The excess electron and hole densities ($\Delta n$ and $\Delta p$) therefore decay at a net recombination rate ($U$ [$\mathrm{cm^{-3}s^{-1}}$]) which is equal to the recombination rate minus the equilibrium recombination rate or the generation rate minus the recombination rate ($\Delta U = R - R_0 = G - R$ [$\mathrm{cm^{-3}s^{-1}}$]) [14]. Assuming the material remains in charge neutrality and free of trapping centres ($\Delta n$ = $\Delta p$), the time dependence of $\Delta n$ can be expressed through Equation 2.7 [14].

$$\frac{\mathrm{d}\Delta n(t)}{\mathrm{d}t} = -U\left(\Delta n(t), n_0, p_0\right). \tag{2.7}$$

In thermal equilibrium, the net recombination rate can be represented as a polynomial in ($\Delta n$, [$\mathrm{cm^{-3}}$]), with the zero-order coefficient equal to zero, as $U$ must equal zero at ($\Delta n$=0). Hence, the time-dependent decay of the excess carrier density ($\Delta n$) follows an exponential decay, which can be shown through a Taylor function. By setting the recombination rate $U(\Delta n)$ as a function where $\Delta n$ is a function of the excess carrier density, the Taylor expansion will take the following form.

$$U(\Delta n) \approx U(\Delta n = 0) + \left.\frac{\partial U}{\partial \Delta n}\right|_{\Delta n=0} \Delta n + O(\Delta n^2), \tag{2.8}$$

where $U(\Delta n = 0) = O$, therefore

$$U(\Delta n) \approx \left.\frac{\partial U}{\partial \Delta n}\right|_{\Delta n=0} \Delta n = \alpha \times \Delta n, \tag{2.9}$$

where $\alpha = \frac{\partial U}{\partial \Delta n}|_{\Delta n=0}$ is a constant. Then, using equation Equation 2.9 the time decay of $\Delta n$ can be expressed as follows.

$$\frac{\mathrm{d}}{\mathrm{d}t}\Delta n = -U(\Delta n, n_0, p_0) = -\alpha \Delta n. \tag{2.10}$$

By inserting Equation 2.9 as $\frac{\mathrm{d}\Delta n}{\Delta n} = -\alpha dt$ in Equation 2.10, with the expo-

nential decay of $\Delta n$ can be derived by integration between 0&$t$:

$$\int_{\Delta n(t=0)}^{\Delta n(t)} \frac{\mathrm{d}\Delta n}{\Delta n} = -\alpha \int_0^t \mathrm{d}t, \tag{2.11}$$

By integrating Equation 2.11 the following expression is obtained.

$$\log \frac{\Delta n(t)}{\Delta n(0)} = -\alpha t, \tag{2.12}$$

and therefore

$$\Delta n(t) = \Delta n(0) e^{-\alpha t}. \tag{2.13}$$

The $\alpha$ [1/s] in Equation 2.11-2.13 represents the time constant of exponential decay. The recombination lifetime ($\tau$ [s]), commonly referred to as the lifetime or carrier lifetime, is dependent on the excess carrier density and can be expressed through Equation 2.14 [14].

$$\tau(\Delta n, n_0, p_0) = \frac{\Delta n}{U(\Delta n, n_0, p_0)}. \tag{2.14}$$

The recombination processes are categorized into intrinsic and extrinsic mechanisms. Intrinsic mechanisms are inherent to all crystal types and are caused by band-to-band (btb) transitions. They include radiative recombination ($U_{\mathrm{Rad}}$ [$\mathrm{cm^{-3}s^{-1}}$]), where excess energy is released as a photon seen as (1) in Figure 2.2, and Auger btb recombination ($U_{\mathrm{Auger}}$), where excess energy is transferred to a third carrier, seen as (2) in Figure 2.2. The extrinsic mechanism depends on the concentration of impurities and dislocations present in the material. The decay of electrons from the CB to the VB takes place as a step-wise transition via a defect centre with an intermediate energy level in the band gap. This recombination mechanism is commonly known as Shockley-Read-Hall, and the recombination rate is denoted as $U_{\mathrm{SRH}}$, seen as (3) in Figure 2.2. The intrinsic and extrinsic recombination mechanisms are often used to express the bulk lifetime $\tau_{\mathrm{bulk}}$ [s] shown in the following equation [9].

$$\frac{1}{\tau_{\mathrm{bulk}}} = \frac{1}{\tau_{\mathrm{Auger}}} + \frac{1}{\tau_{\mathrm{Rad}}} + \frac{1}{\tau_{\mathrm{SRH}}}, \tag{2.15}$$

where $\tau_{\mathrm{Auger}}$, $\tau_{\mathrm{Rad}}$, and $\tau_{\mathrm{SRH}}$ [s] are the lifetimes associated with the Auger, radiative, and SRH recombination mechanisms, respectively, given in Equation 2.14. The SRH mechanism dominates in silicon; however, with increasing temperature or in heavily doped silicon, the Auger mechanism becomes dominant. As silicon is an indirect bandgap material, the radiative mechanism is not relevant in silicon [17].

The effective carrier lifetime, $\tau_{\mathrm{eff}}$ [s], combines the bulk and surface recombination, $\tau_{\mathrm{surf}}$ [s], through Equation 2.16. Surface recombination can be viewed as a two-dimensional case of SRH taking place on the surface of the material, this is further covered in Section 2.2.3.

$$\frac{1}{\tau_{\mathrm{eff}}} = \frac{1}{\tau_{\mathrm{bulk}}} + \frac{1}{\tau_{\mathrm{surf}}}. \tag{2.16}$$

In the limiting cases of high or low recombination rates the bulk lifetime seen in Equation 2.16 can be simplified to Equation 2.17 [14]. The surface recombination velocity can be derived through the time-dependent equation for excess carrier density given in Equation 2.14. The surface recombination velocity is expressed as $S = U/\Delta n$, and the distance the carrier has to pass to recombine is the diffusion length, $L_j$ (where j=p, n for holes and electrons, respectively). The length the carriers have to pass before they recombine depends on the thickness of the sample. The diffusion length can be expressed as $L = \sqrt{D_j \tau_j}$. The effective lifetime can be expressed as follows.

$$\frac{1}{\tau_{\text{eff}}} = \frac{1}{\tau_{\text{bulk}}} + \frac{2S_{\text{eff}}}{W}. \tag{2.17}$$

where $W$ [cm] is the wafer thickness and $S_{\text{eff}}$ [cm/s] is the effective surface recombination. Equation 2.17 shows that with a low bulk recombination lifetime, surface recombination will be dominant and vice versa [14]. The derivation of Equation 2.17 can be found in [19].

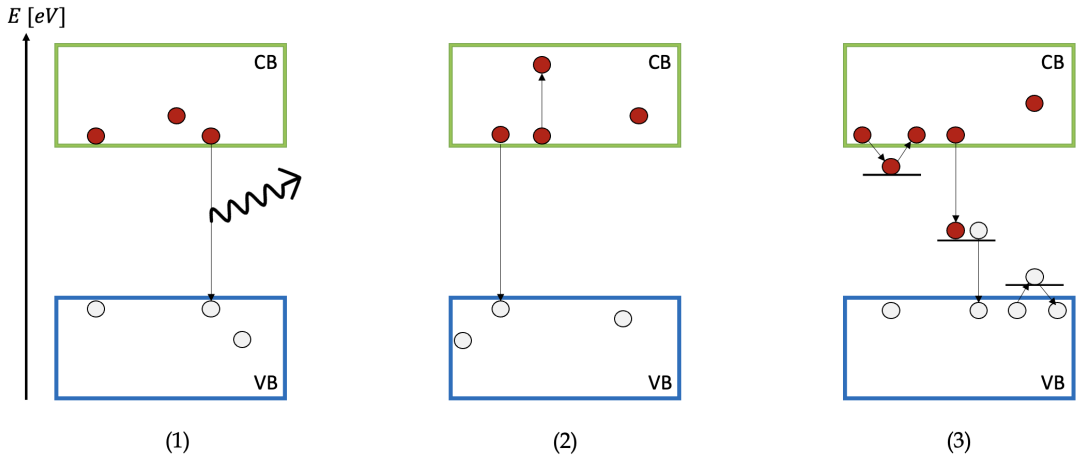


**Figure 2.2:** In the figure, the CB is represented by the colour green, the VB by the colour blue, electrons by red circles, and holes by white circles. The main recombination mechanisms are illustrated as follows: (1) radiative btb, (2) Auger, and (3) SRH recombination. The illustration of the SRH recombination (3) also includes the process of electron and hole trapping and de-trapping near the CB and the VB, respectively, and will be further elaborated in Section 2.2.2.

### 2.2.1 Intrinsic recombination mechanisms

The two intrinsic recombination mechanisms are radiative btb recombination and Auger btb recombination. Radiative btb recombination refers to the release of a photon due to excess energy, as illustrated in Figure 2.2 (1). It is dominant in direct-band-gap materials as it occurs directly from band to band. For this reason, the radiative btb is not the primary recombination mechanism in silicon-based semiconductors. The rate $U_{\text{rad}}$ at which radiative recombination occurs depends on the concentration of free electrons and holes [14]. This is described by Equation 2.18.

$$U_{\text{rad}} = B_{\text{rad}}(np - n_{\text{i}}^2), \tag{2.18}$$

where $B_{\text{rad}}$ [$\text{cm}^{-3}\text{s}^{-1}$] represents the radiative recombination coefficient, which denotes the probability of a radiative transition occurring. This coefficient is a material property that depends on the band structure of the semiconductor [9].

Auger recombination refers to the case when excess energy from a decaying carrier is transferred to a third carrier, illustrated in Figure 2.2 (2). The Auger recombination is dominant in materials with high carrier densities or at high temperatures as a result of increasing thermal excitation [9]. The rate of this mechanism depends on the densities of all involved carriers and the net rate for the two-electron and one-hole (eeh-process) and two holes and an electron (ehh-process) process. The net recombination rate, $U_{\text{Auger}}$, of these processes is given in Equation 2.19 and is given as the product of the concentrations of the carriers involved [9]. Auger recombination can take place in indirect band gap materials and is considered the most dominant loss mechanism in very pure silicon and germanium [9].

$$U_{\text{Auger}} = C_{\text{n}}(n^2p - n_0^2p_0) + C_{\text{p}}(np^2 - n_0p_0^2), \tag{2.19}$$

where $C_{\text{n}}$ and $C_{\text{p}}$ [$\text{cm}^6\text{s}^{-1}$] are Auger coefficients of the eeh- and ehh-processes, respectively.

### 2.2.2 The extrinsic recombination mechanism Shockley-Read-Hall

The extrinsic recombination mechanism takes place as the decay of an e-h pair occurs as a step-wise transition involving a defect centre with an intermediate energy level within the band gap [14]. This recombination mechanism is known as SRH recombination and is illustrated as (3) in Figure 2.2 [20].

In silicon semiconductors, SRH is the dominant recombination mechanism due to the presence of impurities in the crystal structure. These impurities create energy levels in the bandgap that act as trap states or recombination centres when located in the forbidden [9, 14]. The defect energy level and its location within the band gap have a significant influence on the recombination rate of the charge carrier. When the defect level is close to the CB edge, the probability of the electron being re-emitted to the CB is higher than the probability of combining with a hole coming from the VB into the same energy level. This can be attributed to the fact that the trap level is closer to the CB than the VB, which facilitates the re-emission of the electron from the trap level to the CB while increasing the energy barrier for hole capture from the VB. Consequently, defect energy states that are deeply situated within the band gap have more influence on the carrier lifetime than the shallow defects [14].

Defect levels, as displayed in Figure 2.3, can be either occupied or unoccupied. An occupied defect level can either excite an electron to the CB (1) or capture a

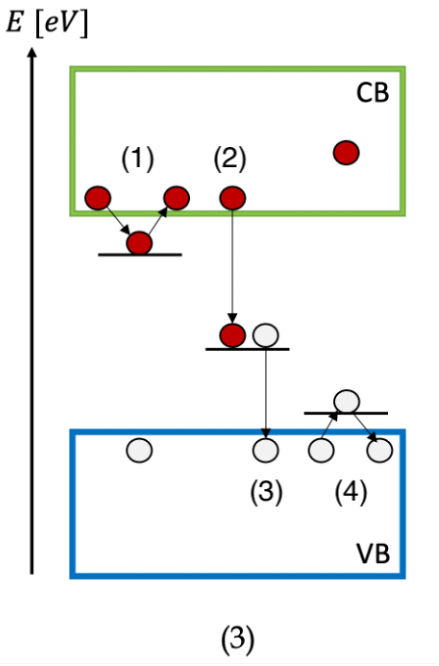


**Figure 2.3:** SRH recombination shown as (3) from Figure 2.2. The figure illustrates occupied and unoccupied defect levels as part of the step-wise transition that takes place when carriers recombine. An occupied defect level can excite an electron to the CB (1) or capture a hole from the VB (4). An unoccupied defect level can capture an electron from the CB (2) or emit a hole into the VB (3) [14].

hole from the VB (4), as illustrated in Figure 2.3. An unoccupied defect level can either capture an electron from the CB (2) or emit a hole into the VB (3) seen in Figure 2.3 [14]. The interactions between the defects and the CB and VB can result in three distinct processes: recombination centre, generation centre, and trap centre [14].

SRH is the most important recombination mechanism in silicon and will for this reason be derived in the following. The net generation and recombination rate of holes and electrons are dependent on the emission and capture rates ($c_p^*$ and $c_n^*$) of holes and electrons. The capture rates for holes and electrons are expressed in Equation 2.20 [14].

$$c_p^* = c_p p = \sigma_p \nu_{th} p, \quad c_n^* = c_n n = \sigma_n \nu_{vt} n. \tag{2.20}$$

The probability of an electron occupying a defect state is given by the product $N_\mathrm{t} \times f_\mathrm{t}$, where $N_\mathrm{t}$ is the density of defect centres, and $f_\mathrm{t}$ is the probability of occupation by an electron, which is determined by the Fermi-Dirac distribution function (Equation 2.2). The total electron emission (or total hole capture) is directly proportional to the density of occupied defect centres, as only occupied states can emit an electron or capture a hole. Conversely, for total electron capture (or hole emission), only one electron can be captured and occupy a single defect state, and the state must be unoccupied. Therefore, the probability of an electron not occupying the defect state is given by $1 - f_\mathrm{t}$. The changes in hole and electron concentrations over time as a result of generation and recombination processes,

can be expressed by the following equations, respectively.

$$\left(\frac{\mathrm{d}p}{\mathrm{d}t}\right)_{\mathrm{GR}} = e_{\mathrm{p}} \times N_{\mathrm{t}} f_{\mathrm{t}} - c_{\mathrm{n}} n \times N_{\mathrm{t}}(1 - f_{\mathrm{t}}), \tag{2.21}$$

$$\left(\frac{\mathrm{d}n}{\mathrm{d}t}\right)_{\mathrm{GR}} = e_{\mathrm{n}} \times N_{\mathrm{t}}(1 - f_{\mathrm{t}}) - c_{\mathrm{p}} n \times N_{\mathrm{t}} f_{\mathrm{t}}. \tag{2.22}$$

By isolating the emission rates from Equations 2.22 and 2.21, they can be expressed as functions of the defect energy $E_{\mathrm{t}}$ and the capture coefficients $c_{\mathrm{n}}$ for electrons and $c_{\mathrm{p}}$ for holes, as expressed in Equation 2.23 and Equation 2.24, respectively. Under equilibrium conditions, where the rate of generation and recombination are equal, the net recombination and generation are zero. By using $U_{\mathrm{SRH}} = \left(\frac{\mathrm{d}n}{\mathrm{d}t}\right)_{\mathrm{GR}} = \left(\frac{\mathrm{d}p}{\mathrm{d}t}\right)_{\mathrm{GR}}$, it is possible to derive expressions for the emission rates of electrons and holes, denoted as $e_{\mathrm{n}}$ and $e_{\mathrm{p}}$ respectively, are expressed in the following equations.

$$e_{\mathrm{n}} = c_{\mathrm{n}} n \frac{1 - f_{\mathrm{t}}}{f_{\mathrm{t}}} = c_{\mathrm{n}} N_{\mathrm{C}} \exp(-\frac{E_{\mathrm{C}} - E_{\mathrm{t}}}{k_{\mathrm{B}} T}) = c_{\mathrm{n}} n_1, \tag{2.23}$$

$$e_{\mathrm{p}} = c_{\mathrm{p}} p \frac{f_{\mathrm{t}}}{1 - f_{\mathrm{t}}} = c_{\mathrm{p}} N_{\mathrm{C}} \exp(-\frac{E_{\mathrm{t}} - E_{\mathrm{V}}}{k_{\mathrm{B}} T}) = c_{\mathrm{p}} p_1, \tag{2.24}$$

where $n_1$ and $p_1$ are the SRH densities for electrons.

Under steady-state conditions, the time rates of change of electrons $\mathrm{d}n/\mathrm{d}t = 0$ and the time rates of change of holes $\mathrm{d}p/\mathrm{d}t = 0$, therefore they are equal. By inserting Equation 2.23 and Equation 2.24 into Equation 2.21 and Equation 2.22, respectively, The probability of occupation, $f_t$, of the defect centres as a function of time can be determined through $\mathrm{d}n/\mathrm{d}t = \mathrm{d}p/\mathrm{d}t$. If this expression is inserted in either Equation 2.21 or Equation 2.22 the net recombination rate $U_{\mathrm{SRH}}$ [$\mathrm{cm}^{-3}\mathrm{s}^{-1}$] for SRH recombination through defects can be expressed through the following equation.

$$U_{\mathrm{SRH}} = \frac{(np - n_{\mathrm{i}}^2)}{[N_{\mathrm{t}}\sigma_{\mathrm{n}}\nu_{\mathrm{th}}]^{-1}(p + p_1) + [N_{\mathrm{t}}\sigma_{\mathrm{p}}\nu_{\mathrm{th}}]^{-1}(n + n_1)}. \tag{2.25}$$

By inserting Equation 2.25 into Equation 2.14, it is possible to derive an expression for the SRH lifetime. The derivation of this equation assumes that carrier trapping can be neglected meaning that $\Delta n = \Delta p$. The non-equilibrium densities of electrons and holes are equal to $n = n_0 + \Delta n$ and $p = p_0 + \Delta p$. Through this, the expression for the SRH lifetime, $\tau_{\mathrm{SRH}}$ [s], in Equation 2.26 is derived.

$$\tau_{SRH} = \frac{\tau_{\mathrm{n0}}(p_0 + p_1 + \Delta n) + \tau_{\mathrm{p0}}(n_0 + n_1 + \Delta n)}{p_0 + n_0 + \Delta n}, \tag{2.26}$$

where $\tau_{\mathrm{n0}}$ [s] and $\tau_{\mathrm{p0}}$ [s] are the capture time constants of electrons and holes, respectively [9].

### 2.2.3 Surface recombination through defects

In mono- and multi-crystalline silicon (mc-Si), defects are most frequently found on the surface edges and at grain boundaries respectively. The reason for this is the presence of partially bonded Si-atoms at the silicon surface edge and in the grain boundaries present in the material. This creates an abrupt discontinuity in the crystal structure with unbonded atoms [9, 14]. The presence of unbonded atoms is higher in mc-Si compared to monocrystalline silicon. The density of recombination-active defect levels near the semiconductor surface is increased as a result of the unbonded atoms. These unbonded atoms represent areas in which environmental impurities can connect to the material. These impurities act as trapping centres or recombination centres [14].

The recombination rate at the surface is often described by the surface recombination velocity (SRV). The SRV can be calculated for both electrons, $S_{\mathrm{n}}$, and holes, $S_{\mathrm{p}}$, [cm/s], as expressed in Equation 2.27 [9].

$$S_j = B_j N_s, \tag{2.27}$$

where $j = n, p$ for electrons and holes respectively, $\mathrm{B}_j$ is a coefficient given by $B_j = \nu_j \sigma_j$ where $\nu_j$ ia th thermal velocity of the carrier and $\sigma_j$ is the capture cross-section of the carrier, and $N_s$ [$\mathrm{cm}^{-3}$] is the density of traps per unit area. The SRV is limited by the thermal energy, and at higher temperatures, the SRV increases. The reason for this is attributed to the increased diffusion of carriers to the surface at higher temperatures [14]. The SRV is expressed as the surface recombination rate, $\mathrm{U}_s$ [$\mathrm{cm}^{-2}\mathrm{s}^{-1}$], divided by the carrier density, $\Delta n$, shown in Equation 2.28 [14].

$$S \equiv \frac{U_s}{\Delta n}. \tag{2.28}$$

Surface recombination can be seen as a two-dimensional case of SRH. One way to reduce surface recombination is through passivation which is a process that saturates the unbonded Si-atoms and reduces the number of energy states in the bandgap, resulting in longer carrier lifetimes [9]. This will be further explained in Section 2.2.3.

#### Reduction of surface recombination

The primary limiting factor in the performance of today's crystalline silicon solar cells is recombination at the cell surfaces and contacts [9]. In the case of high surface recombination velocity at the silicon surface, a dead layer is created where the photogenerated carriers are not collected [9]. To avoid carriers recombining at the surface, and reducing the recombination velocity, a thin layer of a wide bandgap insulator material can be applied on the surface. This applied layer saturates the unbonded atoms and other recombination active bonds at the surface which prevents the carriers from reaching the surface and recombining. This is referred to

as surface passivation. Through surface passivation, the SRV is reduced, resulting in higher measured lifetimes compared to unpassivated (untreated) surfaces [9]. This means that the quality of passivation can be investigated through the SRV. If the surface passivation is of high quality, the effective lifetime $\tau_{\text{eff}}$ can be described by the bulk lifetime alone, as expressed in Equation 2.29 [14].

$$\frac{1}{\tau_{\text{eff}}} = \frac{1}{\tau_{\text{bulk}}}. \tag{2.29}$$

To perform passivation, oxygen, nitrogen, or hydrogen atoms are often used [14]. One method used for surface passivation is chemical passivation, such as the stack passivation of hydrogenated amorphous silicon (a-Si:H) and hydrogenated amorphous silicon nitride (a-$Si_xN_y$:H) [21]. This passivation procedure is a two-step process that includes sample etching followed by passivation using the Oxford Instruments PlasmaLab 133 PECVD chamber (Plasma-enhanced chemical vapour deposition) [22]. Information about the electromagnetic field needed to generate the plasma and the pressure in the deposition chamber is confidential to the instrument and process at IFE [22].

The etching process involves immersing the samples in an HNA solution (Hydrofluoric (HF) acid, nitric acid, and acetic acid with a 2:10:5 ratio) for 20 minutes using the CP5-ets etching method to remove any unwanted substances from the surface [22]. This is followed by eliminating any organic residue on the substrate using Piranha cleaning, which is a mixture of sulfuric acid ($H_2SO_4$) and hydrogen peroxide ($H_2O_2$) on the wafers [23]. The first step includes a 2-minute HF dip and cleaning with de-ionized (DI) water. The second step involves an 8-minute immersion in the Piranha solution, followed by cleaning with DI water. The third step is a repetition of the first step, followed by drying in an $N_2$-well [22].

The passivation process begins by removing possible oxide layers on the wafer surface through a 2-minute HF dip in a 5% HF solution, followed by drying in an $N_2$-well. Once the samples are dry, they can be placed in a load-lock chamber with a vacuum environment to prevent surface oxidation. The passivation is then performed using Plasma-Enhanced Chemical Vapor Deposition (PECVD). The passivation starts by depositing a 40 nm layer of hydrogenated amorphous silicon (a-Si:H) on one side of the wafer. The sample is then removed from the vacuum, quickly flipped, and another 40 nm layer of a-Si:H is deposited on the other side of the wafer. After the passivation layer has been deposited, a 70 nm layer of silicon nitride (a-$Si_xN_y$:H) is also deposited on both sides of the sample. This can be observed in the samples as the (a-$Si_xN_y$:H) layer yields a blue colour. The SiNx:H layer serves two purposes: improving the passivation of a-Si:H through a 10-minute annealing process at 230°C and enhancing the sample's resistance against scratches and other handling-related issues during measurements such as lifetime measurements [22].

**Temporal stability of passivated silicon samples**

The article *Temporal stability of a-Si:H and a-SiN$_x$:H on crystalline silicon wafers*, investigates the temporal stability of a-Si:H,a-Si$_x$N$_y$:H, and stack passivation a-Si:H/a-Si$_x$N$_y$:H on silicon wafers [21]. In the article, the measurements were performed over 18 months. During the first 500 hours, the FZ sample undergoes a degradation of about 85% of the initial value. However, after 1500 hours, the sample recovers to about 100% of the initial value. The degradation observed in the samples can be related to weak bonds of Si-H within the a-Si:H films, which can be influenced by light and temperature. However, the samples' recovery and stability over time may be related to the buffer layer of a-Si:H on the sample which then becomes less sensitive to environmental effects [21]. The bonds between silicon and hydrogen can break as a result of light exposure [24].

The quality of the a-Si:H/a-Si$_x$N$_y$:H stack passivation is relatively stable with respect to time. This passivation provides a more stable passivation compared to a single layer of a-Si:H or a-Si$_x$N$_y$:H. At high temperatures, it is found that hydrogen is released from the a-Si:H film by effusion. The temporal stability of the deposition layer depends on the temperature at which it was deposited. In literature, one finding includes a deposition temperature of 400 °C, which results in a more stable stack passivation compared to a layer deposited at 300 °C [25]. By reducing the temperature the risk of impurity diffusion into the bulk is also reduced [25].

Degradation of the a-Si:H/c-Si structure/layer can result in the creation of dangling bonds. Defects assembling and connecting to the material can suffer from light-induced degradation (LID) commonly referred to as the Staebler-Wronski effect (SWE) [26]. This is typical for electronically active defects such as iron that connect to the material [26]. The dangling bond density will result in shorter measured carrier lifetimes due to the impurities in the material. The most prominent example of LID is degradation caused by the activation of the boron-oxygen (BO) defect in Cz-grown silicon [27]. Other contaminants, such as copper, iron-boron, or other iron acceptors, also cause a decrease in lifetime under illumination. The article [27] discusses materials that are susceptible to Light- and elevated Temperature-Induced Degradation (LeTID), such as boron and gallium-doped materials. The detrimental aspect of LeTID is the degradation of the charge carrier lifetime under illumination at elevated temperatures. This degradation is caused by both illumination and current injection [27].

### 2.2.4 Impurity Sources During Crystallisation And Silicon Production Technology

Impurities in silicon can be detrimental to the efficiency, power output, and carrier lifetime of the material. The impurities that assemble in the material are introduced in the production chain incorporated in the material. The silicon feedstock, quartzite, used for silicon ingot growth can contain impurities. The feedstock designated for silicon ingot production undergoes a reduction process utilizing coal,

coke, charcoal or wood chips as reducing agents. During this process, impurities from the electrodes might be introduced into the material. The feedstock is then melted and dopants are subsequently introduced into the molten silicon. The molten silicon is then poured into a furnace, and the furnace elements are introduced into the molten silicon. This increases the impurity concentration in the material [28].

There are multiple methods to produce monocrystalline and multi-crystalline silicon. One method that is frequently used to produce monocrystalline silicon is the Czochralski (Cz) process. This process involves submerging a monocrystalline seed in molten material and subsequently drawing it upwards with a fixed speed, thus maintaining proximity between the growth interface and the melt-atmosphere interface [6]. The crucible and the seed are rotated in opposite directions, which ensures uniform doping distribution in the monocrystalline ingot. This process requires careful control of the process parameters, including temperature, pulling speed, and the rate of rotation. Small deviations can result in defect formation, such as dislocations or grain boundaries, which will impact the electrical properties of the material. Impurities also have an impact on the electronic properties of the material, and these can be introduced from the crucible, feedstock, seed, and the atmosphere in the growth chamber. To minimize contamination, high-purity materials are used for both the crucible and the seed, and the growth chamber is typically filled with an inert gas, such as argon, to prevent oxygen contamination [6]. The crucible is made from quartz, which partly dissolves in the melt, resulting in a relatively high oxygen level in the monocrystalline ingot [6].

Another method to produce monocrystalline silicon is through the float zone pulling method. This method involves the use of a polycrystalline rod that is placed within an enclosure purged with an inert gas to avoid any oxygen contamination. A single crystal seed is then melted onto the polycrystalline rod through induction heating. Subsequently, a section of liquid silicon is moved upwards while being rotated via the vertical movement of the induction coil. Once the silicon cools, it solidifies into a single-crystal form. The desired doping is attained through the introduction of an appropriate dopant in gaseous form to the inert gas. A notable advantage of this process is its ability to further clean the crystal. Thus, these substances are primarily carried with the fluid zone and transported to the upper end of the crystal. With repeated pulling, this process facilitates the production of exceptionally perfect, high-purity crystals with high resistivity for the intended application [6].

Multicrystalline, compared to monocrystalline, is less expensive to produce due to being easier to manufacture. However, they usually exhibit lower efficiency due to the grain boundaries in the material. A common method to produce multicrystalline silicon is through directional solidification (DS). This process involves filling a crucible with high-purity silicon feedstock, which is then heated above its melting point. The heat is then removed from the bottom, and solidification proceeds upwards, creating a temperature gradient. The quality of the polycrystalline silicon produced through DS depends on the purity of the feedstock, the solidification rate, and the temperature gradient along the length of the crucible. By controlling these parameters, high-quality polycrystalline silicon with desired

electrical properties can be achieved. The impurity atoms that are introduced into the material during crystallization originate from the crucible and coating, resulting in a higher impurity concentration at the edges of the ingot [28].

During the solidification process, most of the metallic impurities in silicon prefer to remain in the liquid phase rather than the solid phase. As a result, a higher concentration of impurities is expected in the last solidified region. Consequently, samples taken from the bottom of CZ-silicon ingots and the top of DS-silicon will have a higher impurity concentration compared to other locations in the ingot. This phenomenon is commonly referred to as segregation. The extent of segregation depends on the ratio of impurity concentration in the melt to that in the ingot [28].

## 2.3 Temperature dependence on carrier lifetime

When investigating the temperature dependence of the carrier lifetime, various parameters are considered. This includes extrinsic losses such as SRH and surface recombination, doping concentration, and recombination mechanisms [29, 30]. In the case of a material like silicon, where SRH is the dominant recombination mechanism, an increase in temperature will result in an increase in carrier lifetime [14, 29]. The temperature dependence of PV-device performance is related to the temperature influence on the intrinsic and extrinsic energy losses in the device. The intrinsic losses are unavoidable in the single-junction cell, and the intrinsic losses are related to the conversion loss (Carnot loss, the thermal energy lost from the sun when converting into electricity), emission loss, entropy generation loss, thermalization, and sub-band-gap loss [31]. The Auger recombination mechanism is included as an intrinsic loss as it is a consequence of fundamental material properties [30, 9]. In the literature, the Auger recombination lifetime is found to increase with an increase in temperature for both n- and p-type silicon [32]. It was found that with increasing doping levels the dominant recombination mechanism changes from SRH to Auger recombination [32]. For high doping concentrations, the Auger lifetime was however found to be reduced [32].

The band gap in a semiconductor is influenced by changes in temperature. As the temperature increases, the band gap decreases [9]. This is confirmed through the empirical equation published in [33].

$$E_{\text{gap}}(T) = E_{\text{gap}}(0) - \frac{\alpha T^2}{T + \beta}, \tag{2.30}$$

where $E_{\text{gap}}(0)$=1.170 eV, $\alpha = 4.73 * 10^{-4}$ eV/K is a temperature coefficient, and $\beta = 636$ K, which is a temperature offset. In n-type semiconductors, increasing the temperature results in an increased concentration of electrons, while in p-type semiconductors, it leads to an increased concentration of holes. This effect occurs due to the increased thermal energy that promotes electrons from the valence band and relaxes holes in the conduction band [9].

Single-crystal solar cells measured at lower temperatures are in agreement

with the SRH theory [29]. For mc-Si solar cells, the lifetime is relatively smaller and is found to increase exponentially with temperature due to the presence of recombination centres within the potential barrier associated with the intercrystalline grain boundaries. Within these boundaries, the presence of trapped charges and photogenerated minority carriers leads to the neutralization of the charge, resulting in a reduction in the potential barrier height. Consequently, minority carriers are able to traverse the potential barrier region. However, when the minority carriers encounter recombination centres at the grain boundary, their effective lifetimes are reduced. As the temperature increases, the thermal energy of the carriers also increases, thereby lowering the probability of barrier recombination. Consequently, the lifetime of minority carriers exhibits an exponential increase with rising temperatures [29]. The experimental work in [29] shows that the lifetime in both monocrystalline and mc-Si cells increases with increasing temperature measured in a temperature range of -196.15-226.85 K. When carriers become trapped by defect or impurity levels, their lifetimes at temperatures equal to or below the exhaustion temperature (the temperature at which the Fermi level aligns with the acceptor impurity level) are independent of temperature.

According to [13], the radiative emission in photovoltaic devices increases with temperature due to an increase in the recombination rate, which is caused by an increase in the equilibrium carrier concentration. This phenomenon creates an imbalance between the absorption and emission rates, leading to negative temperature sensitivity. This imbalance characteristic is responsible for decreased efficiency in all photovoltaic devices at higher temperatures [13]. The negative temperature sensitivity, a decrease in lifetime with increasing temperature, is also observed in cases where the btb recombination process is predominant [29].

The Auger lifetime is observed to increase with increasing temperature for both n-type and p-type silicon, while the temperature dependence weakens at high doping concentrations [30]. The temperature sensitivity of SRH recombination can be assessed by examining the equations that make up the SRH lifetime (Equation 2.26), and the parameters are given in Equation 2.20 - 2.25. The influence of temperature is captured by the thermal velocity of electrons and holes, the capture cross-section of electrons and holes, and the intrinsic carrier concentration. Additionally, the SRH densities $n_1$ and $p_1$ depend on temperature itself and through the effective density of states in the conduction and valence bands [30].

CHAPTER

# THREE

# LIFETIME CHARACTERIZATION TECHNIQUES

This chapter will discuss two techniques used to measure carrier lifetime. The carrier lifetime is determined by the recombination dynamics of excess carriers. One of these techniques is the quasi-steady-state photoconductance (QSSPC) method, first introduced by Sinton and Cuevas in 1996 [15]. This method measures the change in photoconductance through a gradual decay of light intensity over several milliseconds. This ensures steady-state conditions in the sample with respect to recombination processes [14]. Another technique utilizes a sharp pulse of illumination that is rapidly terminated and measures the excess carrier density without illumination. This method is referred to as the transient photoconductance decay (PCD) technique and is typically used for measuring high carrier lifetimes [14].

Both the QSSPC and the PCD methods can be described by a generalized analysis procedure proposed by Nagel et al. [34]. The generalized analysis assumes that the recombination rate $\tau_{\text{bulk}} = \tau_{\text{eff}}$ and is valid to any carrier lifetime and flash lamp dependence [34]. The expression for the effective lifetime $\tau_{\text{eff}}$ in the generalized analysis is given in Equation 3.1 [34].

$$\tau_{\text{eff}} = \frac{\Delta n_{\text{av}}}{G_{\text{av}} - \frac{\mathrm{d}\Delta n_{\text{av}}(t)}{\mathrm{d}t}}, \tag{3.1}$$

where $\Delta n_{\text{av}}$ [cm$^{-3}$] and $G_{\text{av}}$ [cm$^{-3}$s$^{-1}$] are the average excess carrier density and the average generation rate, respectively. To determine the effective lifetime, the photoconductance decay with respect to time has to be measured.

## 3.1 Quasi-steady-state photoconductance technique

The QSSPC technique is used to measure lifetimes below 200 $\mu$s, which employs a large signal method that can be used to directly determine the carrier lifetime. The QSSPC technique enables direct measurements of the carrier injection level,

without the need for device simulation [14].

The instrument uses a flash lamp to optically generate carriers in the measured sample. The excess carrier density ($\Delta n$) is measured by observing the changes in the excess photoconductance, denoted as $\Delta\sigma(t)$, of the sample. The change in photoconductance within the sample is detected through the change in permeability caused by the radio-frequency bridge, that is inductively coupled to a coil. The time dependence of the excess photoconductance of the test sample and illumination is determined using the instrument's reference solar cell and an oscilloscope. Through this, the instrument calculates the average excess carrier density ($\Delta n_{\mathrm{av}} = \Delta p_{\mathrm{av}}$) using the following expression.

$$\Delta n_{\mathrm{av}} = \frac{\Delta\sigma(t)}{q(\mu_n + \mu_p)W}, \tag{3.2}$$

where $\mu_{\mathrm{n}}$ and $\mu_{\mathrm{p}}$ [$\mathrm{cm^2V^{-1}s^{-1}}$] are the carrier mobility and $q$ [C] is the elementary charge. Under steady-state conditions, the generation and recombination of electron-hole pairs are in balance. This means that the number of generation and recombination events are equal. The generalized case given in Equation 3.1 in the case of steady-state ($\mathrm{d}\Delta n/\mathrm{d}t \equiv 0$) can be simplified and expressed in terms of the total recombination in the wafer which is expressed as the effective carrier lifetime, $\tau_{eff}$. The expression for the effective carrier lifetime is given in Equation 3.3 [15].

$$\tau_{\mathrm{eff}} = \frac{\Delta n_{\mathrm{av}}}{G_{\mathrm{av}}}. \tag{3.3}$$

The average generation rate ($G_{\mathrm{av}}$ [$\mathrm{cm^{-3}s^{-1}}$]) depends on the illumination intensity $I_{\mathrm{av}}$ which is measured from the calibrated reference solar cell typically expressed in suns (1sun= 1000 $\mathrm{W/m^2}$). The illumination intensity represents the number of photons incident on the surface of the measured sample. The sample absorbs only a fraction, $f_{\mathrm{abs}}$, of the incident light where the rest of the available photons are lost to the environment. The average generation rate within the sample can be expressed through Equation 3.4 [14].

$$G_{\mathrm{av}}(t) = \frac{I_{\mathrm{av}}(t) f_{\mathrm{abs}} N_{\mathrm{ph}}^{1sun}}{W}, \tag{3.4}$$

where $N_{\mathrm{ph}}^{1sun}$ [$cm^{-2}s^{-1}sun^{-1}$] represents the flux of photons in solar light with an irradiance of 1 sun, which generates electron-hole pairs in the sample [14].

The QSSPC method has several advantages in terms of its measurement capabilities. Firstly, it enables the determination of lifetime values across a wide injection range. Additionally, this method allows for similar measurements to those of an operating solar cell under constant illumination, due to the steady-state condition in the sample. Lastly, this method provides data with fewer fluctuations and less instability, as the lifetime is calculated directly from the absolute values of the measured quantities [35].

## 3.2 Transient photoconductive decay technique

The transient photoconductive decay (PCD) technique is a well-established and widely utilized technique for characterizing semiconductor materials and devices [36]. This technique is used to measure carrier lifetimes higher than 100 $\mu$s[36]. The technique uses a pulsed light source to generate e-h pairs in a sample biased under constant current conditions. This includes a sharp illumination peak which ensures photoconductance decay and changes can be observed in the samples' conductivity and voltage [36].

The PCD technique allows for a simplification of the general equation in Equation 3.1 as $G = 0$. The reason is that the excess carrier density is measured after the light source has been turned off and after the photogeneration has decreased to small levels [34]. The lifetime at each carrier density can be determined using the derived Equation 3.5.

$$\tau_{\text{eff}} = -\frac{\Delta n_{\text{av}}}{\frac{\mathrm{d}\Delta n_{\text{av}}(t)}{\mathrm{d}t}}. \tag{3.5}$$

This is only valid when the carrier lifetime is significantly higher than the decay of the illumination source. The reason is that the illumination source has to generate enough carriers to measure the lifetime for the given sample which is achieved through the sharp flash, generating a peak in illumination [36]. To achieve accurate results, it is necessary to ensure that the sample maintains sufficient excess carrier density well after the flash has terminated. This requires the flash turn-off time (50 $\mu$s for the Sinton BCT-300 instrument) to be shorter than the carrier lifetime. This means that this technique is only valid for carrier lifetimes longer than 100 $\mu$s [35].

The PCD method has a few limitations. These include the dependence on semiconductor material, excess carrier density, light source inhomogeneities, filter thickness, and temperature [36]. Firstly, the excess carrier density, which is measured to calculate the lifetime, depends on the semiconductor material. In silicon, recombination centres with energy states primarily occur in the forbidden gap, which negatively influences the lifetime [36]. Secondly, the light source generates excess carriers in the incident sample, and depending on the intensity or type of light, the carrier distribution at the very beginning of the decay might not be optimal as both generation and recombination take place [36]. For this reason, the carrier lifetime of the sample is measured after the flash has terminated [35]. Thirdly, semiconductor materials often exhibit non-uniform distributions of resistivity and lifetime ($\tau_{\text{PCD}}$) due to the presence of dopants and impurities. In the analysis of PCD measurements, it is crucial to recognize that the derived $\tau_{\text{PCD}}$ value represents an average over the illuminated region. Consequently, variations in $\tau_{\text{PCD}}$ may be observed across different segments of the sample [36]. fourthly, the use of a filter for PCD measurements allows approximation of uniformity. In the case of specimens with inhomogeneities, the presence of a filter can introduce variations in the measured decay time. The material's lifetime and the location of excess carrier generation within the specimen contribute to determining the

effect of filter thickness on measurements [36]. Lastly, The data obtained from this method depends on the derivative which can lead to noisy data in some cases [35].

This method also has some advantages as it is a "stand-alone" method – in other words, it does not require an independent and simultaneous measurement of the generation rate, as the QSSPC method. This means that amount of incident light that is absorbed in the sample, the optical factor, is irrelevant in the PCD analysis. The only purpose of the light sensor is to indicate when the flash has finished and trigger the measurement so the data analysis can begin [35].

An instrument that allows career lifetime measurements with the QSSPC and the PCD technique is the BCT-300 Photoconductance Lifetime Tester (BCT-300) from Sinton Consulting [35].

## 3.3 The SRH equation and its linearizaiton

Lifetime spectroscopy (LS) is a method that allows the analysis of defect and impurity energy levels in a material. This can be performed by other conventional methods as well, however, concentrations of defects outside the detection limit show a significant influence on the carrier lifetime. By measuring the carrier lifetime the temperature and injection-dependent carrier lifetime can be assessed. through this information, one can perform an LS analysis and obtain information about the material quality that can be used to directly identify impurities if the injection and temperature dependence of carrier lifetime is analyzed by measuring recombination lifetime. There are different approaches to investigating this, and all of these methods are based on the SRH Theory. S. Rein through his book *Lifetime Spectroscopy: A Method of Defect Characterization* states that the sensitivity of lifetime spectroscopy allows for analyzing defect centres through the recombination process, which can be used to identify defects relevant to semiconductors. One of the main advantages of LS is that only the relevant defects to the semiconductor device are identified the defects that are relevant to semiconductor devices. LS is the current most sensitive diagnostic method for the identification and analysis of impurities in semiconductor materials [14, 37]. Some of the LS techniques reported in the literature are *Temperature-dependent lifetime spectroscopy* (TDLS), *Injection-dependent lifetime spectroscopy* (IDLS), and *Temperature- and injection-dependent lifetime spectroscopy* (TIDLS) [14].

### 3.3.1 The Shockley-Read-Hall equation

The SRH equation, seen in Equation 2.26 forms the basis of different lifetime spectroscopy techniques. One parameter of the SRH-equation is the fundamental time constant $\tau_{n0}$ and $\tau_{p0}$ for electrons and holes, respectively. They are proportional to the inverse product of the defect concentration $N_t$ [$cm^{-3}$] and the capture cross-sections $\sigma_n$ and $\sigma_p$ [$cm^{-2}$] for electrons and holes, respectively [14].

| Doping | Majority carrier | Magnitude of the relevant densities |
|---|---|---|
| p-type | $p_0 = N_\mathrm{a}$ | $p_0 \gg n_\mathrm{i}^2/N_\mathrm{a} = n_0$ |
| n-type | $n_0 = N_\mathrm{d}$ | $n_0 \gg n_\mathrm{i}^2/N_\mathrm{d} = p_0$ |

**Table 3.1:** Limiting case of Low-level injection conditions ($\Delta n \ll p_0 + n_0$) [14].

$$\tau_{\mathrm{j}0} = \frac{1}{(N_\mathrm{t}\sigma_\mathrm{j}\nu_{\mathrm{th,j}})}, \tag{3.6}$$

where j=n,p, $\nu_{\mathrm{th,j}}$ [cm/s] is the thermal velocity. The thermal velocity ($\nu_\mathrm{th} = \sqrt{(2kT)/m^*_{\mathrm{e/h}}}$, where $m^*_{\mathrm{e/h}}$ are the effective masses of electrons(e) and holes(h) respectively) of electrons and holes varies due to differences in their effective masses, electrons being a heavier element than holes [9]. To include the capture asymmetry which is characteristic of a defect state, a symmetry factor $k$ is introduced [14].

$$k \equiv \sigma_\mathrm{n}/\sigma_\mathrm{p} \approx \tau_{\mathrm{p}0}/\tau_{\mathrm{n}0}. \tag{3.7}$$

This symmetry factor is only dependent on the structure of the defect. By applying Equation 3.7 to the SRH lifetime equation from Equation 2.26, the SRH lifetime can be written as the following [14].

$$\tau_\mathrm{SRH} = \tau_{\mathrm{n}0}\left[\frac{p_0 + p_1 + \Delta n}{p_0 + n_0 + \Delta n} + k\frac{n_0 + n_1 + \Delta n}{p_0 + n_0 + \Delta n}\right]. \tag{3.8}$$

Equation 3.8 represents the SRH-lifetime equation with the dependencies on injection level, doping concentration, defect parameters and temperature. Depending on the injection level, two levels are described. The low-level injection is the case when the excess carrier concentration is much smaller than the equilibrium concentrations of electrons and holes (i.e., $\Delta n \ll n_0 + p_0$) and the high-level injection is the case when the excess carrier concentration is much greater than the equilibrium concentrations of electrons and holes (i.e., $\Delta n \gg n_0 + p_0$). The limiting case of low-level injection conditions for a p-type and an n-type semiconductor is shown in Table 3.1. In the limiting case of LLI conditions Equation 3.8 with relevant properties presented in Table 3.1, the SRH-LLI for a p-type and an n-type semiconductor can be expressed in Equation 3.9 and Equation 3.10, respectively [14].

$$\tau_\mathrm{SRH}^{\mathrm{LLI},p} = \tau_{\mathrm{n}0}\left[\left(1 + \frac{p_1}{N_\mathrm{a}}\right) + k\left(\frac{n_1}{N_\mathrm{a}}\right)\right], \tag{3.9}$$

$$\tau_\mathrm{SRH}^{\mathrm{LLI},n} = k\tau_{\mathrm{n}0}\left[\left(1 + \frac{n_1}{N_\mathrm{d}}\right) + \frac{1}{k}\left(\frac{p_1}{N_\mathrm{d}}\right)\right]. \tag{3.10}$$

In the limit of high-level injection condition ($\Delta n \gg n_0 + p_0, n_1, p_1$) the simplification of Equation 3.8 can be expressed through the following equation [14].

$$\tau_\mathrm{SRH}^\mathrm{HLI} = \tau_{\mathrm{n}0} + \tau_{\mathrm{p}0} = \tau_{\mathrm{n}0}(1 + k). \tag{3.11}$$

Equation 3.11 shows that the SRH recombination under high-level injection is limited by the slower of the two capture processes and is independent of the defect level.

For a p-type (n-type) semiconductor under low-level injection conditions, three types of defects have to be considered. A deep defect level close to or in the mid-gap, a shallow defect level that is close to the CB edge (VB edge for n-type material), and lastly, a defect level in the transition region which is between the deep and shallow defect levels [14]. These will be further explained in Chapter Section 3.3.2.

### 3.3.2 Temperature-dependent lifetime spectroscopy

TDLS measures the carrier lifetime as a function of temperature. The samples are illuminated with a light source that generates excess minority carriers, and the decay of the excess carrier density is monitored over time using an instrument. The carrier lifetime in semiconductor materials is strongly dependent on temperature, as temperature changes can affect the mobility and concentration of carriers. In TDLS, the lifetime is typically measured at a fixed injection level, while the temperature dependence on the lifetime is analyzed to determine the recombination mechanism that occurs in the material. The TDLS method allows for the determination of the defect energy $E_\mathrm{t}$ from the linear slope of an Arrhenius plot [14, 37]. The linear slope increases the deeper a defect energy level is. This is a result of the reduction in the SRH densities for deep defect levels compared to shallow defect levels [14].

The rate of increase of the slope of the Arrhenius plot depends on the defect. This section is limited to shallow defect levels close to the CB edge, which can be derived from Equation 3.9. For a p-type silicon sample, the LLI-SRH lifetime is expressed through Equation 3.9, at a defect in the upper half of the band gap, the LLI-SRH lifetime can be reduced to the following equation.

$$\tau_{\mathrm{SRH}}^{\mathrm{LLI,p}}(T) = \tau_{\mathrm{n0}}(T)\left[1 + k\frac{n_1(T)}{p_0}\right]. \tag{3.12}$$

The $n_1/p_0$ term can be neglected at low temperatures. The reason is that the exponential temperature dependence of the SRH density $n_1$ seen in Equation 2.3, where $E_\mathrm{F} = E_\mathrm{t}$ for the SRH density of electrons is the main contributor to the overall temperature dependence. The ratio $n_1/p_0$ in Equation 3.12 increases with increasing temperature, reflecting the decreasing recombination activity of the defect as the Fermi level $E_\mathrm{F}$ approaches mid-gap [14]. $n_1$ is influenced by the effective density of states, $N_\mathrm{C}$, in the conduction band, which is also temperature dependent as seen from Equation 2.5. The electron capture time constant given in Equation 3.6 only depends on temperature via the thermal velocity $\nu_\mathrm{th}$ expressed through Equation 3.13.

$$\nu_{\mathrm{th}}(T) = \nu_{\mathrm{th}}^{300\mathrm{K}}\left(\frac{T}{300K}\right)^{1/2}, \tag{3.13}$$

where $\nu_{\mathrm{th}}^{300} = 10^7$ [cm/s] is the thermal velocity at 300K. This equation assumes that the capture cross-sections are temperature independent. The temperature dependence of the time constant $\tau_{\mathrm{n_0}}(T)$, can then be expressed by Equation 3.14 [14].

$$\tau_{\mathrm{n0}}(T) = [N_{\mathrm{t}}\sigma_{\mathrm{n}}\nu_{th}(T)]^{-1} = \tau_{\mathrm{n_0}}^{300\mathrm{K}} \left(\frac{T}{300K}\right)^{-1/2}, \tag{3.14}$$

where $\tau_{\mathrm{n_0}}^{300\mathrm{K}}$ is the electron capture time constant at 300K. At sufficiently low temperatures (T< 300 K) the term $n_1/p_0$ can be neglected resulting in the LLI-SRH lifetime to equal the electron capture time $\tau_{\mathrm{n_0}}(T)$. At sufficiently low temperatures the $\tau_{\mathrm{n_0}}(T)$ in Equation 3.12 is independent of the defect parameters $E_{\mathrm{t}}$ and $k$ and exhibits a slight decrease with increasing temperature which can be observed from Equation 3.14. At sufficiently high temperatures the defect-level-dependent term $n_1/p_0$ is dominant and the $\tau_{\mathrm{n_0}}$ can be neglected. To gain information about the defect from the measured carrier lifetime the following assumptions are considered for a shallow defect level close to the CB edge; the position of the defect level $E_{\mathrm{t}}$ in the band: $E_{\mathrm{t}} \rightarrow E_{\mathrm{C}}$, the magnitude of the relevant densities: $p_1 \ll p_0 \ll n_1$, recombination activity of the defect: $\tau_{\mathrm{SRH}}^{LLI,p}/\tau_{n0} = k(n_1/p_0)$, and position of $E_{\mathrm{F}}$ in relation to $E_{\mathrm{t}}$: $E_{\mathrm{t}} \gg E_{\mathrm{C}} - E_{\mathrm{F}}$ [14]. From this information, it is possible to derive the Arrhenius slope from the SRH lifetime under LLI conditions, where $E_{\mathrm{C}} = E_{\mathrm{g}}$, displayed in Equation 3.9.

$$\frac{\tau_{\mathrm{SRH}}^{LLI,p}}{\tau_{n0}} = k\frac{N_{\mathrm{C}}}{N_{\mathrm{A}}} \times \exp\left(-\frac{E_{\mathrm{g}} - E_{\mathrm{t}}}{k_{\mathrm{b}}T}\right). \tag{3.15}$$

To isolate the temperature, logarithmic transformation is applied.

$$\log\left[\frac{\tau_{\mathrm{SRH}}^{LLI,p}}{\tau_{n0}}\right] = \frac{E_{\mathrm{t}} - E_{\mathrm{g}}}{k_{\mathrm{b}}} \times \frac{1}{T} + \frac{N_{\mathrm{C}}}{N_{\mathrm{A}}}. \tag{3.16}$$

A linear equation is represented as y = mx + b. In this equation, y represents the dependent variable, m and b are slope and intercept, respectively and x represents the independent variable. In Equation 3.16 the dependent variable is the logarithm of the term $\log\left[\frac{\tau_{\mathrm{SRH}}^{\mathrm{LLI,p}}}{\tau_{\mathrm{n0}}}\right]$, the slope is represented by the addend $\frac{E_{\mathrm{t}}-E_{\mathrm{g}}}{k_{\mathrm{b}}}$, the intercept is represented by $\frac{N_{\mathrm{C}}}{N_{\mathrm{A}}}$, and the independent variable is represented by $1/T$. The rate of increase of the linear slope equals the defect level close to the CB edge in the sample. Information about the defect level can be used to directly characterize the type of impurity, as different impurities in the material have known energy levels [14].

### 3.3.3 Injection-dependent lifetime spectroscopy

The IDLS characterization technique is used to measure the decay of the excess carriers to determine the carrier lifetime as a function of the injection level, expressed as $\eta = \Delta n/(n_0 + p_0)$ [14]. In IDLS a sample is illuminated with a light source that generates excess minority carriers, and the decay of the excess carrier density is monitored over time using a detector. The injection level can be

varied by controlling the light intensity of the light source, which determines the concentration of excess minority carriers injected into the material. In IDLS, an important consideration is the additional trapping centres that do not contribute to recombination but instead interact with the minority band, leading to the external trapping effect. This effect is well-known in multi-crystalline and Czochralski silicon. These trapping centres can have a significant impact on lifetime measurements, particularly when using photoconductance-based techniques [14].

The TDLS analysis method assumes that the electron and hole capture cross-sections $\sigma_{\mathrm{n}}$ and $\sigma_{\mathrm{p}}$ are temperature independent, which is not the practical case [14]. However, utilizing the IDLS method, the values of the capture cross sections can be determined with high accuracy [37]. By combining these methods (IDLS and TDLS) the defect energy level and the capture cross sections can be determined. The combination of these two methods, IDLS + TDLS) is commonly known as temperature and injection-dependent lifetime spectroscopy (TIDLS).

### 3.3.4 Lifetime spectroscopy analysis based on the SRH equation

To enable temperature-dependent lifetime measurements, multiple setups in the scientific literature are used. One method to perform TDLS is performed by using the original QSSPC setup from Sinton Consulting and connected to a temperature-controlled sample stage positioned on top of the photoconductance sensor coil [37]. To ensure electrical insulation a Pyrex$^{TM}$ glass disk is kept at a distance of 1mm from the coil by means of insulating spacers, The heating power is regulated via a controller [37]. The coil of the instrument is subject to heating during measurements, however, the instrument was calibrated at multiple temperatures. It was concluded that since the calibration curves did not change with temperature, the heating of the coil would not affect the lifetime measurements and that this setup was well suited for TIDLS/TDLS applications [37].

Another study used the Sinton instrument WCT-100 combined with a heating and cooling stage [38]. In this study, the instrument was calibrated and the uncertainty in the calibration curve represents the 95% confidence limit. Other methods used for TDLS and IDLS using the Sinton instruments WCT-120TS which has a temperature stage integrated into the instrument, and photoluminescence (PL) imaging to look at the spatial variations of the effective minority carrier lifetime in samples measured [39, 22, 40].

CHAPTER

# FOUR

# EXPERIMENTAL WORK

This chapter is divided into 2 parts. The first part introduces the samples used and their preparation. The second part, Section 4.2 is a description of the measurements with the corresponding instrument used in the experimental work.

## 4.1 Materials

The samples investigated in this report are given in Table 4.1 and are displayed in figures 4.2-4.9. Most samples are p-type boron-doped monocrystalline silicon samples produced by the Czochralski (Cz) method. To accurately measure the sample lifetime, the bulk recombination properties have to be determined. This requires a reduction in the impact of the surface recombination so that the only contribution when measuring the effective lifetime comes from the bulk. For this reason, the samples were sent to IFE (Institutt for Energiteknikk) for passivation according to the method described in Section 2.2.3.

**Table 4.1:** Information about all measured samples in the thesis, where DS represents directional solidification.

| Sample ID | Sample Type | Growth method | Doping | Passivated | Thickness [mm] | Doping [$cm^{-3}$] | Figure |
|---|---|---|---|---|---|---|---|
| 9B | Wafer | Czochralski | Boron | Yes | 0.557 | 9.785E16 | Figure 4.2 |
| 12B | Wafer | Czochralski | Boron | Yes | 0.968 | 9.785E16 | Figure 4.2 |
| 2T | Wafer | Czochralski | Boron | Yes | 0.500 | 9.785E16 | Figure 4.2 |
| 5T | Wafer | Czochralski | Boron | Yes | 0.970 | 9.785E16 | Figure 4.3 |
| 15B | Brick | Czochralski | Boron | No | 10.000 | 9.785E16 | Figure 4.3 |
| 14B | Brick | Czochralski | Boron | No | 10.000 | 9.785E16 | Figure 4.3 |
| 7T | Brick | Czochralski | Boron | No | 10.000 | 9.785E16 | Figure 4.3 |
| C-196060 | Brick | Czochralski | Boron | No | 25.000 | 7.809E16 | Figure 4.4 |
| FZ | Wafer | Float Zone | Boron | Yes | 0.260 | 1.512E16 | Figure 4.5 |
| IC - 1T | Wafer | Czochralski | Boron | No | 0.166 | 9.785E16 | Figure 4.6a |
| IC - 1B | Wafer | Czochralski | Boron | No | 0.200 | 9.785E16 | Figure 4.6a |
| IC - x1 | Wafer | Czochralski | Boron | Yes | 0.160 | 5.713E16 | Figure 4.6b |
| IC - x2 | Wafer | Czochralski | Boron | Yes | 0.160 | 5.713E16 | Figure 4.6b |
| n-type 1 | Wafer | Czochralski | Phosphorus | No | 0.165 | 3.227E15 | Figure 4.7a |
| n-type 2 | Wafer | Czochralski | Phosphorus | No | 0.165 | 3.227E15 | Figure 4.7b |
| multi-grains | Wafer | DS | Boron | No | 0.194 | 1.695E16 | Figure 4.8a |
| m-cryst | Wafer | DS | Boron | No | 0.0260 | 2.650E16 | Figure 4.8b |
| QSSPC-1 | Brick | DS | Boron | No | 15.000 | 1.242E16 | Figure 4.9a |
| QSSPC-2 | Brick | DS | Boron | No | 15.000 | 1.242E16 | Figure 4.9b |

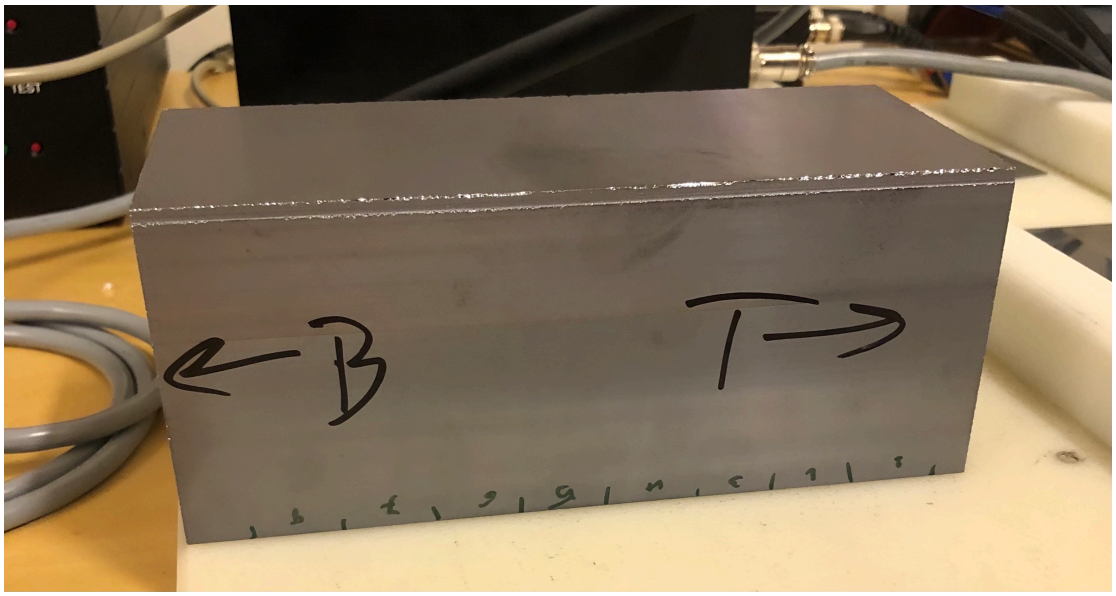


**Figure 4.1:** A p-type boron-doped monocrystalline block extracted from an ingot made in the SINTEF Heliosi lab utilizing the Czochralski furnace. The total length of the block is 18 cm.

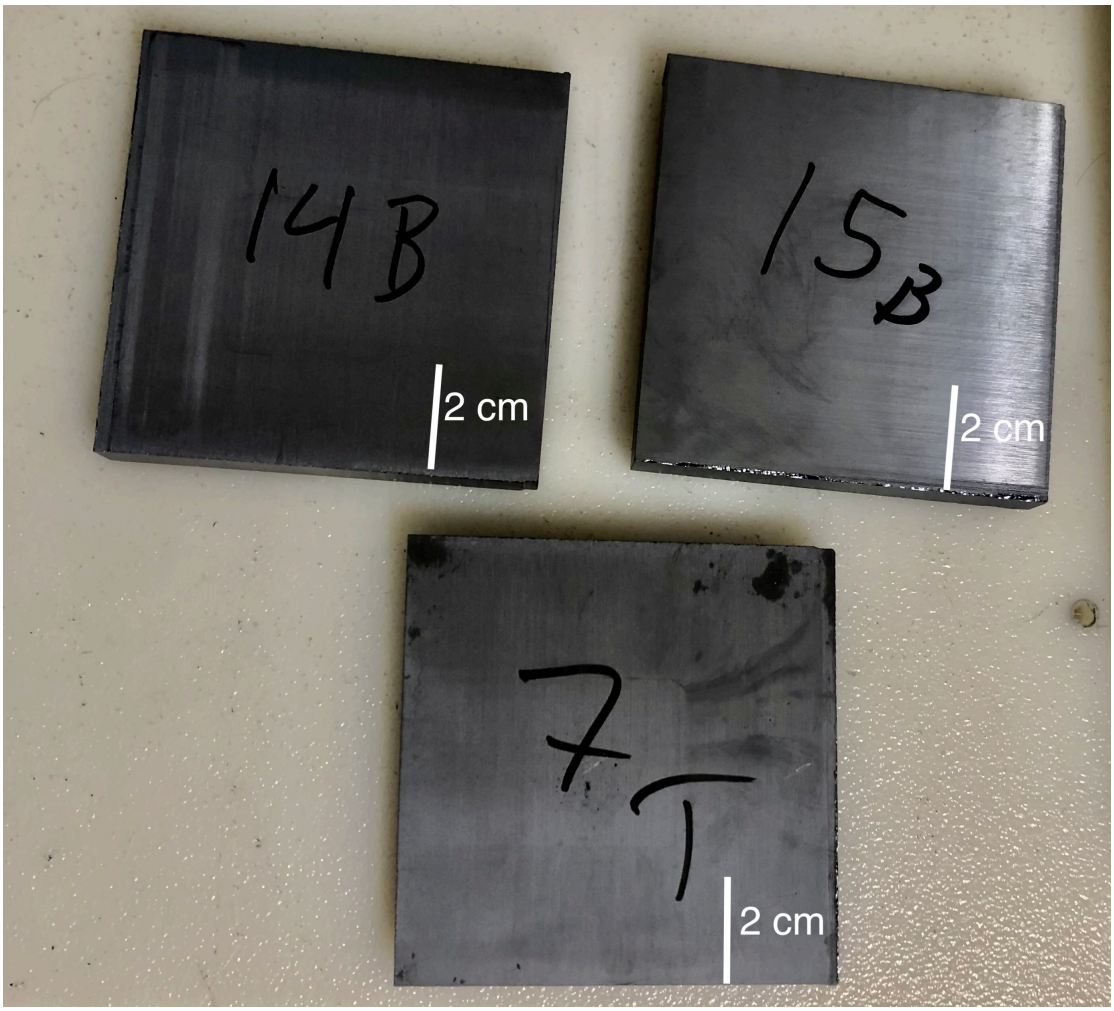


**Figure 4.2:** Three 8x8 cm p-type boron-doped Cz bricks cut from the block in Figure 4.1. The notation B and T represents samples cut from the bottom and top respectively. The thickness of the samples is 1 cm.

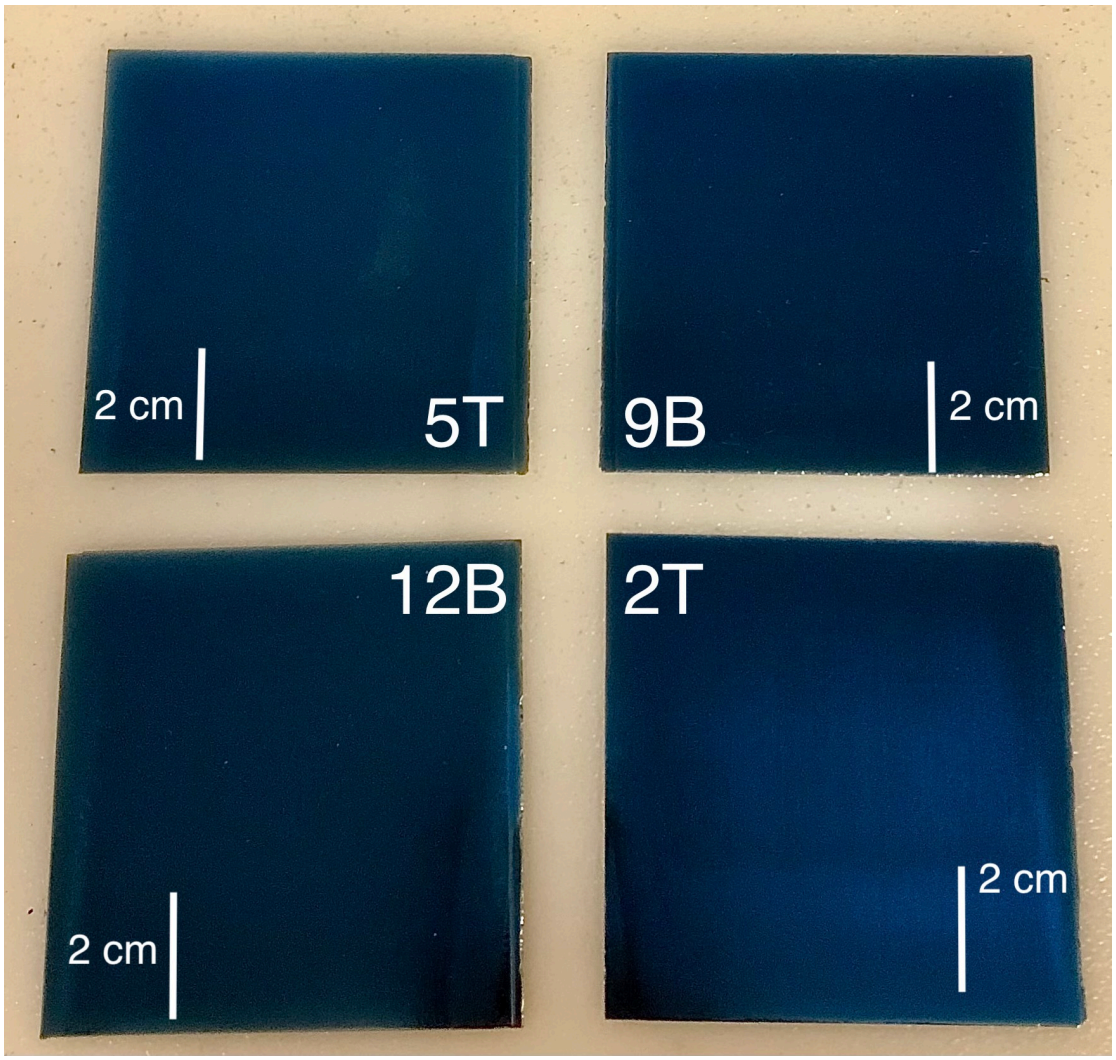


**Figure 4.3:** Four 8×8 cm p-type boron-doped monocrystalline Cz samples cut from the top (T) or the bottom (B) of the block (seen in Figure 4.1. The samples have been passivated with the stack passivation of a-Si:H/a-$Si_xN_y$:H through the procedure explained in Section 2.2.3.

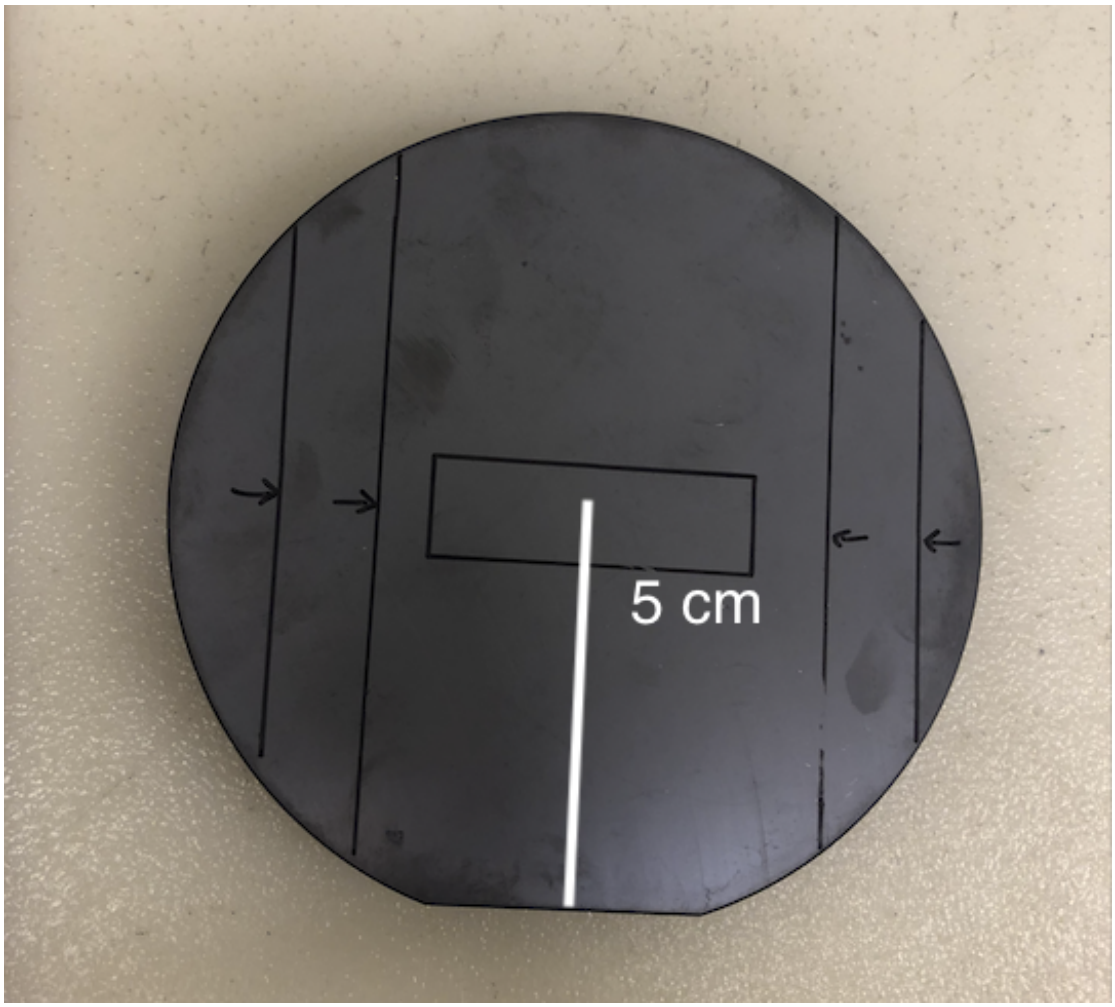


**Figure 4.4:** The sample C-196060 is a p-type boron-doped Cz monocrystalline sample with a diameter of 10 cm and a thickness of 2.5 cm.

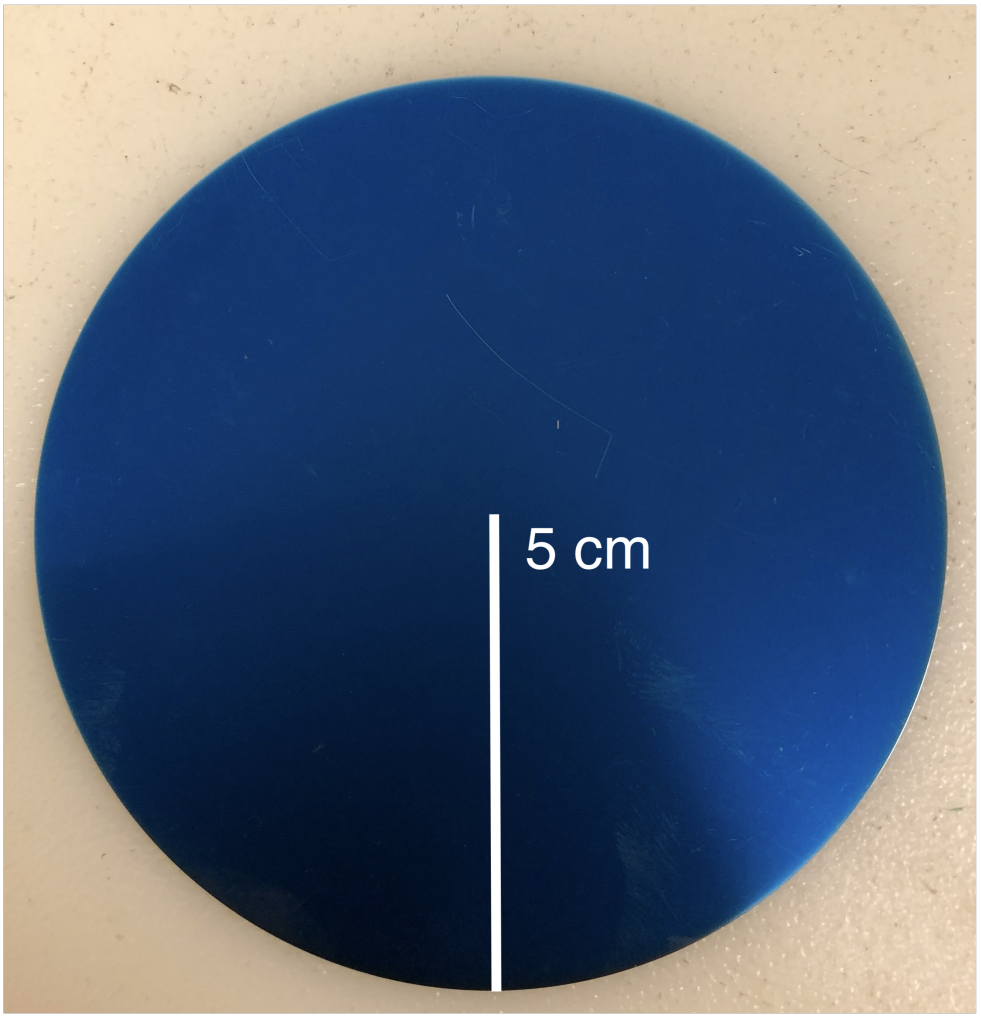


**Figure 4.5:** The FZ sample is a p-type boron-doped monocrystalline wafer produced through the float zone process with a diameter of 10 cm. The sample has been passivated with the stack passivation of a-Si:H/a-Si$_x$N$_y$:H through the procedure explained in Section 2.2.3.

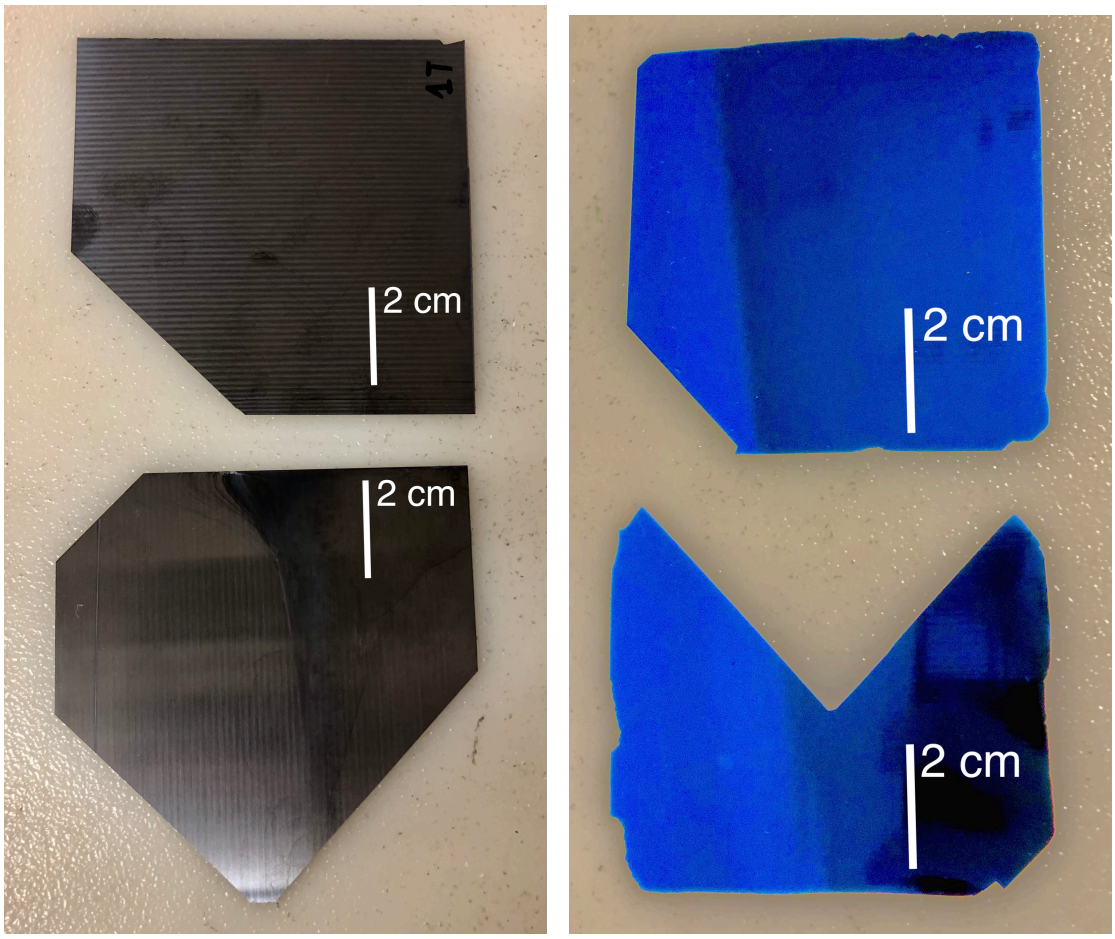


**(a)** **(b)**

**Figure 4.6:** The samples Figure 4.6a and Figure 4.6b are p-type boron-doped monocrystalline silicon samples produced by the Cz process. The size of the samples is 5×5 cm. The Figure 4.6a are unpassivated and the Figure 4.6b are passivated with the stack passivation of a-Si:H/a-$Si_xN_y$:H through the procedure explained in Section 2.2.3. During the passivation process, the IC-x2 experienced some breakage.

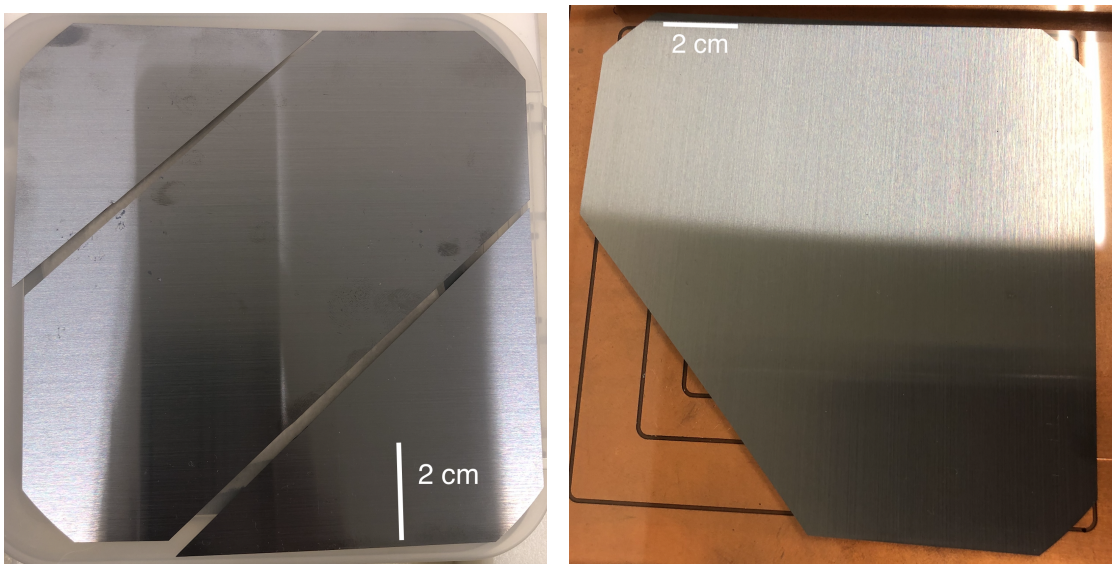


**(a)** **(b)**

**Figure 4.7:** The samples displayed in Figure 4.7a and Figure 4.7b are n-type phosphorous-doped monocrystalline silicon samples produced by the Cz process. The size of the samples is 12x12 cm.

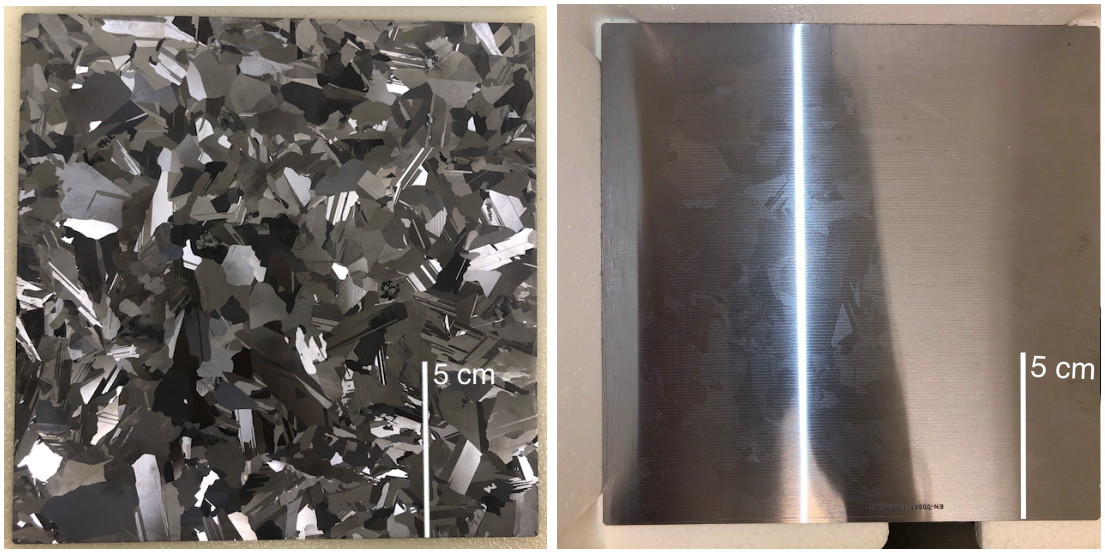


**(a)** **(b)**

**Figure 4.8:** The samples Figure 4.8a and Figure 4.8b are p-type boron-doped mc-Si samples produced through directional solidification. The size of the samples is 15×15.

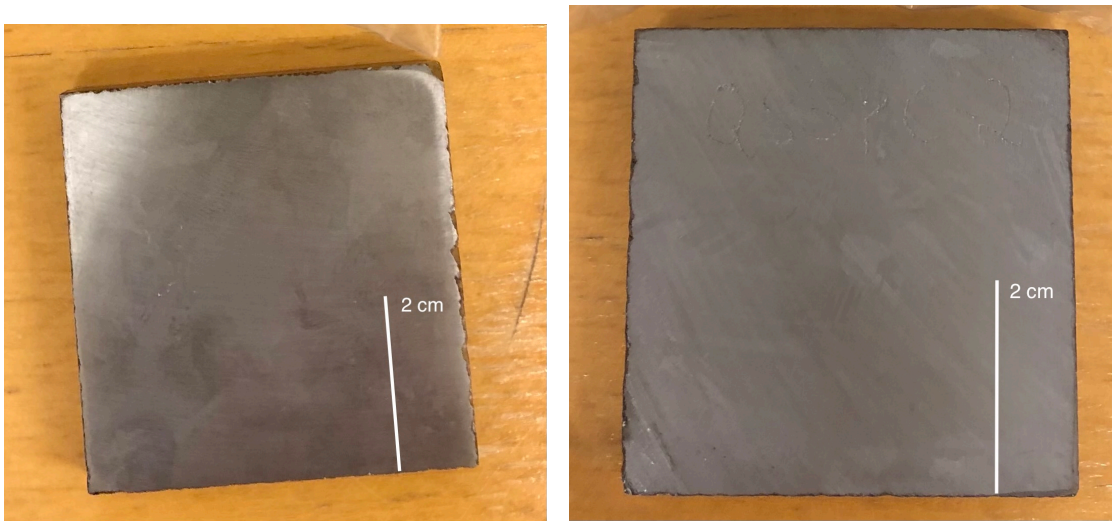


**(a)** **(b)**

**Figure 4.9:** The samples QSSPC-1 (seen in Figure 4.9a) and QSSPC-2 (seen in Figure 4.9b) are p-type boron-doped mc-Si bricks produced by directional solidification with a thickness of 1.5 cm. The size of the bricks is 5×5 cm.

## 4.2 Method

To measure the temperature-dependent carrier lifetimes the BCT-300 setup (Figure 4.10), a Peltier element, a temperature stabilizer, a temperature regulator, and a quartz plate for electrical insulation. To secure exactly similar conditions, the wafers were placed on the heat plate also when mapping lifetimes at room temperature. The measured temperature range is 10-75 °C, as a representation of the Nordic climate [13].

### 4.2.1 BCT-300

The *Sinton consulting* instrument BCT-300 is a non-destructive, optical measurement device used to measure the carrier lifetime in silicon samples [35]. The primary application of the *Sinton Consulting* BCT-300 is measuring as grown boron-doped Cz silicon ingots and bricks. The instrument is not optimized for measuring wafers as they are prone to breakage, and measurements include an error 0.1 $\mu$s [35]. For this reason, *Sinton Consulting* recommends using a specific wafer measurement tool, the WCT-120 [35]. As this instrument is not available for the thesis, the BCT-300 is used with great caution.

To ensure accurate measurements when using the BCT-300 instrument, several steps must be followed. First, the instrument must be turned on and all components properly connected as per the manufacturer's instructions [35]. After turning on the instrument, it is recommended to wait for at least 30 minutes to allow the instrument to reach a stable internal temperature of 25 °C, before measurements are conducted. When the instrument has reached a stable internal


**Figure 4.10:** Part of the experimental setup which consists of the BCT-300 instrument (1) and temperature regulator (2).


**Figure 4.11:** The figure displays the BCT-300, with the 1000 nm filter inserted, measuring a wafer. The BCT-300 shows a green LED light indicating that a stable internal Temperature has been reached.

temperature the green LED on the instrument is lit, as displayed in Figure 4.11. While using the BCT-300 instrument the red LED will be turned on and off, this indicates that the instrument is being maintained at a constant temperature of 25°C.

Before taking measurements, it is important to insert the appropriate filter into the filter slot, which is determined by the lifetime of the sample being measured. As shown in Table 4.2, the inserted filter determines the measurement mode (QSSPC or Transient analysis). When measuring either wafers or bricks, the flash setting of the Flash Power Supply (FPS) - 300 must be set to high (HI) for Transient analysis mode and low (LO) for QSSPC analysis mode. Additionally, the base resistivity of the sample in $\Omega \cdot$cm and the type of substrate (n- or p-type) must be specified before measurements can be taken. The minority carrier density (MCD) must also be specified, as per Table 4.2.

**Table 4.2:** Measurement technique, Specified MCD based, lifetime range and filter used depending on analysis mode for the BCT-300 instrument [14, 16].

| Illumination mode | Analysis Type | Specified MCD [$cm^{-3}$] | Lifetime range [$\mu s$] | Filter (nm) |
|---|---|---|---|---|
| Quasi-Steady-State | QSS1000 | 1E15 (p-type) | $< 200$ | 1000 |
| | QSS850 | 5E14 (n-type) | $< 2$ | 850 |
| Transient | Transient | 1E15 (p-type) | $> 100$ | 850 |
| | Transient | 5E14 (n-type) | $> 100$ | 850 |

The process of qualifying the tester to ensure accurate measurements and calibrating the instrument is given in Appendix 6.2 chapter 4.2.1 and 4.2.2 respectively.

After these steps are performed, the instrument can be zeroed by placing it on top of the plastic measurement platform and pressing the "Zero the instrument" button in the software. Then by placing a sample on the plastic measurement platform (or on the quartz plate) and the instrument on top of the sample, ensuring the sensor region is in complete contact with the sample, the sample can be measured by pressing "Measure sample". The lifetime is usually reported as a function of minority carrier density (MCD). The results obtained from the measurements are represented in a table. The conductance sensor voltage and the light sensor voltage as a function of time are presented in a graph. The data obtained from each measurement can then be collected and downloaded as a text file for later processing.

The carrier lifetime is estimated through the change in conductivity that is measured by an eddy-current conductance sensor and a filtered xenon flash lamp. Depending on the lifetime of the sample, the Quasi-Steady-State Photoconductance (QSSPC) or the Transient Photoconductance Decay (Transient PCD) techniques. The primary purpose of this equipment is to determine the lifetime of carriers in monocrystalline or multi-crystalline silicon ingots, bricks or wafers that are either thinner than 1mm (*Wafer lifetime software*) or larger than 1cm (*Brick lifetime software*) [35]. The instrument allows measurement on unpassivated samples directly after growth as the instrument is able to measure the bulk lifetime. The main function of the instrument is to qualify high-purity silicon without any surface preparation of the measured sample [35]. This also includes measuring the trap density in the semiconductor. The instrument is able to provide accurate results of lifetime measurements from $0.1\mu s$ to greater than 10ms [35].

In transient photoconductance decay measurements, the relatively slow detrapping of minority carriers can cause a long tail in the photoconductance decay, which gives the appearance of an extremely long lifetime. However, this apparent lifetime does not represent the actual recombination lifetime but is instead an output result caused by the presence of traps. Traps may influence the steady-state photoconductance of a sample. At carrier densities equal to or lower than the trap density, the presence of minority carrier traps causes a relative increase in the concentration of majority carriers to maintain charge neutrality. This results in an increase in the steady-state photoconductance above its value when traps are absent, which in turn leads to a longer apparent lifetime [35].

To obtain the conductivity of semiconductor material, the voltage output from the eddy current sensor of the BCT-300 instrument is converted to conductivity using Equation 4.1, where A, B, and C are obtained from the calibration curves in the software used. The resulting conductivity value is expressed in Siemens [$\Omega^{-1}$] [35]. The value of C in Equation 4.1 corresponds to the voltage output from an undoped wafer, and it serves as a reference point on the calibration curves. To ensure accurate measurements, it is necessary to "zero the instrument" before each measurement. Changes in the instrument's operating temperature may affect the accuracy of the measurements, therefore the calibration curve must be normalized to the undoped sample for the current operating conditions. The BCT-300 instrument subtracts the air voltage from the measured sample conductivity to minimize errors in the measurements [35].

$$\sigma = A(V - C)^2 + B(V - C), \tag{4.1}$$

The carrier recombination lifetime measurements of PV silicon at brick or ingot level is an accurate method to verify quality, purity, and growth conditions and to ensure that the material will yield high-efficiency solar cells [35]. The Sinton Instruments eddy-current lifetime measurement instruments offer the best available measurement of the carrier lifetime of these samples in the as-grown and as-cut stages without the need for surface preparation.

The two modes of measurement (QSSPC and Transient PCD) available with the Sinton Instrument tools are described below. In both cases, the sample is illuminated by an IR-Pass filtered xenon flash lamp while the photoconductance is measured simultaneously by an eddy current conductance sensor [35].

## Quasy steady state photoconductive decay

The QSSPC mode employs an illumination flash that decays slower ($>$ 10 times slower) than the carrier lifetime of the sample. This enables the instrument to calculate the effective carrier lifetime through the steady state equation: $\tau_{eff} = \Delta n/G$, where G is the photogeneration within the sample and $\Delta n$ is the carrier density. G is calculated based on the calibrated illumination sensor, known illumination spectrum, and material absorption. The illumination intensity also depends on the filter used, which is determined by the carrier lifetime of the sample seen in Table 4.2. $\Delta n$ is calculated based on the measured photoconductance and calculated through Equation 3.2, and known material and instrument parameters [35].

For a thick sample ($>$ 1 cm) such as an ingot or brick, the measured carrier lifetime depends on the bulk carrier lifetime and conductance depth sensitivity of the instrument, the illumination spectrum, and the sample surface recombination velocity [35]. In QSSPC mode, the measured lifetime is limited by the recombination of carriers at the as-cut or as-grown surface. Since the surface properties are predictable for p-type samples, the contribution of the surface to the measured lifetime can be removed and the bulk lifetime can be estimated [35]. In the QSSPC

mode, the lifetime measured at specific MCD will be lower than the bulk lifetime due to the unpassivated surface [35].

### Transient photoconductive decay

The Transient Photoconductance Decay (PCD) method involves generating carriers with a pulse of illumination that quickly terminates. The resulting decay in the photoconductance is then measured with the eddy current sensor. The carrier recombination lifetime can then be calculated based on Equation 3.5. Just as with the QSSPC mode measurement, the transient mode measured lifetime consists not only of the bulk carrier lifetime but also of the instrument depth sensitivity, illumination spectrum, and surface recombination velocity. The secondary parameters have a small effect in this case; thus, the measured lifetime is taken as a lower bound on the bulk lifetime without any correction [35].

In the transient PCD mode, the measured lifetime is quite close to the bulk lifetime. Transient PCD measurement results taken immediately after the flash terminates (at MCD $> 10^{15}$ cm$^{-3}$) will be affected by surface recombination and yield a measured lifetime significantly lower than the bulk lifetime. Transient mode measurements do not require careful surface preparation as this method is relatively insensitive to differences in the SRV [35]. In the PCD mode, the carrier lifetime measured at a specific MCD is equal to the bulk lifetime [35].

## 4.2.2 Peltier Element

To enable temperature-dependent lifetime measurements, a Peltier element has been connected to the BCT-300 setup. The setup is capable of achieving temperatures from -10 °C to 200°C [42]. The accessible temperature range of the Peltier element using distilled water in the water bath is 5 to 95 °C, and the voltage needed is 230± 10% [42]. The power supplied in Norwegian power outlets is 230 V.

A Peltier element consists of two dissimilar cojoined thermoelectrical metals. These metals are normally an alternation of p-type and n-type semiconductor materials. The n-type and p-type doped semiconductors in a Peltier element are essential for creating the thermoelectric junctions. As thermal energy is applied to the junction one end will become hot and the other warm creating a temperature gradient [41].

When electrical energy is applied a temperature gradient proportional to the electrical current is created across the junction. The free electrons and holes redistribute themselves based on their thermal energy levels. The warmer side of the junction has more thermal energy, causing electrons to move from the n-type material to the p-type material, while the holes move in the opposite direction. This redistribution of charge carriers results in an electrical potential difference across the junction which generates an electrical current. The device is capable of transferring heat and can function as a cooler or heater, depending on the direction

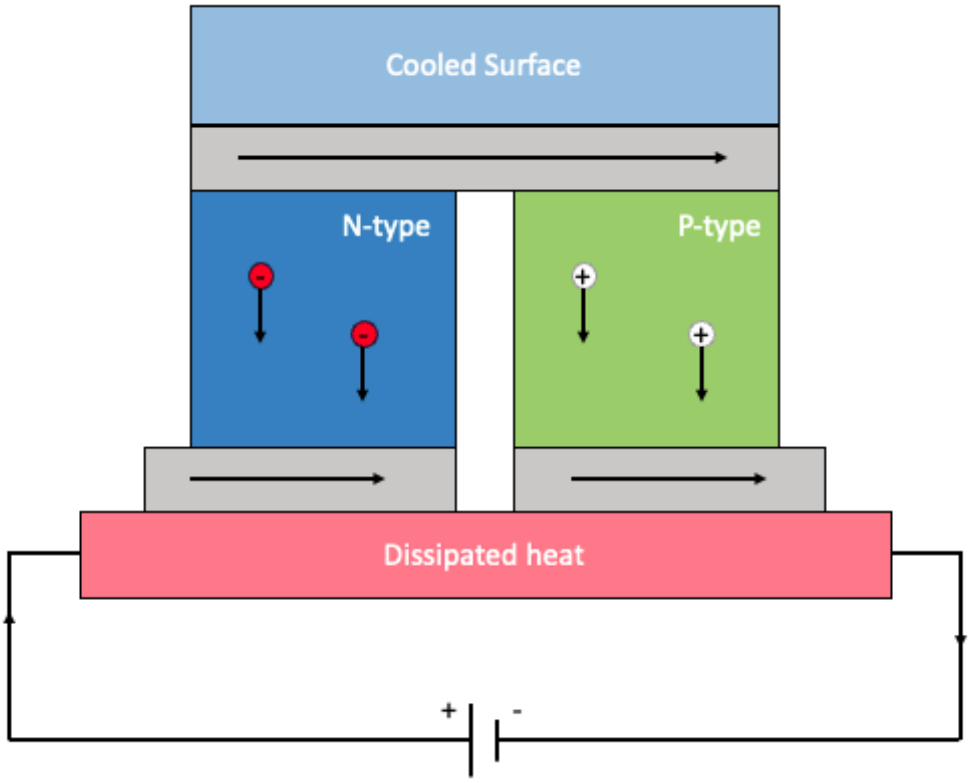


**Figure 4.12:** Schematic working principle of a Peltier element connected to a power source. The Peltier element consists of n-type and p-type semiconductor materials [41].

of the electric current [41].

By applying an electrical current at the junction of the two materials, heating or cooling is achieved as a temperature gradient is created. When a current flows through the materials, one of the materials will become cold and the other will become warm as illustrated in Figure 4.12. The Peltier element is then able to transfer heat from one side of the device to the other by using electrical energy. By changing the direction of the current, the Peltier element can function as a cooler. Peltier elements are however known to have a weak cooling capacity as a lot of electrical energy is required to achieve low temperatures [41].

### Lifetime measurements Using BCT-300 and a Peltier element

To enable lifetime measurements at various temperatures, a Peltier element has been coupled to the original BCT-300 setup (1 in Figure 4.10) used in Appendix 6.2. The Peltier element (seen as (3) in Figure 4.13) consists of a *Peltron* temperature regulator (2 in Figure 4.10) and a *Haake DC 10* temperature stabilizer (seen as (4) in Figure 4.13). To ensure electrical insulation between the copper plate and the sample, a 5 mm thick quartz plate has been mounted on top of the Peltier element, seen as (2) in Figure 4.10. To take a measurement the desired temperature has to be set on the temperature regulator. When the temperature has stabilized the sample to be measured can be carefully placed on the quartz plate. The correct filter for the sample measured, as well as the flash setting, has to be correctly set in order to achieve the most valid results. When the temperature has stabilized the BCT-300 instrument can be zeroed by pressing the "Zero Instrument" button. When the instrument has been zeroed, it can be placed on the sample and the measurement can take place. The BCT-300 should be left on the sample during all measurements in the desired temperature range to ensure accurate measurements.

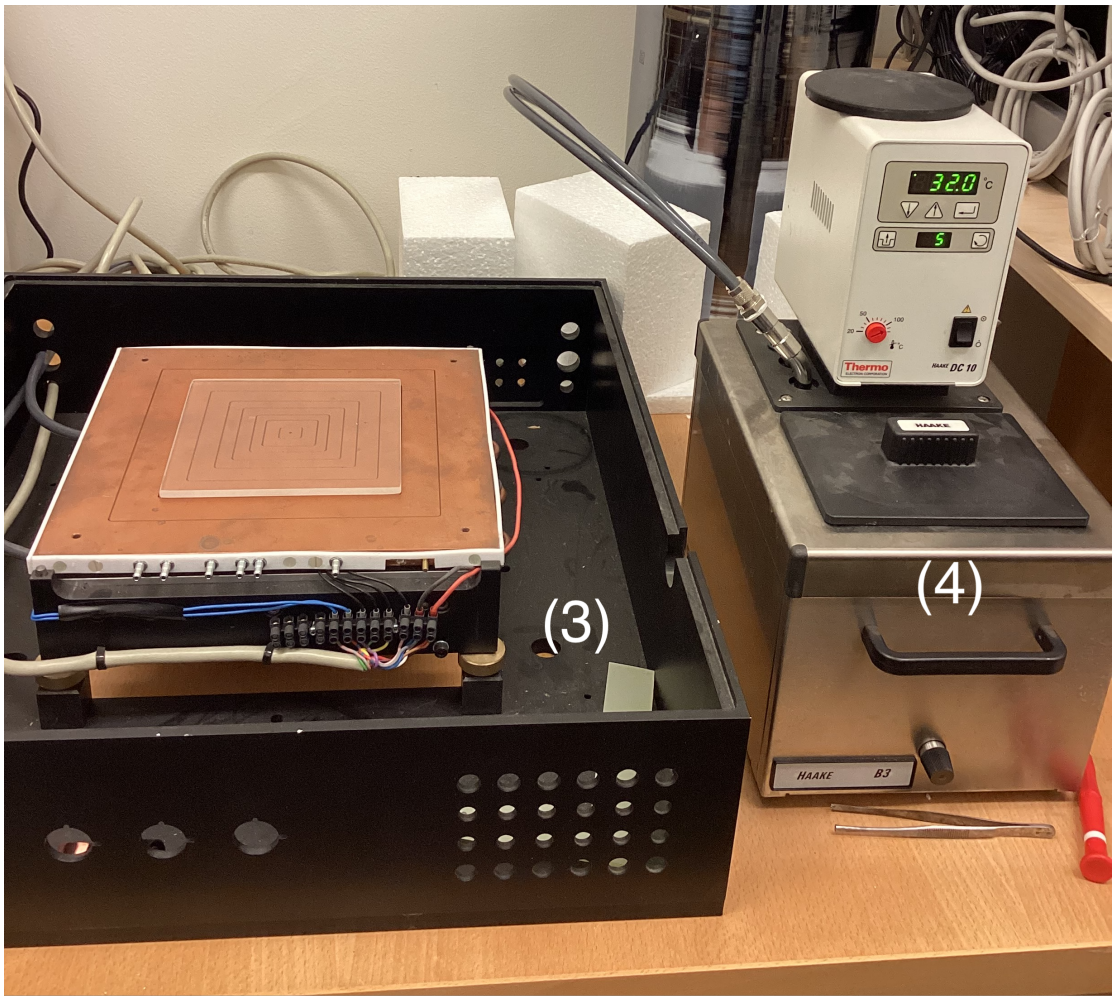


**Figure 4.13:** Experimental setup showing the Peltier element (3) with a connected water bath functioning as a temperature stabilizer (4).

CHAPTER

# FIVE

# RESULTS AND DISCUSSION

This chapter is divided into four parts. The first section (Section 5.1) presents the results obtained from the carrier lifetime measurements conducted on bricks and wafers. The second section (Section 5.2) compares the temporal stability of the stack passivation of a-Si:H/a-$Si_xN_y$:H of the two passivated wafers, 2T and FZ, which were measured once a week over a period of ten weeks. The last section (Section 5.3) outlines the results obtained from the TDLS analysis method to assess if the data obtained from the developed method can be used for such analysis.

To understand the figures presented in this chapter, a colour coding scheme is applied. Dark blue represents 10 °C, and dark red represent 75 °C. While taking measurements with the BCT-300, the instrument is first "zeroed", and placed on the sample when the temperature is stable, and then a measurement is conducted.

As temperatures below 20 °C were only possible to reach once a day, multiple samples were measured after each other at the same temperature. This means that the instrument was taken off the sample so that a new sample could be measured at the same temperature. It is important to note that this procedure may introduce a potential source of error. Given the spatial variations of the carrier lifetime within the sample, particularly for mc-Si samples, inconsistencies can be expected if the instrument is not placed in the exact same position [27, 22, 35]. Consequently, variations in carrier lifetimes due to different impurities at the grain boundaries must be considered as potential sources of error during measurements [35]. Notably, it was observed that this approach yielded erroneous results.

To mitigate this issue, an alternative approach was explored, wherein the instrument was left on the sample throughout the entire temperature range. This modification to the methodology yielded more accurate and reliable results and hence this approach was mainly used throughout all experimental work.

During the measurement process using the BCT-300 instrument, certain pro-

cedural steps have to be followed. Firstly, the instrument has to be calibrated. This is performed by following chapter 4.2.2 in Appendix 6.2. After the calibration, the instrument needs to be qualified to ensure accurate results. This procedure is performed in accordance with chapter 4.2.1 in Appendix 6.2. After these steps are performed the instrument has to be zeroed prior to each measurement, and the measurements can then be performed. Once the temperature of the temperature regulator is stable, the measurement can be carried out.

## 5.1 Lifetime measurements using the BCT-300 coupled with Peltier element

### 5.1.1 From the block

From the block displayed in Figure 4.1, three bricks and four wafers were measured. These samples were extracted from an ingot created in SINTEF's Heliosi lab, utilizing the Czochralski furnace. A block was cut from the ingot, from which eight samples were taken, designated B or T for the bottom or top of the block, respectively. The samples were numbered in ascending order, with the lowest number indicating the sample cut deepest into the block and the highest number representing the first cut sample. Samples that had a thickness of under 200 $\mu$m broke during the polishing process. For this reason, the thinnest wafers cut from the block have a thickness of 500 $\mu$m and only seven samples are measured.

#### Bricks

The three bricks, 15B, 14B, and 7T are displayed in Figure 4.2. The measured carrier lifetime as a function of injection level in a temperature range of 10-75 °C, is depicted in Figure 5.1. The three bricks display different carrier lifetimes, and sample 15B is observed to have the overall lowest lifetimes. The reason for the difference in lifetimes measured from the three samples can be related to structural defects and impurities in the material [28]. The temperature influence on all the bricks individually is displayed in figure 5.2 - 5.4.

Figure 5.2 - 5.4 illustrates the temperature-dependent carrier lifetime as a function of injection level on the three bricks denoted 15B, 14B, and 7T, respectively, in a temperature range of 10-75 °C. All three bricks are monocrystalline silicon and are dominated by the SRH recombination mechanism [14]. The three bricks display an increase in carrier lifetime with increasing temperature. This trend is in accordance with the theory in Section 2.2.2, where it is stated that a material dominated by the SRH recombination mechanism will see an increase in the carrier lifetime as the temperature increases at LLI. In addition, the BCT-300 measures the change in conductivity in the sample, and as the temperature increases the conductivity increases. The increase in conductivity results in a higher excess carrier density seen from Equation 3.2, which again results in a higher carrier lifetime measured, seen from Equation 2.16.

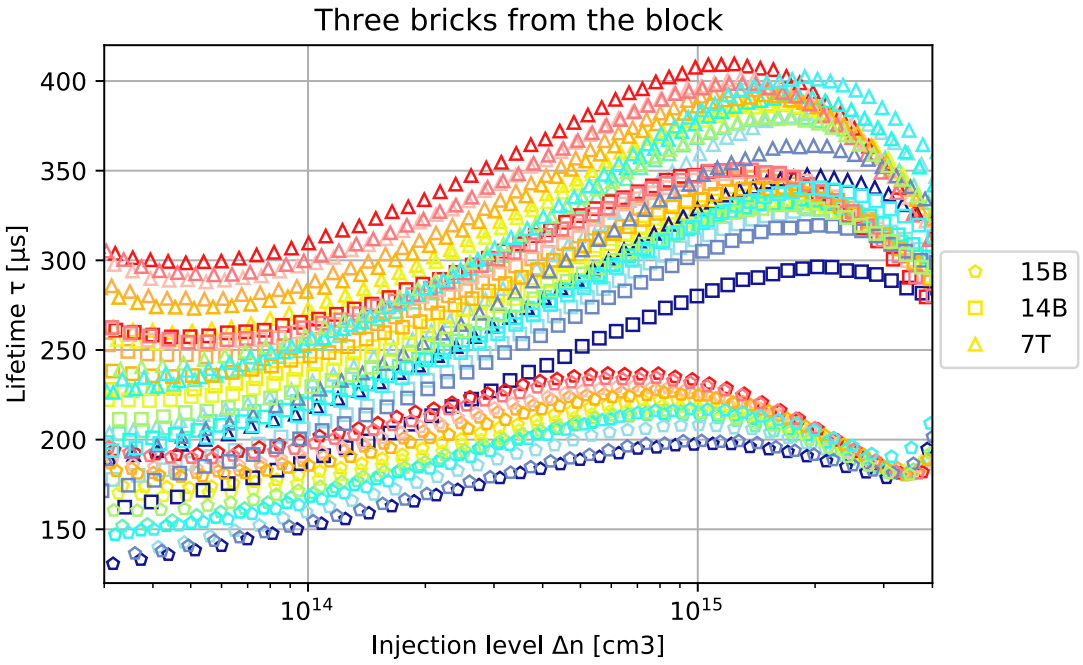


**Figure 5.1:** The temperature-dependent carrier lifetime as a function of injection level of the three bricks from the block (Figure 4.2) measured in a temperature range of 10-75 °C. The bricks are p-type boron-doped monocrystalline Cz samples. The sample 7T is observed to have the highest measured carrier lifetime and 15B is observed to have the lower measured carrier lifetime in the temperature range.

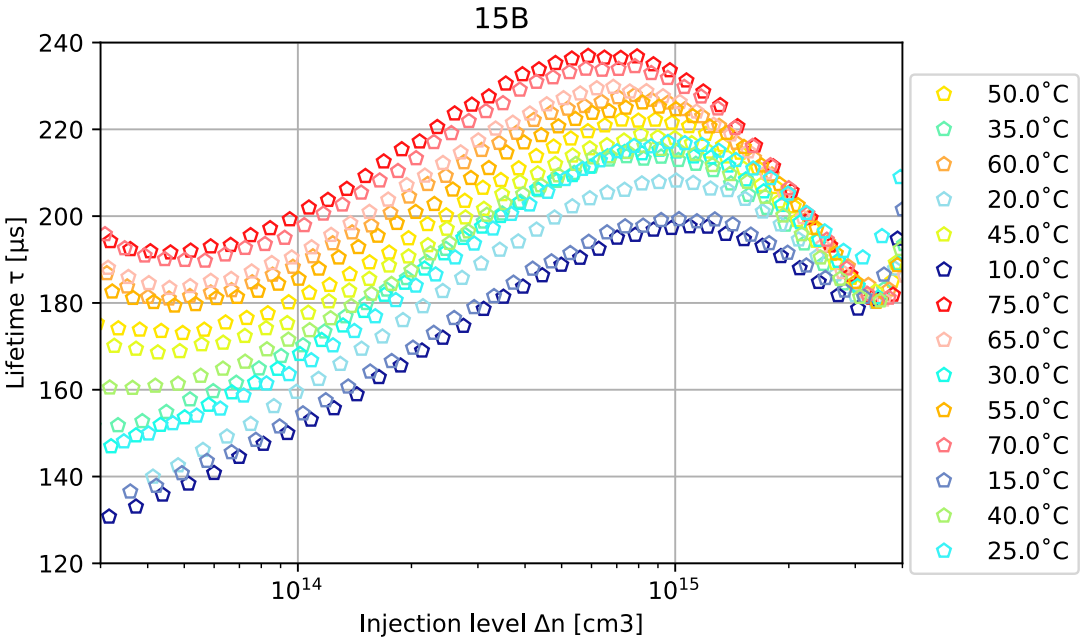


**Figure 5.2:** The sample 15B (seen in Figure 4.2) is a p-type boron doped Cz brick from the block (seen in Figure 4.1), measured from 10-75 °C. The graph illustrates the temperature-dependent carrier lifetime as a function of injection level, and it is observed that the temperature dependence of the carrier lifetime is in accordance with the SRH-equation in the LLI region.

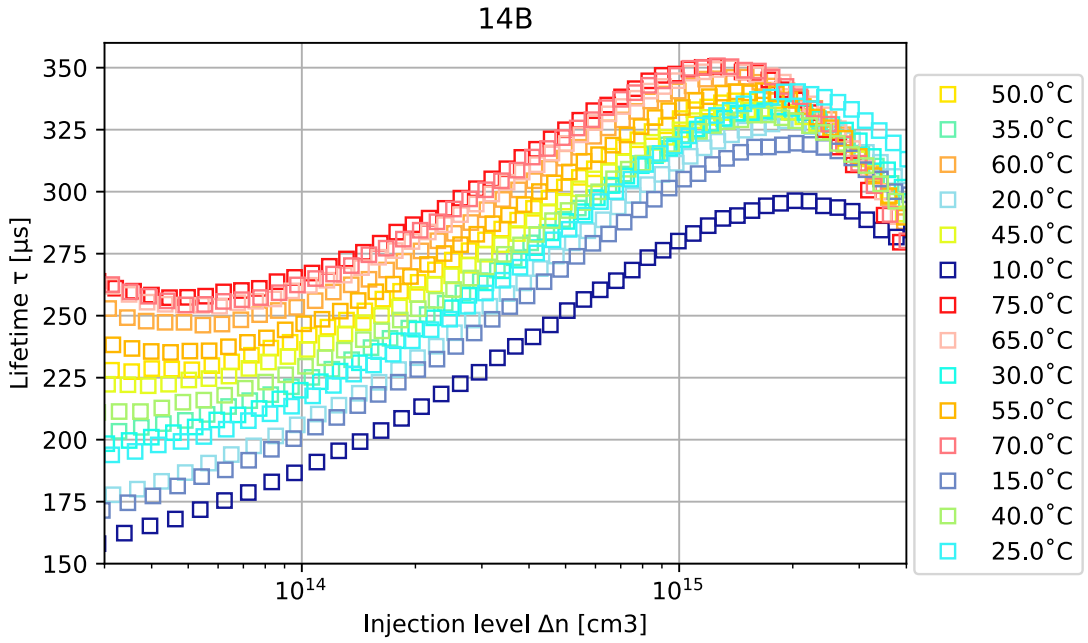


**Figure 5.3:** The sample 14B (seen in Figure 4.2) is a p-type boron doped Cz brick from the block (seen in Figure 4.1), measured from 10-75 °C. The graph illustrates the temperature-dependent carrier lifetime as a function of injection level, and it is observed that the temperature dependence of the carrier lifetime is in accordance with the SRH-equation in the LLI region.

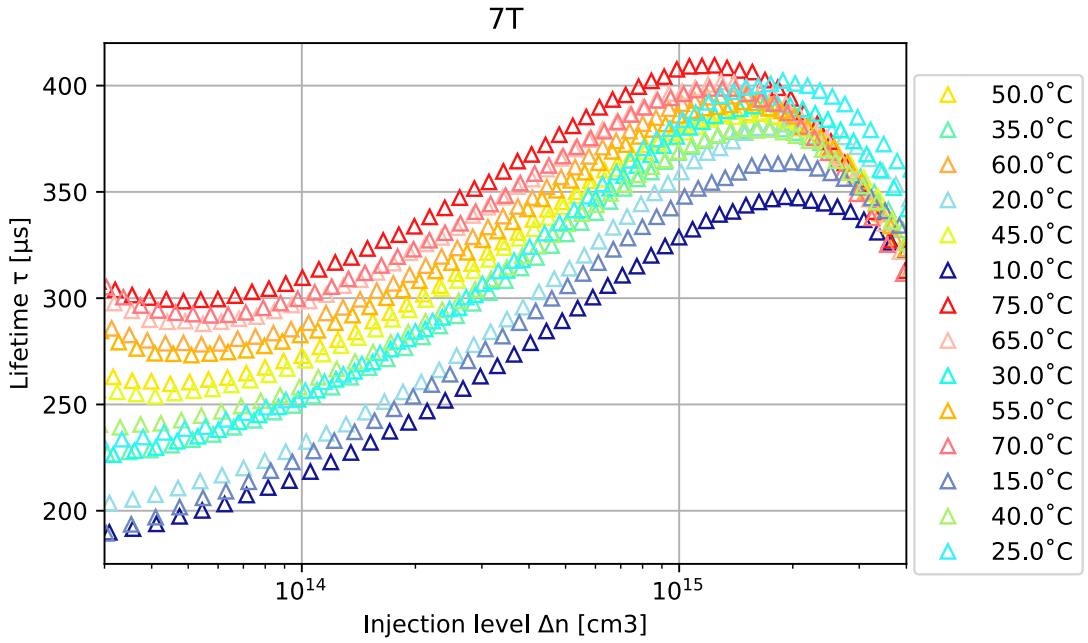


**Figure 5.4:** The sample 7T (seen in Figure 4.2) is a p-type boron doped Cz brick from the block (seen in Figure 4.1), measured from 10-75 °C. The graph illustrates the temperature-dependent carrier lifetime as a function of injection level, and it is observed that the temperature dependence of the carrier lifetime is in accordance with the SRH-equation in the LLI region.

### Wafers

The four wafers from the block, 5T, 9B, 12B, and 2T displayed in Figure 4.3 are stack passivated with an a-Si:H/a-Si$_x$N$_y$:H using the PECVD passivation method described in Section 2.2.3. These samples were also measured as part of the specialization project (Appendix 6.2) where it was found that the Carrier lifetime in the samples increased with increasing thickness, meaning that 5T (970 $\mu$m) and 12B (968 $\mu$m) should exhibit higher lifetimes compared to the 9B (557 $\mu$m) and 2T (500$\mu$m) of these four wafers [16].

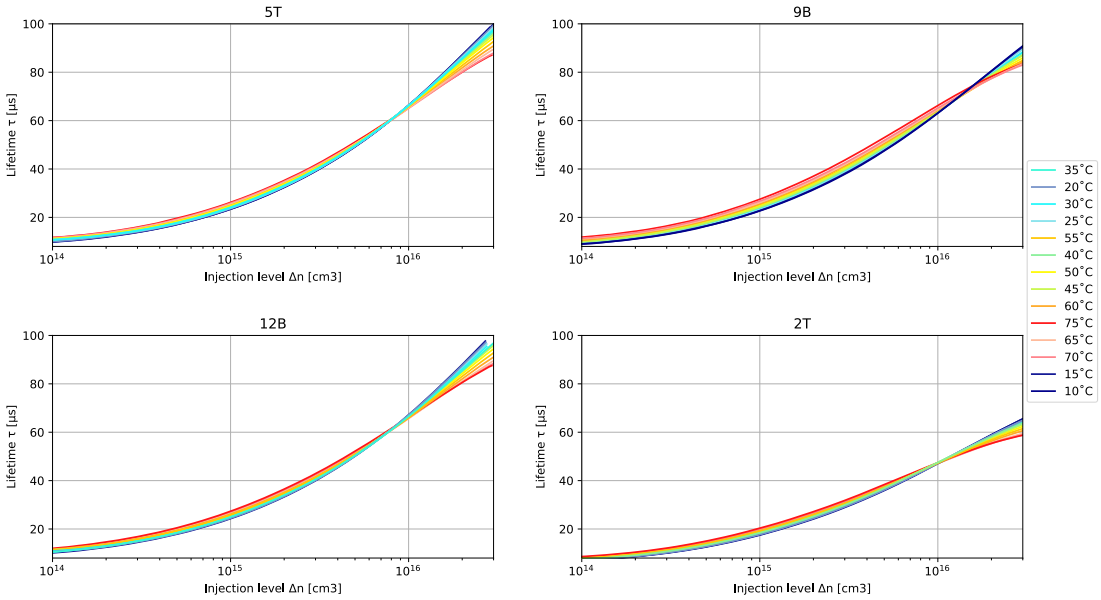


**Figure 5.5:** The samples 5T, 9B, 12B, and 2T (seen in Figure 4.3) are p-type boron doped Cz wafers from the block (seen in Figure 4.1), measured from 10-75 °C. The samples are passivated with a-Si:H/a-Si$_x$N$_y$:H. The graphs illustrate the temperature-dependent carrier lifetime as a function of the injection level. It is observed that the temperature dependence of the carrier lifetime is in accordance with the SRH-equation in the LLI region.

The temperature-dependent carrier lifetime measured in a temperature range of 10-75 °C, is illustrated in Figure 5.5. From Figure 5.5 it is observed that the samples 5T and 12B present the highest lifetimes among the four measured wafers. This observation is consistent with the theoretical deduction presented in Equation 2.17, which indicates that the thickness of the sample affects the carrier lifetime, with thicker samples resulting in higher measured lifetimes. Specifically, the wafers 5T and 12B have approximately twice the thickness of wafers 2T and 9B and will thus exhibit a longer lifetime compared to the thinner samples. As the wafers are passivated the difference in lifetime may be attributed to a nonuniform passivation layer meaning that more carriers recombine at the surface where the passivation layer is not fully saturating the dangling bonds. The passivation of the samples was conducted in January (2023) and the measurements taken on these four samples were completed in June (2023). Through this time the passivation layers might have degraded. However, in accordance with scientific literature, the

temporal stability of the stack passivation layer of a-Si:H/a-Si$_x$N$_y$:H after 1600 hours suggests that the carrier lifetime measured should have recovered about 100% of the initially measured carrier lifetime after passivation [21]. This is further elaborated in Section 5.2.

The temperature dependence of the carrier lifetimes of the samples exhibits the typical SRH-temperature-dependent trend in the LLI region which is also found to coincide with scientific literature [22, 14, 37]. The four graphs in Figure 5.5 display a trend where the carrier lifetime increases with temperature up to a specific injection level from where the trend changes. This change is observed when the injection levels are close to the doping level of each sample (see Table 4.1). In the LLI region, the excess carrier density is smaller than the doping concentration and the temperature dependence of the carrier lifetime is represented by the SRH-equation found in Equation 3.9. In the HLI region, the excess carrier density is comparably larger than the doping concentration. In this regime, the SRH lifetime is given by Equation 3.11 and does not necessarily increase with increasing temperature [14]. Additionally, in the HLI regime, other recombination mechanisms may also become more prominent [14].

### 5.1.2 Not from the block

#### Bricks

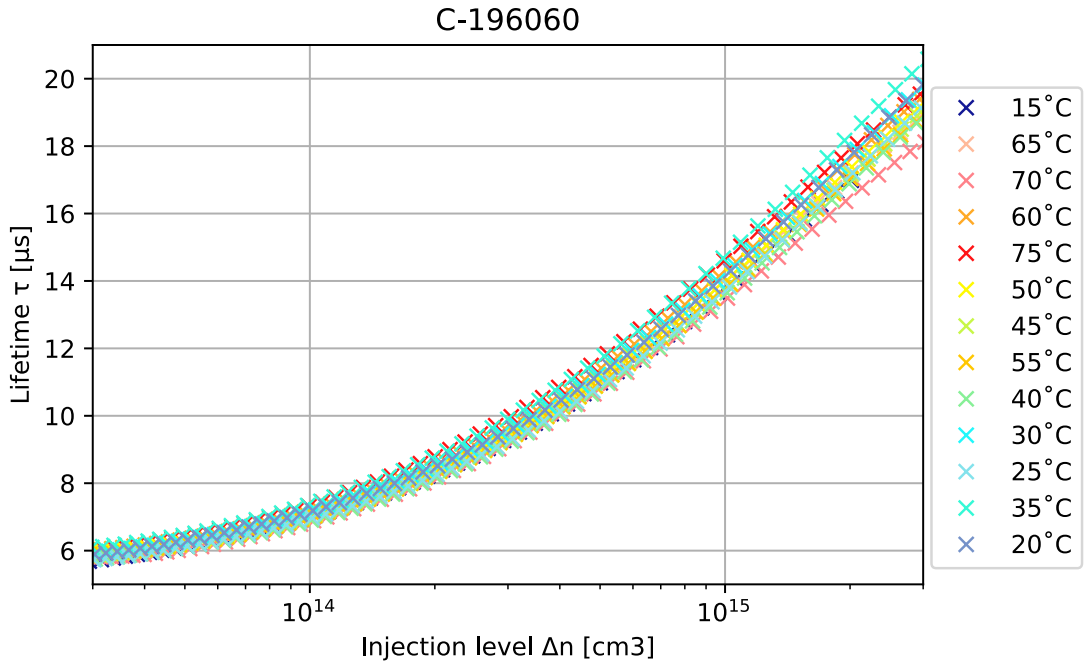


**Figure 5.6:** The C-196060 is a p-type boron doped monocrystalline brick, seen in Figure 4.4). The graph illustrates the measured carrier lifetime as a function of injection level. The carrier lifetime was measured in a temperature range from 15-75 °C. The graph does not display a clear temperature dependence of the carrier lifetime.

The C-196060 brick is displayed in Figure 4.4 and the temperature-dependent carrier lifetime as a function of injection level is illustrated in Figure 5.6. The temperature range measured for this sample is 15-75 °C. The measurement results of this sample do not display the expected temperature dependence in accordance with the SRH-equation in Equation 3.9. From Table 4.2 it is seen that the carrier lifetime is measured in a region that is much smaller than the doping concentration, meaning that the measurement is conducted in the LLI region. In the LLI region, the expected temperature dependence of the carrier lifetime should be in accordance with the SRH-equation in the LLI region given in Equation 3.9. At higher temperatures, the concentration of mobile charge carriers increases due to an increase in thermal energy, leading to an increase in thermalization events that occur when an electron-hole pair recombines. Moreover, the reduction in band gap energy at elevated temperatures results in a lower energy requirement for exciting charge carriers, which can further enhance the rate of Auger recombination. This deviation from the expected SRH temperature dependence of carrier lifetime in the LLI region can be attributed to the presence of other recombination mechanisms such as the impact of Auger recombination on the recombination rate.

Other factors that can influence the temperature dependence of the carrier lifetime are related to defects in the material, which can be activated at higher temperatures resulting in shorter lifetimes [14]. Defects that lie close to the Fermi level result in a slowing down of the temperature dependence of the carrier lifetime which might be the reason for the observed carrier lifetime measured from the C-196060 sample [29].

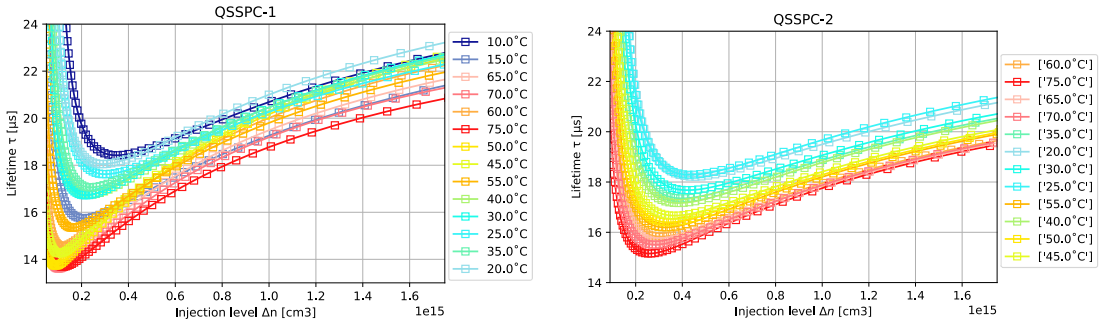


**(a)** **(b)**

**Figure 5.7:** The QSSPC-1 and QSSPC-2 samples (seen in Figure 4.9) are P-type boron doped mc-Si samples produced through directional solidification and have a thickness of 1.5 cm. The temperature-dependent carrier lifetime is measured in a temperature range of 10-75 °C. The carrier lifetime is seen to decrease with increasing temperature.

The temperature-dependent carrier lifetime as a function of the injection level of the samples QSSPC-1 (Figure 4.9a), and QSSPC-2 (Figure 4.9b) are displayed in Figure 5.7a and Figure 5.7b, respectively. These samples are p-type, boron-doped, mc-Si brick samples produced through directional solidification. The QSSPC-1 and QSSPC-2 exhibit lifetimes of 14-25 $\mu$s compared to the bricks from the block (seen in Figure 5.2 - 5.4) which exhibit a carrier lifetime of 130-400 $\mu$s.

The reason for the lower carrier lifetimes measured for the mc-Si bricks can be attributed to the grain boundaries and crystal structure of the samples. The grain boundaries represent areas of unbonded atoms, which means that mc-Si has a high concentration of unbonded atoms where charge carriers can recombine resulting in a lower carrier lifetime [9]. The impurities can connect to the unbonded atoms in the material and the concentration of impurities is higher compared to monocrystalline silicon samples. This will generally result in a shorter measured carrier lifetime for mc-Si samples and more surface recombination will take place in areas with grain boundaries. From Section 2.2.4 it is known that the grain boundaries in mc-Si samples result in variations in the minority carrier lifetime.

Both the QSSPC-1 and QSSPC-2 samples display a decreasing carrier lifetime with increasing temperature as a function of injection level. One reason for this can be attributed to the grains in the mc-Si sample which act as barriers. As temperature increases, the carriers' mobility decreases due to the limited space imposed by grain boundaries, resulting in a reduced band gap [9]. A study by Søndegaard et. al explained that mc-Si samples where the lifetime decreased with increasing temperature could be related to the impurities in the material, and the ingot position as more impurities will ensemble at the top of the ingot [43]. For the QSSPC-1 and QSSPC-2 samples, no information about the ingot position was given. However, as the lifetime decreases with increasing lifetime it is possible to conclude that the concentration of impurities in the samples influences the carrier lifetime in such a way that it decreases with increasing temperature. A study by Mathur P., et al explains that a decrease in a lifetime with an increase in temperature can be a result of predominant btb recombination processes [29]. However, the injection level and temperature measurement are too low for Auger recombination to be dominant, and as silicon is an indirect band gap material, radiative btb recombination is not present. The doping concentration of these two samples seen in Table 4.1 suggest that the measured carrier lifetime is in the LLI region. In the LLI region, it is expected to see an increase in carrier lifetime with increasing temperature in accordance with the SRH-equation.

The temperature dependence observed in the two samples can be attributed to the positioning of the BCT-300 instrument on the sample surface. The carrier lifetime measured at a specific temperature may vary due to different positions on the sample surface, thus capturing spatial variations within the sample caused by grain irregularities. Therefore, it is crucial to maintain a consistent positioning of the BCT-300 instrument throughout all measurements. The two measured monocrystalline silicon (mc-Si) bricks had a width of 5 cm, which is smaller than the width of the instrument, but sufficient to be covered by the coil. However, the instrument's placement was carried out without certainty that the RF sensor coil completely covered the entire sample. No part of the coil was observed to extend beyond the sample surface, indicating that this arrangement was satisfactory. If the sensor coil extends beyond the sample surface, the software shuts down. To continue measurements after a shutdown, the instrument must be zeroed.

**wafers**

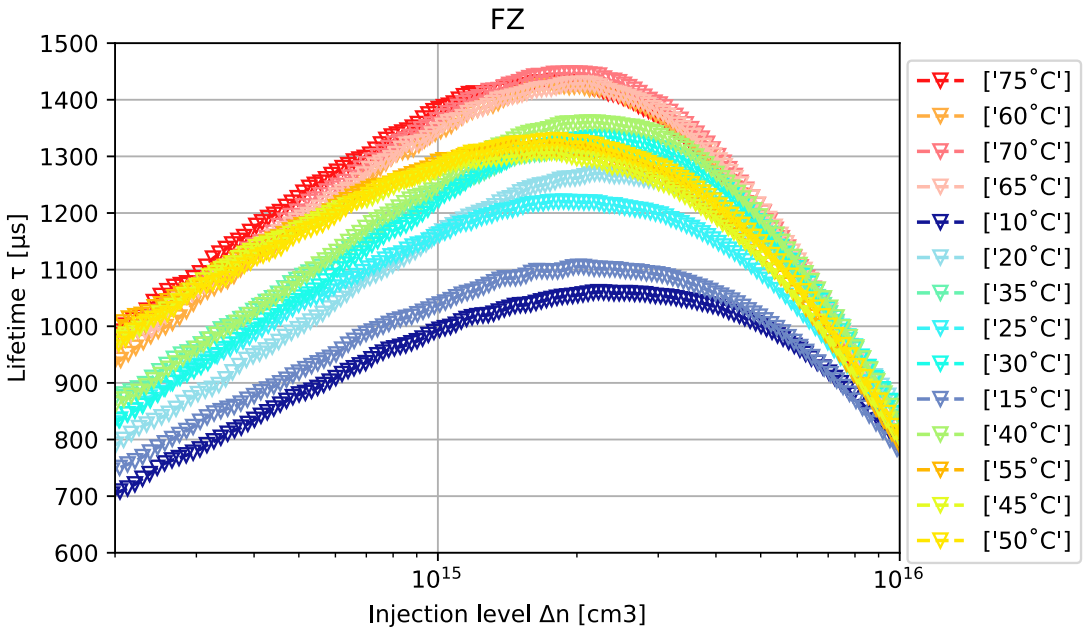


**Figure 5.8:** The FZ wafer (seen in Figure 4.5) has a diameter of 5 cm and is a p-type boron doped monocrystalline silicon sample produced through the float zone process described in Section 2.2.4. The graph displays the temperature-dependent carrier lifetime as a function of the injection level for the FZ wafer. The carrier lifetime is seen to increase with increasing temperature aligning with the SRH-equation in the LLI region.

The carrier lifetime measurements performed on the FZ-sample (seen in Figure 4.5) are illustrated in Figure 5.8. The sample is a p-type boron-doped monocrystalline sample produced through the float zone process as described in Section 2.2.4. The sample exhibits a temperature-dependent carrier lifetime in accordance with the SRH-equation in the LLI region. From Table 3.1 it is observed that the measured carrier lifetime is below the doping concentration meaning that the measured carrier lifetime is in the LLI region. The expected trend is an increase in carrier lifetime with increasing temperature, also found in the literature [22, 14].

The lifetime measurements on the unpassivated IC wafers (seen in Figure 4.6a) are displayed in Figure 5.9a and the passivated IC wafers (seen in Figure 4.6b) are displayed in Figure 5.9b. It is important to note that the passivated and unpassivated samples are not identical, hence the designation x1 and x2 on the passivated samples. The passivation process was carried out in January through the process described in Section 2.2.3. According to scientific literature, the passivation layer should not have undergone degradation at this stage [21].

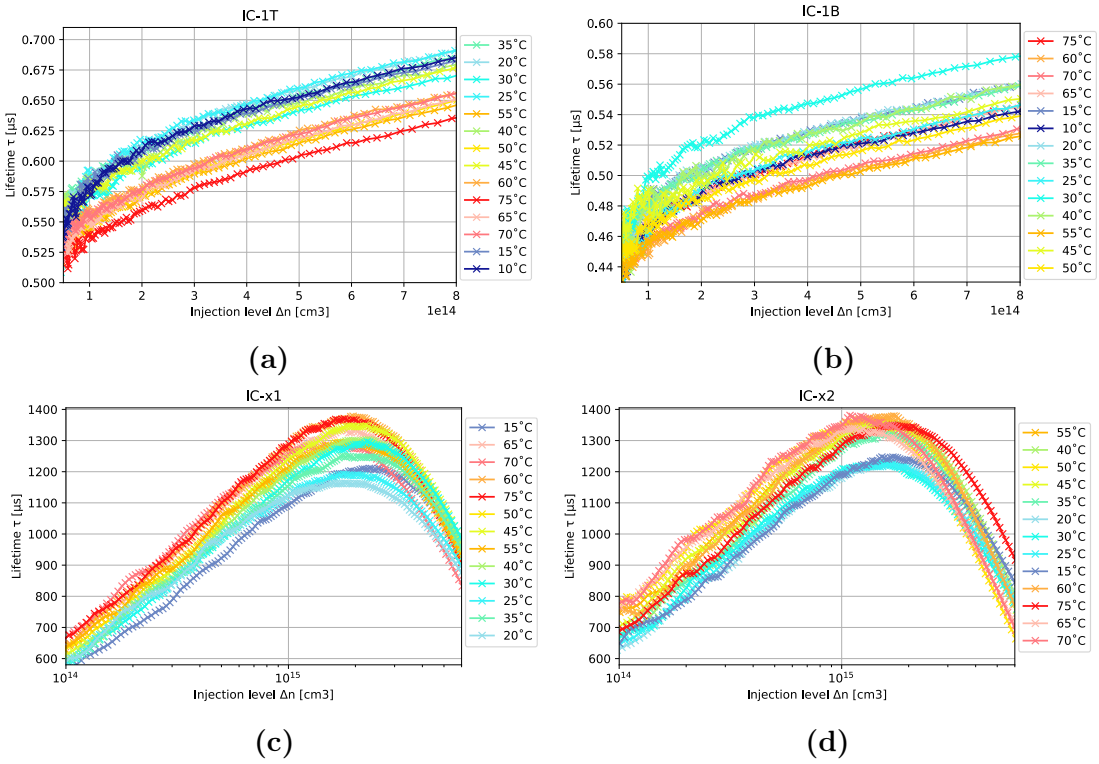


**Figure 5.9:** The measured carrier lifetime as a function of injection level in a temperature range of 10-75 °C, on the IC samples. The IC-1T and IC-1B are unpassivated p-type boron-doped monocrystalline Cz wafers. The trend observed for the two unpassivated wafers in Figure 5.9a and 5.9b are not in accordance with the SRH-equation in the LLI region. The two wafers IC-x1 and IC-x2 are stack with a-Si:H/a-$Si_xN_y$ in accordance to the process described in Section 2.2.3. Figure 5.9c and 5.9d. The carrier lifetime for the passivated samples is observed to increase with increasing temperature in aligning with the SRH equation in the LLI region.

The measured carrier lifetime for the unpassivated IC-samples, namely IC-1T and IC-1B displayed in Figure 5.9a and Figure 5.9b respectively, are generally very low. The carrier lifetime as a function of injection level for these two samples is subject to fluctuations and instability. These fluctuations arise from the saturated reference cell in the BCT-300 instrument, which means that the instrument is not able to accurately measure the carrier lifetime for these samples. This can be attributed to the measuring limits of the instruments which are 1 $\mu$s.

The carrier lifetimes measured as a function of temperature do not show a clear temperature dependence. Since the samples are unpassivated, the concentration of impurities and unbonded atoms is higher compared to the passivated IC wafers (Figure 5.9c-5.9d), which display a much higher lifetime. The influence of passivation on the carrier lifetime is explored in a previous study and an increase in the carrier lifetime was observed after the samples were passivated [16]. This increase is related to the saturation of unbonded atoms in the unpassivated samples, resulting in reduced or no surface recombination in the sample seen from Equation 2.29.

The passivated samples, IC-x1 (Figure 4.6a top) and IC-x2 (Figure 4.6a bottom), are displayed in Figure 5.9c and Figure 5.9d, respectively. The samples display an increase in the carrier lifetime with an increase in temperature. This means that the temperature dependence of the carrier in these samples is in accordance with the SRH equation in the LLI region. From Table 4.1 the doping concentrations for the samples can be found and we can conclude that the measured carrier lifetimes are in the LLI region. From Figure 5.9c and Figure 5.9d it is observed that the increase in carrier lifetime with increasing temperature takes place when the excess carrier density is lower than the doping concentration in the sample (found in Table 4.1) meaning that the carrier lifetime measured for these two samples are in the LLI region. These findings are also reported in literature [22, 14]

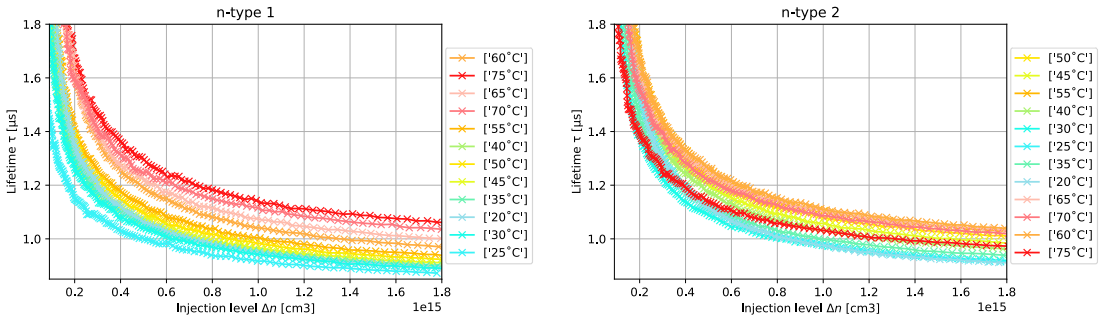


**(a)** **(b)**

**Figure 5.10:** The graphs display the temperature-dependent carrier lifetime as a function of injection level for the sample n-type 1 (5.10a) and n-type 2 (5.10b). These samples are n-type phosphorus-doped monocrystalline Cz wafers, displayed in Figure 4.7. The graph displays the temperature-dependent carrier lifetime as a function of injection level for the sample n-type 2. The samples are phosphorus-doped n-type Cz wafers, as displayed in Figure 4.7b. The overall temperature dependence on the carrier lifetime is in accordance with the SRH-equation in the LLI region.

The temperature-dependent carrier lifetime as a function of injection level on the n-type samples is displayed in Figure 5.10. The n-type 1 (Figure 4.7a) and n-type 2 (Figure 4.7b) are n-type, phosphorus-doped monocrystalline silicon samples. From Figure 5.10 it is observed that the measured minority carrier lifetime is very low, under 2 $\mu$s. This short lifetime can be attributed to the fact that these samples are not passivated meaning that more impurities can connect to the material through the unbonded atoms at the surface edges of the sample.

The obtained temperature dependence of the n-type 1 sample is in accordance with the SRH-equation in the LLI region, which is also observed in scientific literature [44]. The doping concentration is $3.227\times10^{15}$ cm$^{-3}$ and it is observed that the injection level in Figure 5.10a is smaller than the doping concentration. Thus most of the measured lifetimes are in the LLI region. The temperature dependence after exceeding the doping concentration shows a less clear temperature trend due to other recombination mechanisms becoming more prominent in this region.

The measured carrier lifetime as a function of injection level at various temperatures for the sample n-type 2 is displayed in Figure 5.10b. The temperature-dependence of the carrier lifetime is for this sample not as clear compared to the n-type 1 sample. However, the overall trend observed is that the carrier lifetimes measured at lower temperatures are lower compared to those at higher temperatures where a higher carrier lifetime is measured. The doping concentration of the sample n-type 2 is equal to the doping concentration of the n-type 1 sample. For this reason, it is also observed here that the carrier lifetime is measured in the LLI region, and according to Equation 3.10 the carrier lifetime should see an increase with increasing temperature. For this sample the temperature dependence when the injection level exceeds the doping concentration displays a less clear temperature trend. The ambiguity of the measurement at 75 °C can be related to errors within the BCT-300 instrument such as unconscious moving of the instrument due to the many cords connected to the instrument (seen in Figure 4.10) or due to activation of defects in the material [35].

The temperature-dependent carrier lifetime measurements of the mc-Si samples Multi-grain (Figure 4.8a) and m-cryst wafer (Figure 4.8b) are displayed in Figure 5.11a and Figure 5.11b, respectively. The multi-grains sample was measured in the given temperature range from 10-75 °C. The m-cryst was measured after the multi-grains starting from 75 °C. However, it is important to note that due to limitations in the experimental setup, the desired temperature of 10-15 °C is only achievable once per day. This limitation is attributed to insufficient power supplied to the Peltier element, which could potentially be caused by aged equipment leading to a slight degradation in performance. As a result, the m-cryst sample is solely measured within the temperature range of 20-75 °C.

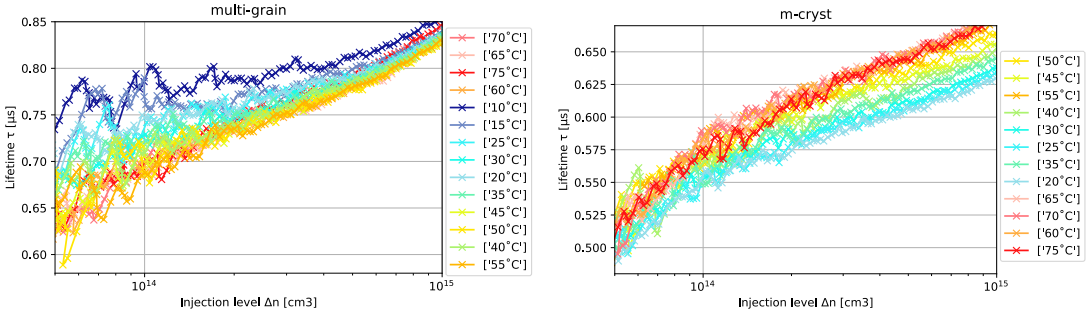


**(a)** **(b)**

**Figure 5.11:** The graphs display the temperature-dependent carrier lifetime as a function of injection level for the multi-grains (Figure 5.11a) and m-cryst (Figure 5.11b) samples in a temperature range of 10-75 °C. The measured carrier lifetime of the multi-grains sample show instability and no clear temperature dependence in accordance with the SRH-equation in the LLI region. The measured carrier lifetime of the m-cryst sample show instability in measurements however the carrier lifetime increases with increasing temperature aligning with the SRH-equation in the LLI region.

The carrier lifetime measured on the multi-grains sample is very low and does not exhibit a clear temperature-dependent trend on the carrier lifetime as a func-

tion of injection level (as seen in Figure 5.11a). However, at elevated temperatures, the lowest lifetimes are observed, while the highest lifetimes are recorded at lower temperatures. The data obtained shows fluctuations and instability, and this can be related to the reference cell in the instrument becoming saturated, which is related to the limit of the instrument. This poses challenges for the instrument in accurately measuring the signal. The absence of clear temperature dependence in the carrier lifetime with respect to the injection level can be ascribed to the presence of defects and impurities within the material, as noted in a prior study [43].

The m-cryst sample displays an increasing lifetime with increased temperature as a function of injection level (as seen in Figure 5.11b). This aligns with the theoretical predictions based on the SRH equation in the LLI regime. This trend is also found in scientific literature [45]. The doping concentration for the m-cryst sample is observed to be higher than the injection level. Consequently, the measured carrier lifetime corresponds to the LLI region.

## 5.2 Temporal stability of FZ and 2T

Temporal stability measurements were conducted on two wafers, specifically the 2T sample and the FZ sample. The temperature-dependent carrier lifetime, as a function of injection level, was assessed every week over a span of 10 weeks. The obtained results are displayed in Figure 5.12a and Figure 5.12b, representing the temporal stability of the FZ and 2T samples, respectively.

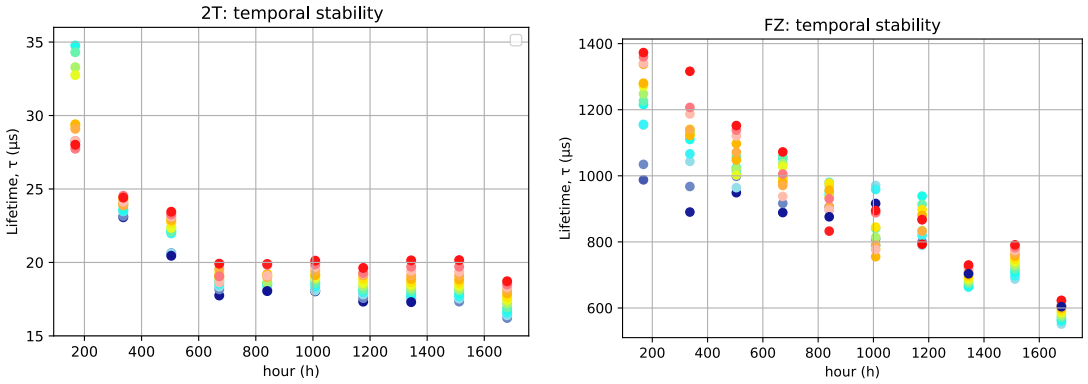


**(a)** **(b)**

**Figure 5.12:** Temporal stability measurements of the Si:H/a-$Si_xN_y$ stack passivated 2T (Figure 5.12a) and FZ (Figure 5.12b) samples are displayed in Figure 5.12a and Figure 5.12b, respectively. The measurements include measuring the carrier lifetime at a fixed injection level in a given temperature range of 10-75 °Cand have been performed once a week for a period of ten weeks. The colour coding represents the temperatures where dark blue is 10 °C, and red is 75 °C.

Both the 2T and FZ samples depict a noticeable decline in a lifetime during the initial 600-hour period. This decrease is expected, as observed in the scientific

literature [21]. The degradation can be attributed to weak Si-H bonds within the a-Si:H films, which are influenced by light and temperature, allowing environmental impurities to interact with the material [21]. The 2T wafer shows stabilization after 600 hours at 50% from the initially measured carrier lifetime. According to the literature, it is expected that this stack passivation will recover to 85-100% of its initial value [21]. This is related to the passivation layers as the a-Si:H of 40nm is less sensitive to environmental effects, and the top layer of a-$Si_xN_y$ functions as a block for hydrogen effusion out of the passivation stacks [21].

During the initial stages of the experimental work, certain measurements were performed using a procedure that involved removing the instrument from the sample after each measurement, to measure both samples at low temperatures. Consequently, the measurements obtained within the first three weeks exhibit significant variations and demonstrate a notable decline in quality. This inconsistency in measurement results can likely be attributed to the measurement method employed during this early phase as the samples exhibit spatial variations in the carrier lifetime [39, 46].

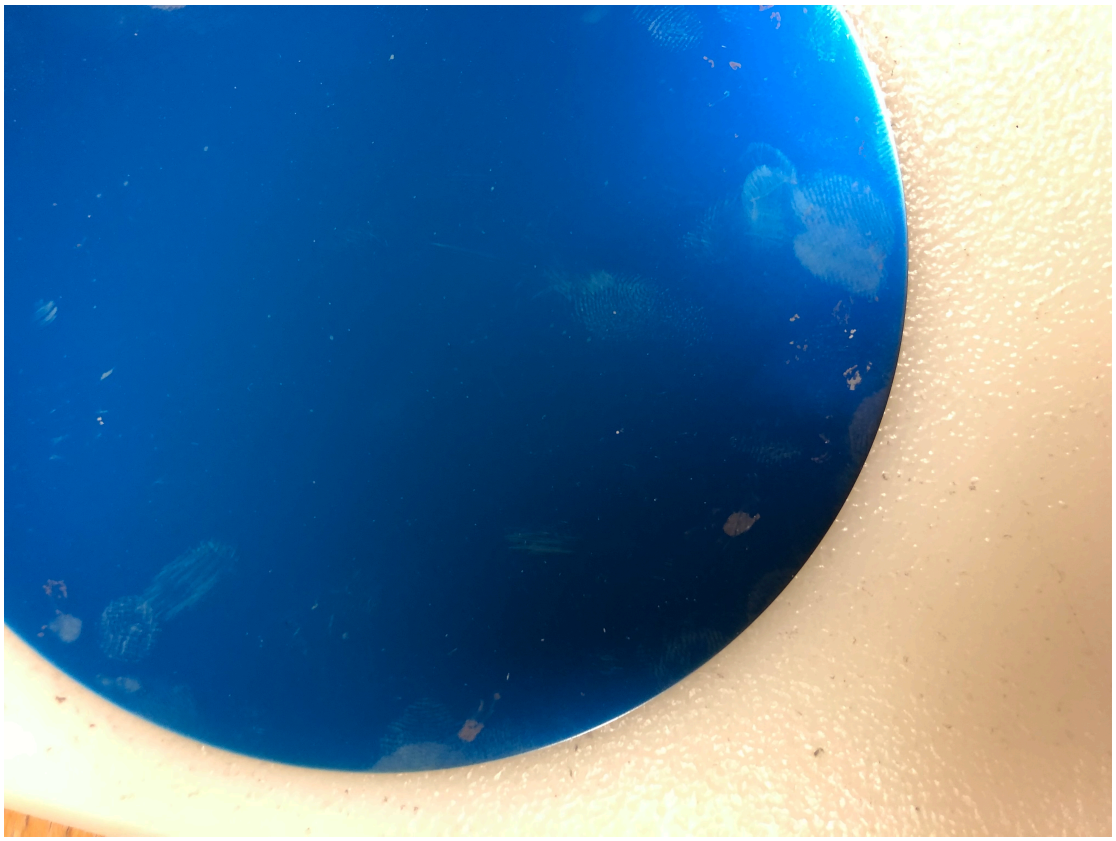

**Figure 5.13:** Scratches and marks that formed on the FZ sample surface around week 6.

The degradation of the FZ wafer does not exhibit a stabilization as the 2T sample. Starting from week 6, certain areas on the sample exhibited noticeable marks and damages to the passivation layer as seen in Figure 5.13. This occurrence could potentially introduce additional instability and unreliability in the results obtained as these areas contain unbonded atoms. The reason is that in these areas

where the passivation layer is no longer present, impurities from the environment can connect to the material. This can potentially result in a decrease in the measured carrier lifetimes.

The temperature dependence of the carrier lifetime of the FZ sample becomes less apparent after 800 hours. This can be attributed to impurities connecting to the material or preexisting defects within the material that undergo chemical transformations under illumination, resulting in a change in the carrier lifetime [35]. One such defect is the boron-oxygen defect, which remains unchanged under illumination flash but can be activated when exposed to indoor lighting for extended periods [35]. In the temperature dependence analysis of the FZ sample, it is noteworthy that measurements conducted at 10 °C deviate from the expected trends observed at other temperatures. These particular measurements exhibit anomalous behaviour, distinct from the overall clear trends observed in the temperature dependence of other measured temperatures.

While the FZ and 2T samples were stored in opaque containers on a day-to-day basis, both samples were exposed to indoor lighting during the days when measurements were conducted. This exposure may have caused light-induced changes in the materials which can result in activation of certain defects [21, 26]. One article observed degradation of a float-zone monocrystalline phosphorus-doped sample by close to 40% after 1-sun light soaking up to 500h [26]. The light-induced degradation observed is explained through the changes driven by the dangling-bond density [26]. This is also observed in other scientific research where it is found that increased light exposure results in an increase in the dangling bonds (recombination centre density) which in turn results in the degradation of the material's electronic quality [47]. As the passivation degrades, more impurities are influenced by previous illuminations which will result in lower measured carrier lifetimes. Therefore, by applying high temperatures to the sample the passivation layer might degrade more.

## 5.3 TDLS

The TDLS analysis was performed on the three bricks, and the four wafers from the block, the FZ, IC-x1, IC-x2, and m-cryst wafer. The TDLS analysis is performed through a linear fit of the measured carrier lifetime at each temperature step using Equation 3.16. Each sample's calculated defect energy levels (trap levels) are given in the title of the obtained graphs presented in position from the VB. The TDLS analysis is only performed on the samples in Section 5.1 that exhibit increased carrier lifetime with increasing temperature. The reason is that the TDLS analysis is based on the SRH-equation in the LLI region where the temperature dependence of the carrier lifetimes exhibits an increasing carrier lifetime with increasing temperature which forms the basis of the Equation 3.16. The TDLS analysis is performed by evaluating the LLI lifetime at a fixed injection level in accordance with Table 4.2. The intercept $N_C/N_A + \log(\tau_{n0})$ presented in Equation 3.16 assumed constant.

The purpose of this chapter is to see if the developed method for measuring temperature-dependent carrier lifetime as a function of injection level, can be used to perform simple TDLS analysis. To do so, some assumptions have been made.

The temperature dependence of the SRH-equation for p-type materials given in Equation 3.9 is related to the temperature dependence of the SRH density $n_1$. This parameter is dependent on the effective density of state in the conduction band given in Equation 2.5, whose temperature dependence is expressed as $N_{\mathrm{C}}(T) = N_{\mathrm{C}}^{300K}(T/300K)^{3/2}$ [14].

The temperature range in which the TDLS analysis is performed, 10-75 °C, indicates that impurity depletion can be assumed for the whole temperature range. This means that the majority carrier concentration for a p-type material $p_0$ equals the doping concentration $N_{\mathrm{a}}$ [14]. In addition, no temperature dependence has to be taken into account for the equilibrium concentration of the majority carrier in this simplified model [14].

Equation 3.12 - 3.16 assumes that $kn_1(T)/N_{\mathrm{a}} \gg 1$. The reason is that the term $n_1/p_0 = n_1/N_{\mathrm{a}}$ reflects the decreasing recombination activity of the defect as the fermi level $E_{\mathrm{F}}$ approaches mid-gap with increased temperature. The LLI-SRH lifetime will then see a steep increase in the temperature range where this term dominates [14]. When performing a TDLS analysis the temperature dependence of all parameters should be considered. For the purpose of simplification the temperature dependence of the capture time constants represented in Equation 3.14, is treated as a constant. This is in practice not valid [14, 37]. This means that using Equation 3.16 and assuming that the capture time constant, is constant will yield results deviating from the true defect energy level to the measured sample.

From Equation 2.30 it is observed that the bandgap decreases with increasing temperature. For the TDLS analysis, the band gap energy is kept constant. By not including the temperature dependence of the band gap in the TDLS analysis, the obtained defect energy levels can deviate from the actual defect energy level.

It is assumed that there is only one defect in the material [14]. From Section 2.2.3 and Section 2.2.4 it is explained that multiple defects and impurities can connect to the material in various steps of the production of the material. Impurities may connect to an unpassivated material through its dangling bonds at the surface. In the case of a passivated sample, different factors such as exposure to light and high temperatures may result in the degradation of the passivation layer where impurities can connect to the material. The various defect levels and impurities that can connect to the material are characterized by different energy levels [48, 49]. The energy state of the defect is also assumed stable. This is however not always accurate. For structural defects such as dislocations, point defects etc, this is true, however, this might not be accurate for precipitates or impurities connecting to the material whose defect energy can be continuously distributed in certain regions of the band gap [14].

The TDLS analysis performed on the brick samples 15B and 14B is presented in Figure 5.14a and Figure 5.14b, respectively. From Section 5.1 the carrier lifetime as a function of injection level measured in a temperature range of 10-75 °C,

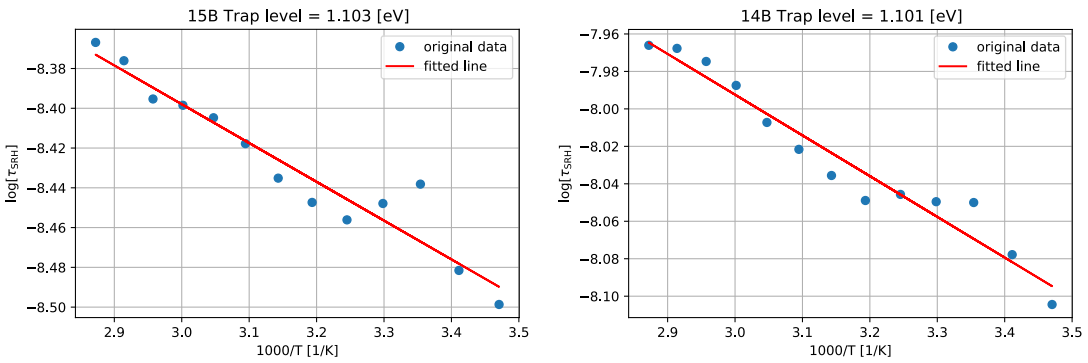


**(a)** **(b)**

**Figure 5.14:** The figures illustrate the TDLS analysis performed on the brick samples 15B (Figure 5.14a) and 14B (Figure 5.14b). The trap level found through the analysis is given in the title of both samples. For the sample 15B, the trap level corresponds to 1.103 eV and for the sample 14B, the trap level is found to be 1.101 eV.

shows a carrier lifetime increase with increasing temperature in accordance with the SRH equation in the LLI region. The data obtained from the carrier lifetime measurements is observed as a decrease in the Arrhenius slope shown in the figures below for 15B and 14B.

The TDLS analysis is conducted in accordance with Equation 3.16 together with the assumptions mentioned above. The defect levels obtained suggest that the lifetime-limiting defect lies in the upper half of the band gap [14]. Trap levels close to the CB are usually termed shallow defect and their influence on the carrier lifetime is not significant. The obtained defect levels suggest that the lifetime limiting defect lies in the upper half of the band gap [14]. The trap level obtained for both the 15B and 14B are very high which is a result of the assumptions made. These trap energy levels do not represent any of the defect levels as presented in [48, 49]. From Section 2.2.2 it is known that deep defect levels have a much more significant impact on the carrier lifetime. The reason can be attributed to the fact that the carriers trapped close to the CB are easily activated in comparison to the carriers trapped in deep defect levels [14]. As the energy level approaches the majority band gap edge (the VB for p-type materials), the minority carrier capture is increasingly suppressed under LLI due to the energy position of the defect level [14]. The trend observed with a decreasing slope, and a high lifetime limiting defect lying in the upper half of the band gap is also observed for other samples presented in Appendix 6.2.

The primary objective was to assess the suitability of the developed method for TDLS analysis, hence simplifications were made in the calculations. Nevertheless, to enhance the accuracy and validity of the analysis, future improvements should include the temperature dependence of the capture time constant i.e., capture cross-section, thermal velocity, and fewer assumptions. These are not included in the analysis as this is beyond the scope of the thesis.

CHAPTER

# SIX

# CONCLUSIONS

## 6.1 Concluding summary

This thesis has presented a method for performing temperature-dependent lifetime measurements on silicon wafers and bricks. The method is based on the minority carrier lifetime tester BCT-300 from Sinton Consulting. To perform temperature-dependent carrier lifetime measurements, the BCT-300 has been connected to a Peltier element. The method has been tested with a series of passivated and unpassivated samples spanning different crystal structures and thicknesses. The results show that the proposed method effectively measures temperature-dependent minority carrier lifetimes within the studied temperature range for lifetimes higher than 1.5 s. The investigations performed through this method are used to address the research questions given in Section 1.1.

The thesis also investigated the temporal stability of stack passivation of a-Si:H/a-SiN$_x$:H stack passivation. From Section 2.2.3 it is explained that the stack passivation of a-Si:H/a-SiN$_x$:H is expected to degrade about 15% from the initial value. However, the samples will regain 85-100% of their initial carrier lifetime after 1500 hours [21]. The FZ wafer displayed a continuous degradation which can be related to LID, destruction of the passivation layer or a nonuniform passivation layer. The 2T sample exhibits stabilization at 50% of the initially measured value, and it is expected that the lifetime will increase. However, due to time restrictions, this increase was not observed. The reason for the samples degrading more than 15% of their initial value can be attributed to light-induced degradation caused by exposure to light during the measurement process. Taking measurements in the full temperature range of one sample could take from 2 to 4 hours, meaning that the sample measured was exposed to multiple hours of light. Consequently, defects such as the boron-oxygen defect may have been activated, affecting the carrier lifetime measurements of the samples.

The unpassivated mc-Si wafers showed shorter carrier lifetimes compared to

the unpassivated n-type monocrystalline carrier lifetimes. This can be attributed to the presence of grain boundaries in the mc-Si sample which increases the number of dangling bonds at the surface, which increases the surface recombination and reduces the carrier lifetime. The monocrystalline p-type samples, namely IC-1T and IC-1B showed showed fluctuations and instability in the obtained data. The reason can be attributed to the BCT-300 instrument range which includes an error of 0.1 $\mu$s. Also, the instrument is not optimized for measuring wafers resulting in instability in the obtained data. This is observed as the extremely low minority carrier lifetimes, below 1.5 $\mu$s display fluctuations, and not a clear temperature dependence as expected from the SRH-equation in the LLI region. The mc-Si brick samples QSSPC-1 and QSSPC-2 showed a temperature dependence of the carrier lifetime that decreased with increasing temperature. Compared to the bricks from the block the mc-Si bricks displayed a much shorter carrier lifetime which is attributed to the grain boundaries and spatial variations in the sample.

The developed model poses various limitations for TDLS analysis. As multiple assumptions and simplifications were made to perform the TDLS analysis, the results obtained may not be as accurate as they would have been with a more advanced TDLS analysis. To improve the TDLS analysis the temperature-dependent capture cross section should be included as well as the temperature dependence of the capture time constant. Also, the experimental setup posed limitations and instability for the temperature range meaning that the obtained results from this analysis may not be accurate.

## 6.2 Future work

This work has presented a method for performing temperature-dependent lifetime measurements on silicon wafers and bricks. Further work will include improvements in accuracy for lifetimes lower than 1 $\mu$s and verifying the measurement with other well-established techniques. In addition, a validation method for the developed method is essential to ensure that the method accurately can measure the temperature-dependent carrier lifetime.

The BCT-300 shows instability and fluctuations at measured carrier lifetimes below 1 $\mu$s. For unpassivated wafers extremely low lifetimes may be measured and a more accurate method is essential. To measure the low lifetimes a development of the BCT-300 setup could be performed. The Peltier element proved to be unstable at temperatures below 20 °C, and 10-15 °C was only possible to reach once a day. More accurate and reliable results could be achieved by implementing a more stable heat controller.

The TDLS analysis performed included simplifications and assumptions which might have given results deviating from the actual case. For this reason, a more advanced TDLS analysis can be performed to characterize defect levels within the samples measured. The use of the TDLS method together with a single-temperature IDLS measurement to determine defect parameters will improve the accuracy [14].

# REFERENCES


[1] V. Masson-Delmotte et al. 'Global warming of 1.5 C'. In: *An IPCC Special Report on the impacts of global warming of 1.5 C* 1.5 (2018), pp. 43–50.

[2] *EIA projects nearly 50% increase in world energy usage by 2050, led by growth in Asia — eia.gov*. https://www.eia.gov/todayinenergy/detail.php?id=42342. [Accessed 07-May-2023]. 2020.

[3] Energy.gov. *Solar Photovoltaic Cell Basics*. URL: https://www.energy.gov/eere/solar/solar-photovoltaic-cell-basics. (accessed: 30.11.2022).

[4] EFTA. *AGREEMENT ON THE EUROPEAN ECONOMIC AREA*. https://www.efta.int/media/documents/legal-texts/eea/the-eea-agreement/Main%20Text%20of%20the%20Agreement/EEAagreement.pdf. Accessed: (17.04.2023). 1994.

[5] *bp Statistical Review of World Energy 2021*. https://www.bp.com/content/dam/bp/business-sites/en/global/corporate/pdfs/energy-economics/statistical-review/bp-stats-review-2022-full-report.pdf. Accessed: (24.05.2023). 2021.

[6] A. Goetzberger et al. *Crystalline silicon solar cells*. Vol. 1. Wiley Online Library, 1998.

[7] J. John et al. 'Introduction to surface passivation of industrial crystalline silicon solar cells'. eng. In: *Surface Passivation of Industrial Crystalline Silicon Solar Cells*. United Kingdom: Institution of Engineering and Technology, 2019. ISBN: 9781785612466.

[8] photovoltaic Equipment VDMA. *International Technology Roadmap for Photovoltaic (ITRPV): Publication of Thirteenth Edition*. https://www.vdma.org/documents/34570/16191053/2022-04-05+PR+VDMA+PV+ITRPV+2022+EN.pdf/132a2e1c-c932-9643-7bee-f218076e841f?t=1649064322356. Accessed: (25.04.2023). 2022.

[9] J. Nelson. *The physics of solar cells*. World Scientific Publishing Company, 2003.

[10] EFTA. *Best Research-Cell Efficiency Chart*. https://www.nrel.gov/pv/assets/pdfs/best-research-cell-efficiencies.pdf. Accessed: (17.04.2023). 1976.

[11] W. Shockley and H. Queisser. 'Detailed Balance Limit of Efficiency of p,Äên Junction Solar Cells'. In: *Journal of applied physics* 32.3 (1961), pp. 510–519. ISSN: 0021-8979.

[12] rscSiliconElement. *Silicon - Element information, properties and uses*. https://www.rsc.org/periodic-table/element/14/silicon. [Accessed 17.04.2023].

[13] O. Dupré et al. 'Thermal behavior of photovoltaic devices'. In: *Physics and engineering* 10 (2017), pp. 978–3.

[14] S. Rein. *Lifetime spectroscopy: a method of defect characterization in silicon for photovoltaic applications*. Vol. 85. Springer Science and Business Media, 2006.

[15] R. Sinton and A. Cuevas. 'Contactless determination of current–voltage characteristics and minority-carrier lifetimes in semiconductors from quasi-steady-state photoconductance data'. In: *Applied Physics Letters* 69.17 (1996), pp. 2510–2512.

[16] V. Kristiansson. 'Lifetime and resistivity measurements on silicon wafers and bricks'. In: (2023), p. 31.

[17] K. Mertens. *Photovoltaics: fundamentals, technology, and practice*. John Wiley and Sons, 2018.

[18] I. Fleming. *Molecular Orbitals and Organic Chemical Reactions*. Wiley, 2009. ISBN: 9780470746592. URL: https://books.google.no/books?id=pAgBngEACAAJ.

[19] T. S. Horanyi et al. 'In situ bulk lifetime measurement on silicon with a chemically passivated surface'. In: *Applied Surface Science* 63.1-4 (1993), pp. 306–311.

[20] W. Shockley and W. Read Jr. 'Statistics of the recombinations of holes and electrons'. In: *Physical review* 87.5 (1952), p. 835.

[21] X. Cheng et al. 'Temporal stability of a-Si:H and a-SiNx:H on crystalline silicon wafers'. In: *Energy Procedia* 124 (2017). 7th International Conference on Silicon Photovoltaics, SiliconPV 2017, 3-5 April 2017, Freiburg, Germany, pp. 275–281. ISSN: 1876-6102. DOI: https://doi.org/10.1016/j.egypro.2017.09.299. URL: https://www.sciencedirect.com/science/article/pii/S1876610217342704.

[22] H. Haug et al. 'Temperature dependent photoluminescence imaging calibrated by photoconductance measurements'. In: *Energy Procedia* 124 (2017). 7th International Conference on Silicon Photovoltaics, SiliconPV 2017, 3-5 April 2017, Freiburg, Germany, pp. 47–52. ISSN: 1876-6102. DOI: https://doi.org/10.1016/j.egypro.2017.09.338. URL: https://www.sciencedirect.com/science/article/pii/S1876610217343096.

[23] Unknown. - *Division of Research Safety | Illinois — drs.illinois.edu*. https://www.drs.illinois.edu/Page/SafetyLibrary/PiranhaSolutions. [Accessed 30-Apr-2023]. 2020.

[24] M. Tucci and L. Serenelli. 'Metastability of SiNx/a-Si:H crystalline silicon surface passivation for PV application'. In: *Thin Solid Films* 516.20 (2008). Proceedings on Advanced Materials and Concepts for Photovoltaics EMRS 2007 Conference, Strasbourg, France, pp. 6939–6942. ISSN: 0040-6090. DOI: https://doi.org/10.1016/j.tsf.2007.12.042. URL: https://www.sciencedirect.com/science/article/pii/S0040609007020871.

[25] S. Gatz et al. 'Thermal stability of amorphous silicon/silicon nitride stacks for passivating crystalline silicon solar cells'. In: *Applied Physics Letters* 93.17 (2008), p. 173502.

[26] S. De Wolf et al. 'Very fast light-induced degradation of a-Si: H/c-Si (100) interfaces'. In: *Physical Review B* 83.23 (2011), p. 233301.

[27] T. Niewelt et al. 'Understanding the light-induced degradation at elevated temperatures: Similarities between multicrystalline and floatzone p-type silicon'. In: *Progress in Photovoltaics: Research and Applications* 26.8 (), pp. 533–542. DOI: https://doi.org/10.1002/pip.2954. eprint: https://onlinelibrary.wiley.com/doi/pdf/10.1002/pip.2954. URL: https://onlinelibrary.wiley.com/doi/abs/10.1002/pip.2954.

[28] G. Coletti et al. 'Role of impurities in solar silicon'. In: *Advanced Silicon Materials for Photovoltaic Applications* (2012), pp. 79–125.

[29] P. Mathur et al. 'Temperature dependence of minority carrier lifetime in single-crystal and polycrystalline Si solar cells'. In: *Journal of Applied Physics* 52.5 (1981), pp. 3651–3654.

[30] S. Kristensen. 'Temperature coefficients and crystal defects in multi crystalline silicon solar cells'. PhD thesis. Thesis Dec, 2020.

[31] L. Hirst and N. Ekins-Daukes. 'Fundamental losses in solar cells'. In: *Progress in Photovoltaics: Research and Applications* 19.3 (2011), pp. 286–293.

[32] P. Altermatt et al. 'Assessment and parameterisation of Coulomb-enhanced Auger recombination coefficients in lowly injected crystalline silicon'. In: *Journal of Applied Physics* 82.10 (Nov. 1997), pp. 4938–4944. ISSN: 0021-8979. DOI: 10.1063/1.366360. eprint: https://pubs.aip.org/aip/jap/article-pdf/82/10/4938/10588108/4938_1_online.pdf. URL: https://doi.org/10.1063/1.366360.

[33] S. Sze. *Semiconductor devices: physics and technology*. John wiley and sons, 2008.

[34] H. Nagel et al. 'Generalized analysis of quasi-steady-state and quasi-transient measurements of carrier lifetimes in semiconductors'. In: *Journal of Applied Physics* 86.11 (1999), pp. 6218–6221.

[35] R. Sinton Insturments Sinton. *BCT-400/BLS-I Photoconductance Lifetime Tester User Manual*. English. Version V5.5. Sinton Instruments. 2016. 67 pp. Boulder, USA.

[36] R. Mattis and A. Baroody. *Carrier lifetime measurement by the photoconductive decay method*. Vol. 13. US Department of Commerce, National Bureau of Standards, 1972.

[37] J. Schmidt. 'Temperature- and injection-dependent lifetime spectroscopy for the characterization of defect centers in semiconductors'. In: *Applied Physics Letters* 82 (Mar. 2003), pp. 2178–2180. DOI: 10.1063/1.1563830.

[38] B. Paudyal et al. 'The Implementation of Temperature Control to an Inductive-Coil Photoconductance Instrument for the Range of 0-2308C'. In: *Progress in Photovoltaics: Research and Applications* 16 (2008), pp. 609–613. DOI: 10.1002/pip.839.

[39] A. Berg. 'Temperature and injection dependent photoluminescence imaging of charge carrier lifetime in multicrystalline silicon wafers'. MA thesis. 2019.

[40] M. Wiig et al. 'Identifying recombination parameters by injection-dependent lifetime spectroscopy on mc-silicon based on photoluminescence imaging'. In: vol. 1999. Aug. 2018, p. 130017. DOI: 10.1063/1.5049336.

[41] G. Mahan. 'Introduction to thermoelectrics'. In: *APL Materials* 4 (Oct. 2016), p. 104806. DOI: 10.1063/1.4954055.

[42] HAAKE. *nstruction Manual Circulator DC10 including all Baths*. English. Gebr. HAAKE GmbH. 1999. 56 pp. Germany.

[43] S. Søndergaard et al. 'Minority Carrier Lifetime Variations in Multicrystalline Silicon Wafers with Temperature and Ingot Position'. In: (2017), pp. 2651–2655. DOI: 10.1109/PVSC.2017.8366683.

[44] D. Sandiford. 'Temperature dependence of carrier lifetime in silicon'. In: *Proceedings of the Physical Society* 71.6 (1958), p. 1002.

[45] H. Haug et al. 'Lifetime spectroscopy with high spatial resolution based on temperature- and injection dependent photoluminescence imaging'. In: *Solar Energy Materials and Solar Cells* 200 (2019), p. 109994. ISSN: 0927-0248. DOI: https://doi.org/10.1016/j.solmat.2019.109994. URL: https://www.sciencedirect.com/science/article/pii/S092702481930323X.

[46] S. Nie et al. 'Photoluminescence-Based Spatially Resolved Temperature Coefficient Maps of Silicon Wafers and Solar Cells'. In: *IEEE Journal of Photovoltaics* 10.2 (2020), pp. 585–594. DOI: 10.1109/JPHOTOV.2019.2956261.

[47] S. Olibet et al. 'Effect of light induced degradation on passivating properties of a-Si:H layers deposited on crystalline Si'. In: (Jan. 2006).

[48] Rougieux Fiacre E. et al. 'Determining the charge states and capture mechanisms of defects in silicon through accurate recombination analyses: A review'. In: *Solar Energy Materials and Solar Cells* 187 (2018), pp. 263–272. ISSN: 0927-0248. DOI: https://doi.org/10.1016/j.solmat.2018.07.029. URL: https://www.sciencedirect.com/science/article/pii/S0927024818304008.

[49] A. Sanchez Garcia et al. 'The Recombination Parameter $\gamma$: Modeling and Comments'. In: *IEEE Journal of Photovoltaics* (2023), pp. 1–8. DOI: 10.1109/JPHOTOV.2023.3268399.

# APPENDICES

# A - TDLS ANALYSIS

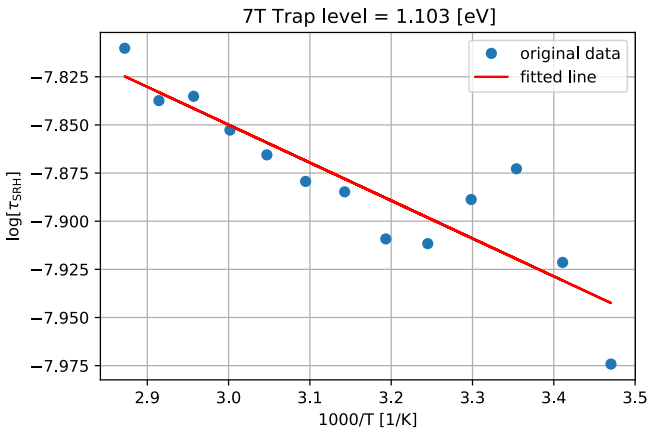


**Figure .1:** TDLS analysis on the brick sample 7T. The trap level found in the sample 7T corresponds to 1.103 eV.

The TDLS analysis is performed on 7 wafers, all exhibiting a carrier lifetime dependence in accordance with the SRH-equation given in Equation 3.9 in the LLI region.

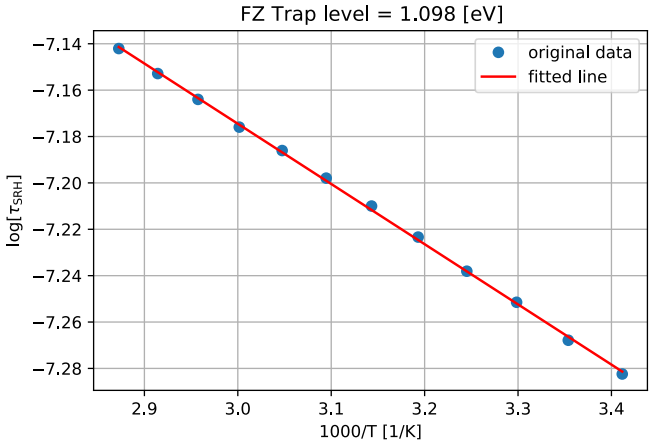


**Figure .2:** TDLS analysis on the wafer sample FZ. The trap level found in the FZ sample corresponds to 1.098 eV.

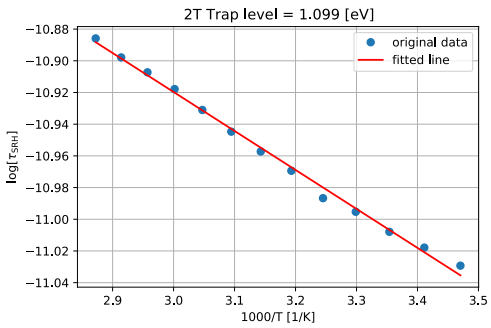


**Figure .3:** TDLS analysis on the wafer sample 2T. The trap level found in the 2T sample corresponds to 1.099 eV.

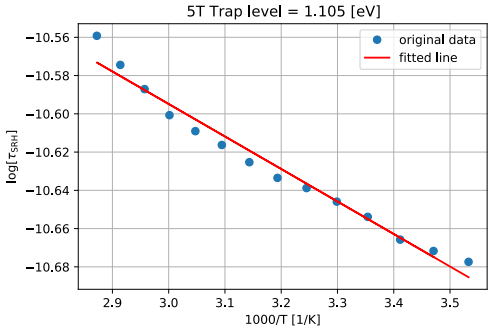


**Figure .4:** TDLS analysis on the wafer sample 5T. The trap level found in the 5T sample corresponds to 1.105 eV.

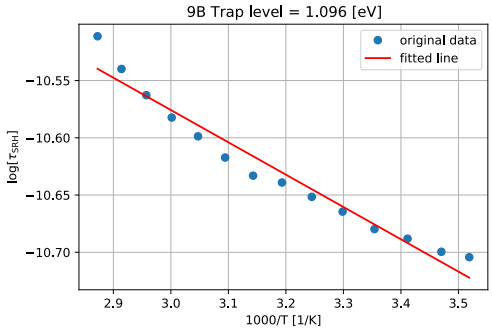


**Figure .5:** TDLS analysis on the wafer sample 9B. The trap level found in the 9B sample corresponds to 1.096 eV.

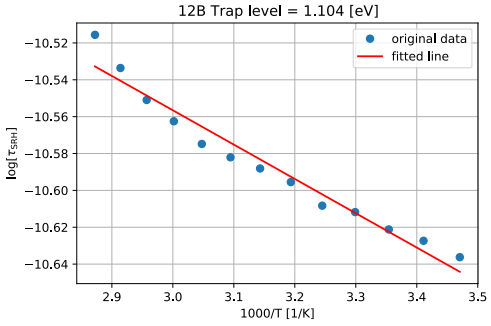


**Figure .6:** TDLS analysis on the wafer sample 12B. The trap level found in the 12B sample corresponds to 1.104 eV.

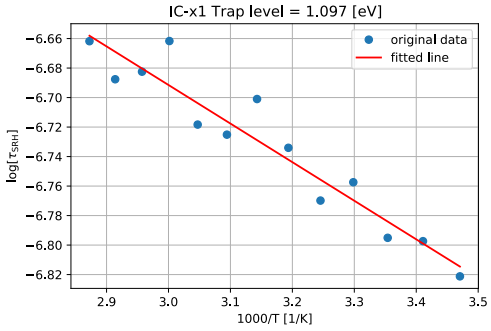


**Figure .7:** TDLS analysis on the wafer sample IC-x1. The trap level found in the IC-x1 sample corresponds to 1.097 eV.

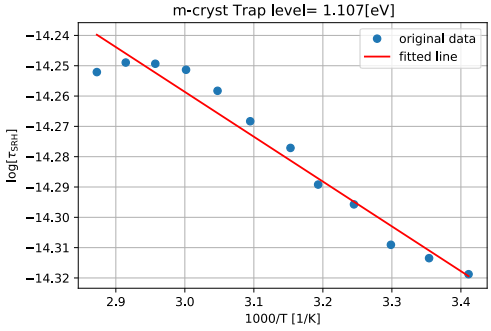


**Figure .8:** TDLS analysis on the wafer sample m-cryst. The trap level found in the m-cryst sample corresponds to 1.107 eV.

# B - METHOD DEVELOPMENT FOR TEMPERATURE DEPENDENT LIFETIME SPECTROSCOPY

# Method Development for Temperature Dependent Lifetime Spectroscopy

Vilma Kristiansson[1], Alfredo Sanchez Garcia[2], Marisa Di Sabatino[1]
[1] Department of Materials Science and Engineering, NTNU, Trondheim
[2] Sustainable Energy Technology, SINTEF Industry, Trondheim

## Introduction

- This work describes a novel method developed to perform temperature dependent lifetime measurements on silicon wafers and bricks. Additionally, this work investigates the stability of stack passivation of a-Si:H/a-$SiN_x$:H on 2 wafers in a period of 6 weeks.
- High efficiency in solar cells is associated with high minority carrier lifetime. The efficiency of solar cells is known to decrease with increasing the temperature [1].
- During the crystallisation process of silicon, impurities are introduced. The presence of impurities creates energy levels in the silicon band gap which will act as defect levels. This recombination mechanism is known as the Shockley-Read-Hall (SRH) recombination [2]. This recombination mechanism is usually dominant in silicon [1].
- Untreated wafers are usually dominated by surface recombination due to the unbonded atoms present at the edges. To reduce the surface recombination, wafers can be passivated. This saturates the unbonded atoms, and higher lifetimes can be expected [2].

## Theory

- To measure the minority carrier lifetime, the Sinton BCT-300 instrument is used. The instruments allows lifetime measurements in quasi-steady state photoconductance (QSSPC) and Transient photoconductance decay (PCD) modes [2].
- QSSPC measures the change in photoconductance. The software of the BCT-300 converts this to the excess carrier density (Δn). The measured flash intensity is converted into the generation rate, G. The lifetime ($\tau$) is then calculated

$$\tau = \frac{\Delta n}{G} \quad (1) \qquad \Delta n = \frac{\Delta \sigma}{q(\mu_n + \mu_p)} \quad (2)$$

- The PCD converts the sheet conductance to excess carrier density. The lifetime at each excess carrier density, Δn (equation 2), can be determined using equation 3. Equation 3 takes the derivative of the photoconductance decay with respect to time

$$\tau = \frac{\Delta n}{(d\Delta n/dt)} \quad (3)$$

## Experimental setup

- The Sinton Instruments BCT-300 (1) instrument is capable of measuring carrier lifetime (0.1 µs - 10 ms) in both the QSSPC and PCD modes. To enable lifetime measurements at various temperatures a Peltier element has been coupled to the BCT-300 setup. The Peltier element (2) consists of a temperature regulator (3) and a temperature stabilizer (4). To ensure electrical insulation between the copper plate and the sample, a 5 mm thick quartz plate has been mounted on top of the Peltier element (2).
- The Peltier element allows temperature measurements in the range [-10, 200] ˚C, where the range 10-75˚C is investigated here.
- The samples tested consists of 6 bricks: 4 mono-crystalline and 2 multi-crystalline, with thicknesses between 1 cm and 1.5 cm; and 10 wafers: 2 multi-crystalline with thicknesses > 300 µm and 8 monocrystalline with thicknesses < 300 µm.

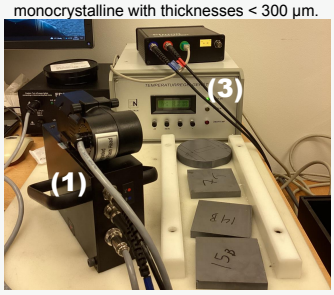


Sinton BCT-300 instrument and the temperature controller for the Peltier element.

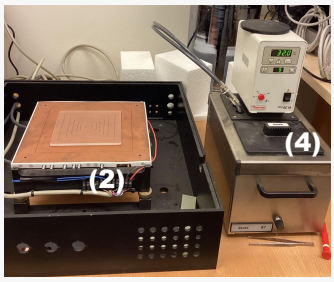


Peltier element and temperature controller. The instrument complemented by a quartz plate to ensure electrical insulation between the samples and the instrument.

## Results

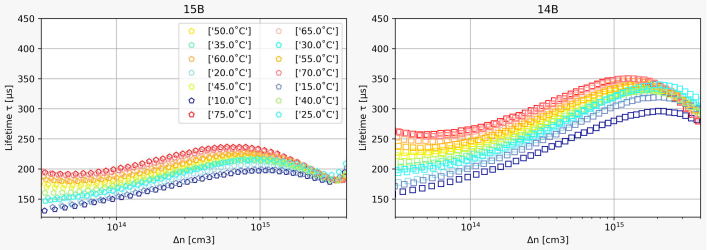


The samples 15B and 14B are boron-doped monocrystalline Czochralski grown bricks of 1 cm thickness. These exhibit a trend excepted: with increasing temperature, the lifetime also increases. This can be attributed to the temperature dependence of the dominating SRH recombination.

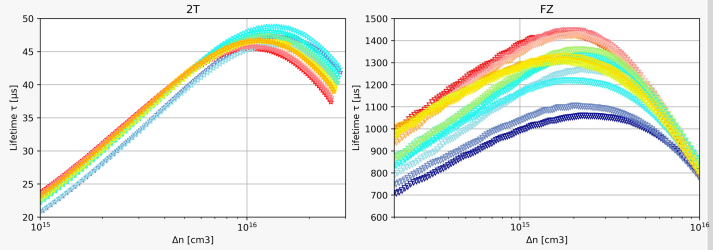


The sample 2T is boron-doped monocrystalline Czochralski grown wafer with a thickness of 0.05 cm. The sample FZ is a boron-doped monocrystalline float-zone grown wafer with a thickness of 0.026 cm. Both samples have been stack passivated with a-Si:H/a-$SiN_x$:H. The lifetime measurements for both wafers exhibit the typical trend observed for samples dominated by SRH-recombination mechanism.

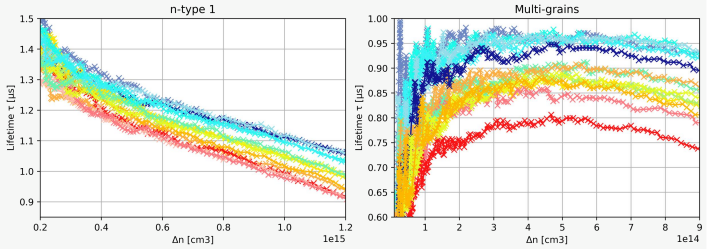


The sample n-type 1 is a phosphorus doped monocrystalline silicon wafer (with thickness 0.0165 cm) produced by the Czochralski method. The sample Multi-grains is a p-type boron-doped multi crystalline wafer (with thickness 0.0201 cm), produced by directional solidification. None of these two samples are passivated, which can be observed through the extremely low measured lifetimes. Because of this, the reference cell of the instrument saturates, resulting in instability and fluctuations in the measurements that hinder making any conclusions of the temperature dependence.

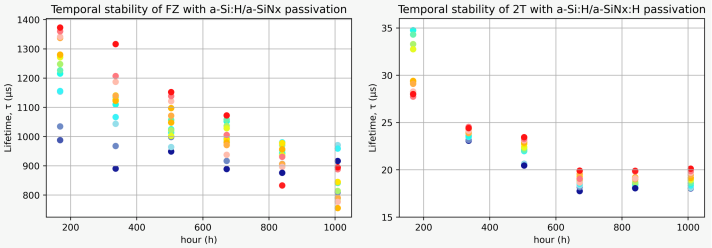


The two graphs display a decrease in lifetime with respect to time, for the FZ and 2T sample, respectively. This is excepted as observed in the scientific literature [4]. The degradation can be related to weak bonds of Si-H within the a-Si:H films as a result from light and temperature influence [4]. The 2T wafer depicts a stabilization after > 600 hours. From literature it is expected that this passivation will recover to 85-100% of initial value [4]. Due to difficulties measuring the exact same position of the wafer, the lifetime measured will vary from each measurement taken.

## Conclusion

This work has presented a method for performing temperature dependent lifetime measurements on silicon wafers and bricks. The method has been tested with a series of sample spanning different crystal structures, thicknesses and passivation. The results show that the proposed method effectively measures temperature-dependent minority carrier lifetimes within the studied temperature range for lifetimes higher than 1 µs. Further work will include trying to improve accuracy for lifetimes lower than 1 µs and verifying the measurement with other well-established techniques.

References:

[1] Nelson, J. A. (2003). *The physics of solar cells*. World Scientific Publishing Company.

[2] Rein, S. (2005). *Lifetime spectroscopy : a method of defect characterization in silicon for photovoltaic applications*. Tyskland: Springer.

[3] Sinton, R. A., Cuevas, A., & Stuckings, M. (1996, May). Quasi-steady-state photoconductance, a new method for solar cell material and device characterization. In *Conference Record of the Twenty Fifth IEEE Photovoltaic Specialists Conference-1996* (pp. 457-460). IEEE.

[4] Cheng, X., Marstein, E. S., You, C. C., Haug, H., & Di Sabatino, M. (2017). Temporal stability of a-Si: H and a-SiNx: H on crystalline silicon wafers. *Energy Procedia*, *124*, 275-281.

This work was performed within the Norwegian Research Center for Sustainable Solar Cell Technology (FME SUSOLTECH, project number 275639/E20). The center is co-sponsored by the Research Council of Norway and its research and industry partners.

SINTEF NTNU | Norwegian University of Science and Technology

# C - SPECIALIZATION PROJECT - TMT 4250: LIFETIME AND RESISTIVITY MEASUREMENTS ON SILICON WAFERS AND BRICKS

NTNU
Kunnskap for en bedre verden

Department of Material science

TMT4520 - Solar cell systems and materials,
specialization project

# Lifetime and resistivity measurements on silicon wafers and bricks

*Author:*
Vilma Helena Erika Kristiansson

*Supervisors:*
NTNU: Marisa di Sabatino, SINTEF: Alfredo Sanchez Garcia

31.01.2023

# Abstract

The efficiency of solar cells is influenced by multiple material properties. Two important properties are the carrier lifetime and the resistivity of the material. To better understand the methods used to determine these properties, this report has investigated lifetime and resistivity measurements in Czochralski boron-doped, p-type monocrystalline silicon.

This project has investigated carrier lifetime and resistivity measurements on p-type silicon samples with a variety of thicknesses and the effect of passivation. To measure the lifetime, Sinton instrument BCT-300 were used in two different modes. Firstly, the quasi-steady-state photoconductance decay (QSSPC) mode allows the measurement of carrier lifetime below 200 $\mu$s; followed by the photoconductive decay (PCD) mode, which allows the measurement of carrier lifetime above 100 $\mu$s. Lifetime measurements were performed on 13 wafers with different thicknesses ranging from 164-980 $\mu m$, and 3 brick samples with a thickness of 1cm. To ensure high-quality carrier lifetime measurements the BCT-300 instrument was calibrated both with bricks and wafers. The calibration samples had known resistivity and sheet resistance values. To ensure accurate lifetime measurements the wafers used for calibration were obtained from 4-point probe measurements.

The results show that the thickness of the samples greatly influences the measured carrier lifetime on the unpassivated samples. This can be explained through the surface of the unpassivated samples which consist of partially bonded atoms where unwanted vacancy atoms or extrinsic impurities from the environment can connect to the material. This results ion low measured lifetime for the unpassivated wafers due to the short distance the carriers have to undergo before reaching the surface. By increasing the sample thickness, the carrier lifetime increases due to a longer distance to the surface of the material. To increase the carrier lifetime, the wafers can be passivated. The effect was observed to increase the lifetime significantly. This can be explained by the the atoms on the surface edges of the passivated samples that are now fully bonded which means that the surface recombination lifetime is not prominent in the sample.

# Sammendrag

Effektiviteten til solceller blir påvirket av flere ulike material egenskaper. To viktige egenskaper er resistivitet og levetid til wafere. For å få en dypere og bredere forståelse av metodene som brukes for å bestemme disse egenskapene, har denne rapporten undersøkt levetid og resistivitetsmålinger på Czochralski bor-dopet, p-type monokrystallinsk silisium.

Detter ble undersøkt ved p måle levetid og resistivitet på silisiumprøver med ulik tykkelse. I tillegg ble effekten av passivering undersøkt for wafere. For å måle levetiden ble Sinton instrumentet BCT-300 benyttet i to ulike moduser. Først ble ≪quasi-steady-state photoconductance decay≫ (QSSPC) benyttet, som tar kan måle levetid i prøver under 200 $\mu$s. Deretter ble modusen "photoconductive decay" (PCD) benyttet som gjør det mulig å ta levetidsmålinger over 100 $\mu$s. Levetidsmålingene ble gjennomført på 13 ulike wafere med ulik tykkelse mellom 164-980 $\mu$m, og 3 tykkere prøver på 1cm. For å sikre nøyaktige målinger med BCT-300 instrumentet ble det kalibrert ved å bruke 6 wafere med kjent resistivitet og tykkelse, og tykkere prøver (1cm) med kjent resistivitet. For å sikre at kalibreringen skulle være av høy kvalitet ble waferenes resistivitet målt ved å benytte en 4-punkts probe metode.

Resultatene viste at tykkelsen på prøvene har stor innflytelse på den målte levetiden for de upassiverte prøvene. Dette kan bli forklart ved at overflaten til de upassiverte prøvene består av ikke-fullstendige atombindinger, noe som betyr at uønskede vakans atomer o.l. kan feste seg til materialet. Dette gjør at ladningsbærerne får en kortere distanse for å komme til overflaten og rekombinere. Ved å øke tykkelsen på prøven, økes også distansen ladningsbæreren må gjennom for å komme til overflate, som øker levetiden. For å øke levetiden til waferene kan de passiveres. Fra resultatene ble det funnet at levetiden i de tynne prøvene merkbart økte. Dette kan forklares ved at atomene på overflaten av prøven er fullstendig mettet, slik at ladningsbærerne ikke kommer til overflaten. Dette gjør at overflaterekombinasjonen ikke lenger er til stede og levetiden øker.

# Acknowledgements

This specialisation project has been written for the department of material science as part of the course TMT4520 - *Solar cell systems and materials, specialization project*.

I want to express my sincere gratitude to my co-supervisor Alfredo Sanchez Garcia for being patient with me through this project while teaching me the instruments, sharing knowledge, and answering numerous emails. Also, I want to thank Alfredo for quick replies and feedback of this report and support through this project. I also want to give my warmest thanks to my supervisor Marisa di Sabatino for giving feedback on the report and being patient with me through this process.

I also want to thank Irene Brakstad for polishing the samples and Pål Tetlie for sawing wafers with different thicknesses. Lastly, I want to thank Rune Søndenå at IFE for the great cooperation and help with the passivation of the samples.

# Table of Contents

# 1 Introduction

The world is facing a pressing need for sustainable energy due to the current challenging energy crisis and global warming [1]. The transition from fossil fuel-based energies to renewable energies requires reducing the costs of renewable energy sources and simultaneously increasing their efficiencies. One of the energy sources showing great potential is the Sun. The challenges seen by solar energy today are mainly related to cost, maintenance, energy storage, and weather dependencies. Solar cell material-related challenges are mainly related to efficiency as this property is a compromise between cost and material used [2]. Silicon is the most important solar cell material and makes up approximately 95% of all solar cell material used for fabrication [3].

## 1.1 Background and motivation

The efficiency of solar cells are influenced by multiple material properties. Two important properties are the carrier lifetime and the resistivity of the material. To gain a better understanding of the methods used to determine these properties, this report will investigate lifetime and resistivity measurements in Czochralski boron doped, p-type monocrystalline silicon.

During the solidification of Czochralski silicon (Cz-Si), a large number of impurities assemble in the ingot. This has a negative effect on the minority carrier lifetime. To measure the lifetime different techniques can be used. In the paper written by Sinton et al. [4], the quasi-steady-state photoconductance decay (QSSPC) regime is described. This regime determines the minority carrier lifetime by using a photoconductance instrument in quasi-steady-state mode. According to the paper, the QSSPC method allows for the utilization of less complex electronics and illumination sources in comparison to the transient photoconductive decay method, while still being capable of measuring lifetimes within the range of nanoseconds to milliseconds [4]. Another method used to measure the carrier lifetime is the photoconductive transient decay (PCD) technique. This technique allows the measurement of high carrier lifetimes through a sharp pulse of illumination that is rapidly switched off and then the excess carrier density without illumination can be determined [5].

In monocrystalline silicon samples, defects are most likely to occur at the surface of the material. The surface edges are abrupt discontinuities in the crystal structure consisting of partially bonded atoms (dangling bonds) [6]. This introduces vacant positions in the lattice where unwanted vacancy atoms or extrinsic impurities from the environment can connect to the material. These impurities introduce energy levels in the band gap of the material. The recombination mechanism associated with this phenomenon is known as Shockley-Read-Hall(SRH) recombination [7], [8]. SRH is the most important recombination mechanism in silicon [2]. Recombination occurring at the surface due to defects and impurities can be explained as a two-dimensional case of SRH recombination. According to the study by Nagel et al., [9], one of the mechanisms contributing negatively to the efficiency is the recombination losses in the surface and bulk, hence it is important to investigate the recombination lifetime. One method used to reduce surface recombination is passivation [6].

Lifetime is an indication of the material quality, and it is desired that this property is high to have an efficient solar cell. The lifetime is a measure of the time it takes for an electron to recombine [2]. The lifetime is negatively affected by recombination, and one method to reduce surface recombination is through passivation. A result expected after passivation is higher lifetimes achieved on the samples compared to before passivation.

Another parameter also investigated is the effect the sample thickness has on the lifetime. S. Rein through his work *Lifetime spectroscopy: a method of defect characterization in silicon for photovoltaic applications*, [6], explains that by increasing the wafer thickness the surface recombination impact on the effective carrier lifetime will decrease. By measuring the lifetime on different thicknesses one can obtain information about how the surface recombination velocity changes depending on sample thickness.

## 1.2 Aim and scope of the work

This specialization project work is conducted together with SINTEF in Trondheim and aims to investigate carrier lifetime and resistivity measurements on silicon bricks and wafers and a block before and after passivation on the samples that could be passivated. The project is limited to measurements on cz p-type, boron-doped monocrystalline silicon at room temperature. The lifetime measurements are performed using Sinton Instruments BCT-300, which according to Sinton Consulting is able to measure accurate lifetimes both on unpassivated and passivated samples [5]. The resistivity will be measured using a Jandel 4-point probe instrument to ensure high-quality calibration for the BCT-300. The BCT-300 instrument will be used to measure the carrier lifetime of a block, followed by three bricks and five wafers cut from the block. Additionally, measurements will be conducted on nine thin wafers that are not from the block. Four wafers from the block and six thin wafers will be passivated at IFE (Insitutt for Energiteknikk), and the effect of passivation on the measurements will be investigated.

The project work is structured as follows: section 2 introduces the relevant theory mainly based on the work *Lifetime Spectroscopy: A Method of Defect Characterization in Silicon for Photovoltaic Applications* by S. Rein ([6]) and *The physics of solar cells* by J. Nelson ([2]). Following the theory chapter, Section 3 explains the theory behind the measurement techniques used in the experimental work given in section 4. Section 5 explains and illustrates results through tables and graphs and discusses the results in relation to the theory. Lastly, in section 6 a conclusion of the most important findings will be presented, followed by suggestions for further work.

# 2 Theory

This chapter aims to provide an overview of the fundamental properties and characteristics of silicon as a semiconductor, including its position in the field of solar energy. Silicon is the most used material for solar cells due to its abundance on earth (27.7% [10]), and the combination of high efficiency, low cost, and long lifetime [11]. This chapter begins by introducing semiconductor properties followed by an explanation of recombination mechanisms in silicon. Lastly, resistivity and related electrical parameters will be presented.

## 2.1 Semiconductor Properties

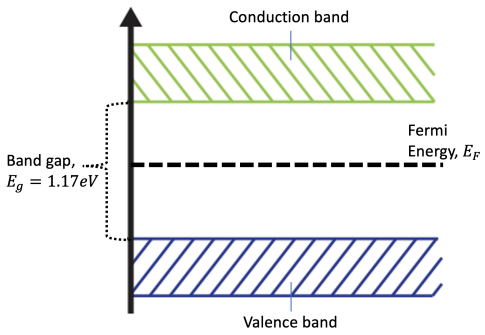


**Figure 1:** Silicon bandgap, shown with the Fermi energy level in the middle of the conduction and the valence band (the forbidden band gap) [2].

Semiconductors have a number of properties that make them suitable for use in solar cells. These include their ability to absorb visible light, their band gap between initial, occupied states and unoccupied states that are involved in photon absorption, and their ability to be tailored for efficient transport of charges. The minimum amount of energy needed to promote an electron from the valence band to the conduction band is called the fundamental band gap, $E_g$ [2], shown

through $E_g = E_C - E_V$, where $E_C$ and $E_V$ denote the conduction band minimum and valence band maximum shown in Figure 1. The *conduction band* (CB) is described as the lowest unoccupied band, and the *valence band* is described as the highest occupied band containing valence electrons. Photon energy equal to or larger than the band gap allows the absorption of photons and converts the resulting excess energy into electrical energy, which can then be used to power devices. When an electron is excited across a band gap, it quickly decays to reach the lowest available energy state in the conduction band (minimum).

Semiconductors that contain no impurities, nor defects are commonly referred to as intrinsic semiconductors or pure and perfect semiconductors. Extrinsic semiconductors are intrinsic semiconductors where an element have intentionally been added to the material [2]. This is commonly referred to as doping. Elements with more valence electrons (n-type doping) or fewer valence electrons (p-type doping) can be added. This changes the conductivity of the material. The conductivity increases with increasing temperature, and with decreasing band gap [2].

In thermal equilibrium, at T=0k, the VB states are occupied and CB states are empty, as all electrons are involved in bonding. The electrons in the VB are not easily removed and require energy equal to the band gap to be removed to the nearest available unoccupied level. Hence they do not conduct heat or electricity easily [2]. With increasing temperature, the electrons gain increasingly more kinetic energy and electrons are thermally excited from the VB to the CB. The higher the temperature the greater the number of electrons and holes which are mobilized, and the higher the conductivity. The occupation probability of the allowed electron states at a given energy level E in thermal equilibrium can be described by the Fermi-Dirac distribution function presented in Equation 1 [6]. It is important to note that each energy state can be occupied of maximum two electrons of opposite spin according to the Pauli Exclusion principle [6].

$$f(E) = \left[1 + \exp(\frac{E - E_F}{k_B T})\right]^{-1} \tag{1}$$

where $E_F$ [eV] is the Fermi energy, $k_B$ [eV/K] is the Boltzmann's constant and $T$ [K] is the absolute temperature. To calculate the electron and hole densities in the CB and the VB, respectively, at thermal equilibrium the following equations can be used for the electron (Equation 2) and holes (Equation 3) respectively

$$n_0 = N_{C\,\exp}\left(\frac{E_F - E_C}{k_B T}\right) \tag{2}$$

$$p_0 = N_{V\,\exp}\left(\frac{E_V - E_F}{k_B T}\right) \tag{3}$$

Equation 2 and Equation 3 shows that $n_0$ [$cm^{-3}$] and $p_0$ [$cm^{-3}$] strongly depends on both the Fermi level and the temperature [2]. $N_C$ [$cm^{-3}$] and $N_V$ [$cm^{-3}$] are the effective density of state in the CB and VB, respectively. These values can be calculated through the following equation

$$N_{C/V} = 2\left(\frac{m^*_{e/h} k_B T}{2\pi\hbar^2}\right)^{\frac{3}{2}}, [2] \tag{4}$$

where $m^*_{e/h}$ [-] are the effective masses of electrons and holes respectively, and $\hbar$ [Js] is the reduced Planck constant. Equations 1-4 shows that the product of the $n_0$ and $p_0$ are constant for any given material at a given temperature and independent of $E_F$.

The carrier density is an important parameter as impurities or structural defects in the material introduce bonds of different strengths in the crystal. This changes the local distribution of electronic energy levels. If these impurity energy levels occur within the band gap, they can affect the electronic properties of the semiconductor. Introducing occupied levels increases the Fermi level, which increases the density of electrons relative to holes in equilibrium. In the same way, unoccupied levels reduce the Fermi level and increase the density of holes relative to electrons. The density and the nature of the carriers in the semiconductor can therefore be controlled by adding definite amounts of impurities with energy levels close to the conduction or valence band edge. This addition of impurities is commonly referred to as doping [2].

## 2.2 Carrier density

Semiconductors can be tailored by adding either donors which are electrons (n) with negative charges or acceptors which are holes (p) with positive charges, commonly referred to as doping. The donors or acceptors added will be then incorporated in substitutional sites in the crystal lattice. By adding donors or acceptors the conductivity and electrical properties in the material will change [2].

The semiconductor can be doped in order to increase the density of electrons relative to holes, this is called n-type doping. This is done by adding elements from group 5 such as phosphorus in the semiconductor, which can be observed in Figure 2 as the allowed level is introduced into the forbidden gap close to the conduction band. Hence little energy is required to excite electrons to the conduction band [2]. The additive atom is referred to as the donor atom as it donates one free electron to the lattice. In n-type materials, electrons are the majority carriers and the holes are minority carriers, n≫p. The concentration of free electrons in n-doped semiconductors can be assumed to be approximately equal to the density of the donor atoms ($N_D$): $n \approx N_D$ [2].

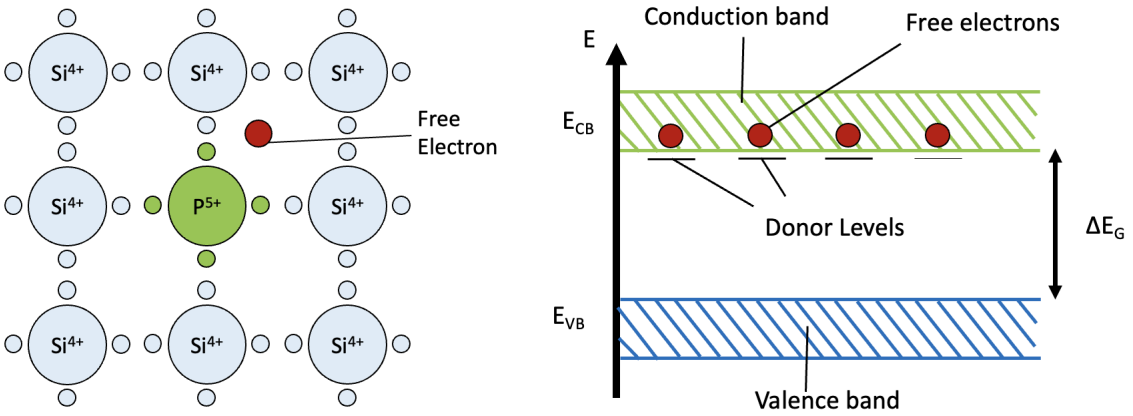


**Figure 2:** n-type doping of semiconductors. The fifth electron from phosphorous is available as a free electron. This introduces a new energy level in the band diagram close to the conduction band minimum [2].

Another way the semiconductor properties can be altered is through the introduction of atoms with a lower valence. The purpose is to increase the density of holes compared to electrons. The hole functions as an acceptor atom as it accepts an electron from the crystal. This process is referred to as p-type doping [2]. This is usually performed with atoms from group III in the periodic table such as boron. The allowed level introduced in the forbidden gap is now close to the valence band (seen in Figure 3), meaning that less energy is emitted during relaxation from the conduction to valence band [2].

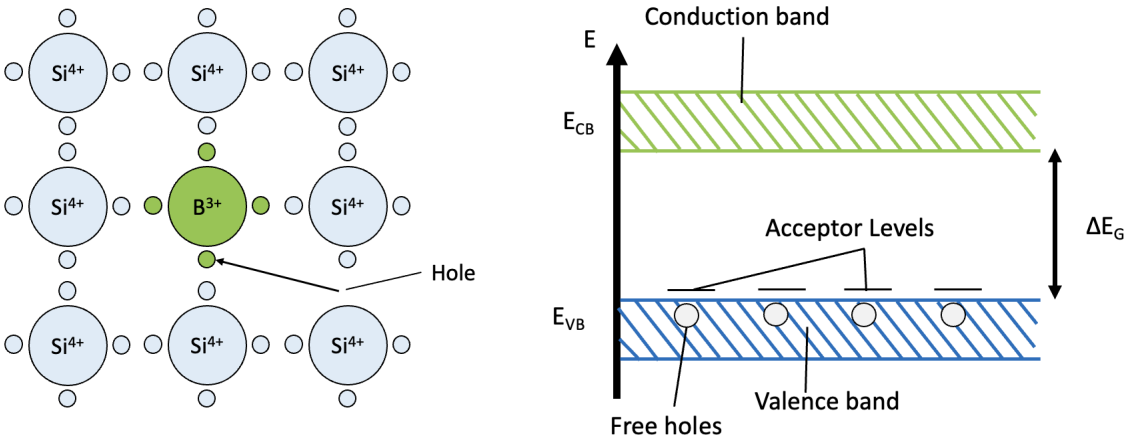


**Figure 3:** p-type doping of semiconductors. As boron is missing an electron, a neighbouring electron moves into the bond generating a hole. This introduces a new energy level in the forbidden band gap close to the valence band maximum [2].

When the material is doped the density of the dopant can be assumed to be approximately equal to the electron and hole densities in an intrinsic semiconductor shown in Equation 2 and Equation 3, respectively. This is however only valid when the density of the donors is lower than the effective density of state of electrons in the case of n-type doping, and in the case of p-type doping when the density of the acceptor is lower than the effective density of states of holes [6]. The Fermi level and the equilibrium concentrations of hole and electron density in doped (extrinsic) semiconductors depend on the type and concentration of dopant used.

The majority carrier concentration can be calculated on the basis of the doping concentration through Equation 6 and Equation 5 for electrons and holes respectively [6].

$$\mathrm{p_0 = N_A} \quad \text{and} \quad \mathrm{n_0 = \frac{n_i^2}{N_A} \ll p_0}, \qquad \text{for a p-type semionductor} \tag{5}$$

$$\mathrm{n_0 = N_D} \quad \text{and} \quad \mathrm{p_0 = \frac{n_i^2}{N_D} \ll n_0}, \qquad \text{for a n-type semionductor} \tag{6}$$

where $N_\mathrm{A}$ and $N_\mathrm{D}$ are the concentration of the acceptor and donor atoms respectively given in the units of [$\mathrm{cm^{-3}}$]. The position of the Fermi level in a doped semiconductor is directly determined by the doping concentration which can be observed in Figure 4.

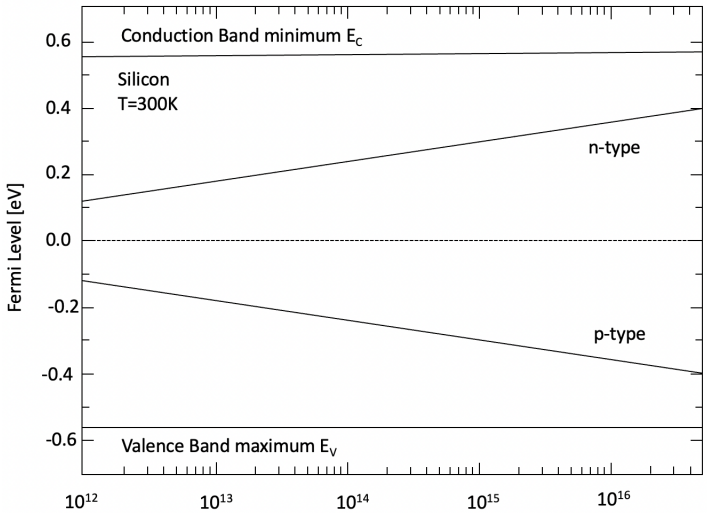


**Figure 4:** The Fermi level $E_\mathrm{F}$ as a function of doping concentration in n- and p-type silicon at 300 K, with respect to the intrinsic energy $E_\mathrm{i}$.

## 2.3 *pn*-Junction

For a semiconductor material to efficiently transport charges, a $p$-type and an $n$-type semiconductor is joined together creating the pn-junction. When the $n$- and $p$-side are connected the $n$-side has a surplus of free electrons that diffuse due to the concentration gradient as a diffusion current to the $p$-side where the electrons recombine. The opposite happens for the holes. They diffuse from the $p$-side to the $n$-side where they recombine with the electrons. This creates an electrical field in the junction, that drives electrons to the $n$-side and holes to the $p$-side. This is the foundation for the space charge region that exists at the $pn$-junction, which causes a potential difference between the border of the space charge region, referred to as the diffusion voltage. The concentration of minority carriers at the edge of the depletion region increases exponentially with applied voltage. The process by which this concentration is controlled by the bias across the junction is known as the minority carrier injection [2].

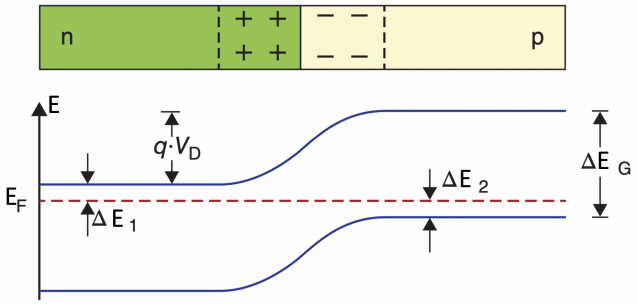


**Figure 5:** $pn$-junction together with band diagram, fixed positive charges on the $n$-side (left) and fixed negative charges on the $p$-side (right). $E_F$ is the fermi level, close to the CB on the $n$-side and close to the VB on the $p$-side. $q{\cdot}V_D$ is the built in voltage. $E_G$ is the distance between the VB and the CB [12].

## 2.4 Generation and recombination

When the semiconductor is subjected to light the electron is excited from the valence to the conduction band and an electron-hole pair is created. Thus this process is called generation. The energy needed to excite an electron from the valence band to the conduction band can come from thermal processes or through the absorption of photons [2].

The inverse process of generation is recombination. This process refers to an event where electron-hole pairs are annihilated due to a spontaneous transition of an excited electron from the conduction band to an unoccupied state, hole, in the valence band. The energy is released either as photons, phonons, or transferred to other carriers, which ensures energy and momentum conservation for the individual processes of electron-hole recombination [2].

The recombination rate ($R$, [$\mathrm{cm^{-3}s^{-1}}$]) is directly proportional to the densities of the carriers involved in the transition from VB to CB and to a recombination coefficient. The recombination coefficient depends on the quantum mechanical probability of an electron transition from the CB to the VB and thus depends on the individual physical processes underlying recombination [6]. Under thermal equilibrium, the thermal generation rate $G_0$ [$\mathrm{cm^{-3}s^{-1}}$] and the equilibrium recombination rate $R_0$ [$\mathrm{cm^{-3}s^{-1}}$] are balanced, meaning that the product of the equilibrium hole and electron densities $p_0$ and $n_0$ is the intrinsic carrier concentration $n_i^2$ [$\mathrm{cm^{-3}}$] [6].

If the material is constantly subjected to light under a constant optical excitation, a new stationary state is present. In the stationary state, the generation rate $G > G_0$ and the total recombination rate $R > R_0$ are balanced. In the case when the light is switched off the system wants to regain its equilibrium state, this however is not reached instantaneously. For this reason the excess electron and hole densities $\Delta n = n - n_0$ [$\mathrm{cm^{-3}}$] and $\Delta p = p - p_0$ [$\mathrm{cm^{-3}}$], respectively, decay at a net recombination rate. This net recombination rate is given as $\Delta U = R - R_0$ [$\mathrm{cm^{-3}s^{-1}}$] [6]. Assuming charge neutrality and absence of trapping centres, it follows that $\Delta n = \Delta p$. From this one can derive an expression for the recombination time, taking into account the time-dependent

decay of excess carrier density $\Delta n(t)$ [6].

$$\frac{\mathrm{d}\Delta n(t)}{\mathrm{d}t} = -U\left(\Delta n(t), n_0, p_0\right) \tag{7}$$

Under thermal equilibrium the net recombination rate U [$\mathrm{cm^{-3}s^{-1}}$] can be written as a polynomial in $\Delta n$ [$\mathrm{cm^{-3}}$], whereby the zero-order coefficient identically equals zero, as $U(\Delta n = 0)$ has to vanish. Hence Equation 7 suggests that the time-dependent decay of the excess carrier density $\Delta n$ follows an exponential decay. This exponential decay presents the recombination lifetime $\tau$ [s], often referred to as lifetime or carrier lifetime, expressed in Equation 8 [6].

$$\tau(\Delta n, n_0, p_0) = \frac{\Delta n}{U(\Delta n, n_0, p_0)} \tag{8}$$

The recombination mechanisms are distinguished by intrinsic or extrinsic mechanisms. The intrinsic recombination mechanisms are unavoidable as they are present in all types of crystals. If the excess energy is released as a photon the process is referred to as band-to-band recombination and denoted $\tau_{\mathrm{Rad}}$ [s]. If the excess energy is transferred to a third carrier it is an Auger band-to-band recombination mechanism $\tau_{\mathrm{Auger}}$ [s]. The extrinsic recombination mechanisms normally take place as a step-wise transition via a defect centre with an intermediate energy level in the band gap. This process is more commonly referred to as Shockley − Read − Hall and this lifetime is denoted $\tau_{\mathrm{SRH}}$ [s]. These three recombination mechanisms are often used to express the bulk lifetime $\tau_{\mathrm{bulk}}$ [s] of a wafer shown in Equation 9 [2].

$$\frac{1}{\tau_{\mathrm{bulk}}} = \frac{1}{\tau_{\mathrm{Auger}}} + \frac{1}{\tau_{\mathrm{Rad}}} + \frac{1}{\tau_{\mathrm{SRH}}} \tag{9}$$

The effective carrier lifetime, $\tau_{\mathrm{eff}}$ [s], of a silicon wafer combines the bulk and surface recombination by

$$\frac{1}{\tau_{\mathrm{eff}}} = \frac{1}{\tau_{\mathrm{bulk}}} + \frac{2S_{\mathrm{eff}}}{W} \tag{10}$$

where $\tau_{\mathrm{bulk}}$ is the bulk lifetime, $W$ is the wafer thickness [cm] and $\mathrm{S_{eff}}$ [cm/s] is the effective surface recombination. Equation 10 shows that with a low bulk recombination lifetime, surface recombination will be dominant and vice versa [6].

### 2.4.1 Radiative recombination

In direct semiconductors, radiative recombination is considered the dominant recombination process. Radiative band-to-band recombination is the direct annihilation of an electron-hole pair, involving the emission of a photon with energy equal to that of the band gap, illustrated in Figure 6. The radiative recombination rate depends both on the concentrations of free electrons n and free holes p, which can be seen in Equation 11 for the net recombination rate $U_{\mathrm{rad}}$ [$\mathrm{cm^{-3}s^{-1}}$] [6]:

$$U_{\mathrm{rad}} = B(np - n_{\mathrm{i}}^2) \tag{11}$$

where B [$\mathrm{cm^{-3}s^{-1}}$] reflects the probability of a radiative transition and is a material property and strongly depends on the band structure of the semiconductor. For indirect band gap materials, both a photon and a phonon are emitted in order to conserve both momentum and energy [6]. Thus this recombination mechanism is not dominant in indirect band gap materials such as silicon.

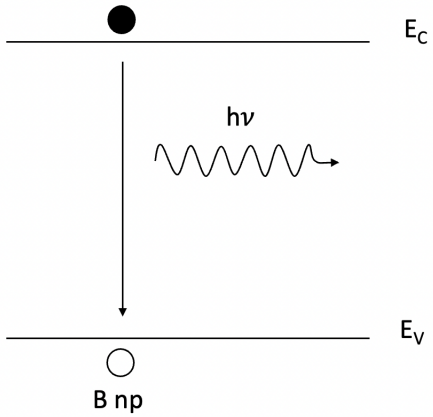


**Figure 6:** Schematic diagram of intrinsic recombination mechanism, radiative band recombination [6].

### 2.4.2 Auger recombination

The Auger recombination mechanism is most important when carrier densities are high and in indirect band gap materials. This includes materials which are doped, have a low band gap or are at high temperatures [2]. Auger recombination is an intrinsic recombination process commonly seen as a three-particle interaction. The energy released during the recombination of an electron-hole pair is transferred to a third charge carrier, which releases its excess energy as a phonon to the crystal. This is also referred to as thermalization [6]. Auger recombination can also take the form of a band-to-band process, meaning that an electron and two holes or two electrons and one hole are involved. The rate of this mechanism depends on the densities of all carriers involved, and the net rate for two-electron and one hole (eeh-process) and two holes and an electron (ehh-process). The net recombination rate of these processes $U_{\text{Auger}}$ [$\text{cm}^{-3}\text{s}^{-1}$] are given in Equation 12 [2].

$$U_{\text{Auger}} = C_{\text{n}}(n^2p - n_0^2p_0) + C_{\text{p}}(np^2 - n_0p_0^2) \tag{12}$$

where $C_{\text{n}}$ and $C_{\text{p}}$ [$\text{cm}^6\text{s}^{-1}$] are Auger coefficients of the eeh- and ehh-processes, respectively.

During an Auger recombination event, momentum and energy are conserved and can occur in indirect band gap materials, unlike radiative recombination which is suppressed. Auger recombination is also the dominant loss mechanism in very pure silicon and germanium [2].

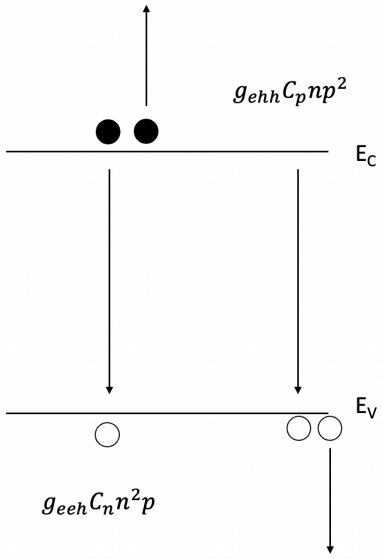


**Figure 7:** Schematic diagram of intrinsic recombination mechanism, Auger band-band recombination [6].

### 2.4.3 Shockley-Read-Hall

In the case of an extrinsic recombination mechanism, the decay of an electron-hole pair does not happen band-band as it does in an intrinsic mechanism. The recombination is a step-wise transition of an electron transition via a defect centre with an intermediate energy level in the band gap. This recombination mechanism is commonly known as Shockley – Read – Hall (SRH) recombination after Shockley, Read, and, Hall who originally modelled this effect [7].

SRH is the most important recombination process in silicon semiconductors due to impurities in the ideal crystal structure. These impurities introduce energy levels in the forbidden band gap that induces defect levels that act as recombination centres if located within the band gap. This mechanism can occur either through defects in the bulk, induced by impurities or lattice defects, or as a result of surface states [6]. Traps are normally localised states that mainly capture and release one type of carrier. Those that capture and release both carriers are called recombination centres [2].

The energy levels representing impurities or crystallographic imperfections may be occupied by an electron or by a hole. These states make it possible for electrons or holes to interact with the conduction (CB) and valence band (VB), respectively, through four elementary processes shown in Figure 8 [6].

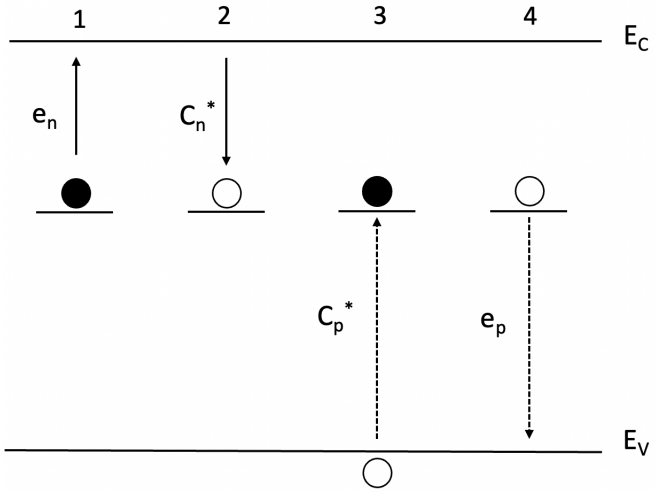


**Figure 8:** Electron band diagram showing the four interaction mechanisms of free carriers with a defect level in the band gap: electron emission (1), electron capture (2), hole capture (3), and hole emission (4). The direction of the solid and dashed arrows indicates the direction of the electron and hole transition, respectively [6].

An occupied defect level shown as 1 and 3 in Figure 8 where an electron is excited to the CB (1) or captures a hole from the VB (3). An unoccupied defect level shown in 2 and 4 on the other hand can either capture an electron from the CB (2) or emit its hole into the VB (4) [6]. It is important to understand the function of these defects in relation to the conduction band (CB) and valence band (VB). The possible two-step processes that result from the interaction of defects (form a combination of 1,2,3, and, 4 shown in Figure 8) with the CB and VB can be can be understood as three different processes based on the function assigned to the defect level. These three processes are when the defect level acts as a recombination centre, a generation centre, or a trap centre, which will be further explained in the following [6].

The first process takes place when the defect level acts as a recombination centre. This can be seen as a two-step capture process where a free electron from the CB (2) and a free hole from the VB (3) are captured by the defect level and annihilate each other. Alternatively, it can be understood as a two-step relaxation event, where a free electron from the conduction band first relaxes to the defect level (2) and then relaxes to the VB (3), where it finally annihilates a hole [6].

When the defect level acts as a generation centre a two-step emission event occurs where the defect level successively emits an electron into the CB (1) and a hole into the VB (4). Alternatively, it can also be understood as a two-step excitation process where an electron from the VB is first excited into the defect level (4) and then excited into the CB (4), resulting in the generation of an electron-hole pair [6].

Lastly, an event where the defect level acts as a trap centre. The trapping process is identified as a two-step process where a carrier is captured at the defect centre and subsequently injected back into the band where it came from. This is indicated by the combinations (2)+(1) or (3)+(4) which show that the defect centre interacts with only one of the two bands [6].

Shockley, Read, and Hall formulated a theory of recombination through defects from statistical considerations of the four elementary processes and determined the recombination rate related to a single defect level as a function of the defect, material and excitation parameters [6],[7].

The SRH lifetime, $\tau_{SRH}$ can be found by Equation 13, based on the assumptions that the densities of electrons and holes are $n = n_0 + \Delta n$ and $p = p_0 + \Delta p$, respectively, and that carrier trapping is negligible ($\Delta n = \Delta p$) [6].

$$\tau_{SRH} = \frac{\tau_{\mathrm{n0}}(p_0 + p_1 + \Delta n) + \tau_{\mathrm{p0}}(n_0 + n_1 + \Delta n)}{p_0 + n_0 + \Delta n} \tag{13}$$

where $\tau_{\mathrm{n0}}$ [s] and $\tau_{\mathrm{p0}}$ [s] are the capture time constants of electrons and holes, respectively and $n_1$and $p_1$ are the electron and hole SRH densities respectively. SRH recombination through a single trap state can be explained by Equation 14 [2].

$$U_{SRH} = \frac{n - n_0}{\tau_{\mathrm{n,SRH}}} \tag{14}$$

where $U_{\mathrm{SRH}}$ [$\mathrm{cm^{-3}s^{-1}}$] is the net recombination rate via defects. The minority carrier lifetime $\tau_{\mathrm{n,SRH}}$ [s] depends upon the density of trap states, as well as their position within the band gap, as can be seen in Equation 15

$$\tau_{n,SRH} = \frac{1}{B_{\mathrm{n}} N_{\mathrm{t}}} \tag{15}$$

where $B_{\mathrm{n}}$ is a coefficient for SRH recombination [$\mathrm{cm^{-3}s^{-1}}$] and $N_{\mathrm{t}}$ [$\mathrm{cm^{-3}}$] is the density of trap states [2]. In room temperature SRH processes dominate in doped p-type silicon, giving rise to a $\tau$ value of about 10 $\mu$m. In heavily doped silicon or at higher temperatures, Auger dominates. Radiative lifetimes in silicon are extremely long and never dominate the recombination in a practical solar cell [12].

### 2.4.4 Surface recombination through defects

Defects are most likely to occur at the surfaces in monocrystalline materials [2]. The silicon surface edge presents an abrupt discontinuity in the crystal structure, as it has partially bonded atoms [6]. The partially bonded atoms result in an increase in the density of recombination-active defect levels located in the band gap, near the semiconductor surface [6]. The localised states at the surface may also be extrinsic impurities that have been deposited from the external environment [2]. In these cases the trap states are concentrated in a two-dimensional space rather than a three-dimensional space as in the case of bulk defects [2].

Surface recombination differs from bulk recombination in the sense that the interface states do not normally occupy a single energy level, but are continuously distributed throughout the band gap. The activity of the semiconductor surface can be measured by the surface recombination velocity (SRV, denoted $S_{\mathrm{n}}$ [cm/s] for electrons and $S_{\mathrm{p}}$ [cm/s] for holes), and is defined in Equation 16, for electrons and holes respectively [2].

$$S_n = B_n N_s, \text{ [2]} \qquad S_p = B_p N_s, \text{ [2]} \tag{16}$$

where $N_s$ [$cm^{-3}$] is the density of traps per unit area. The SRV allows the quality of surface passivation to be assessed. The velocity at which the carriers diffuse into the surface to recombine cannot exceed $S = 10^7$ cm/s. The reason for this maximum speed at which carriers can move is related to the thermal energy [6]. Equation 17 represents the surface recombination rate as equivalent to the surface recombination rate $U_s$ divided by the carrier density [6].

$$S \equiv \frac{U_s}{\Delta n} \tag{17}$$

where $U_s$ [$cm^{-2}s^{-1}$] is the surface recombination rate, and $\Delta n$ is the excess electron density.

For electrons in p-type silicon, the surface recombination velocity at untreated surfaces and at interfaces with metallic contacts is in the range of $10^3 - 10^5$ $cms^{-1}$. Through surface passivation, the surface recombination rate reduces $S_n$ to less than 100cm $s^{-1}$. The surface recombination rate is reduced due to a reduction in the number of defects and impurities at the surface of the semiconductor [2].

Electron and hole mobilities are determined by the frequency of scattering events within the conduction and valence band. At low doping levels scattering is dominated by the silicon lattice and at high doping, mobility decreases because the impurity atoms generate scattering centres [2].

## 2.5 Passivation

The steadily increasing bulk carrier lifetimes of crystalline silicon (c-Si) wafers for application to commercial c-Si solar cells make recombination at the cell surfaces and contact the major fundamental limitation in today's c-Si solar cells [2].

The silicon surface has a high surface recombination velocity which tends to create a layer where photogenerated carriers are not collected. This can be prevented by passivating the surface. Passivation is performed by creating a thin layer of a wide band gap insulator that prevents carriers from reaching the surface and hence reduces the effective surface recombination velocity. The passivation reduces the loss of carriers in the emitter through surface recombination and a higher lifetime can be measured compared to that of an unpassivated surface [2].

If the surface passivation is of good quality the effective lifetime can be described by only the bulk lifetime Equation 18 [6].

$$\frac{1}{\tau_{\text{eff}}} = \frac{1}{\tau_{\text{bulk}}} \tag{18}$$

One mechanism to reduce the surface recombination rate at the surfaces is by optimizing the interface properties. This mechanism includes reducing the interface trap density. It is common to passivate dangling silicon bonds with oxygen or nitrogen atoms and hydrogen atoms, which reduces the interface trap density by several orders of magnitude. Each modification of the interface directly modifies the recombination-active interface states, which generally implies a change in the characteristic defect properties [6].

## 2.6 Resistivity and sheet resistance

Resistivity and sheet resistance are important factors for the determination of the electrical properties of a semiconductor, as well as carrier lifetime.

One parameter related to the resistivity is the resistance ($R$) which is related to the rate at which carriers recombine at the surface of the semiconductor device. The resistance of a semiconductor is a measure of the opposition to the flow of electrical current through the device and is typically

measured in ohms (Ω) [13]. The resistance is a geometrical-dependent parameter and is equal to the voltage (V) [volt] across the material divided by the current (I) [ampere] flowing through it. The inverse parameter of the resistance is the resistivity ($\rho$) [$\Omega \cdot$ cm] [13]. The resistivity is independent of the material geometry which is opposite to that of the resistance [2]. These two parameters are related through Equation 19 [13].

$$\rho = R\frac{A}{l} \tag{19}$$

where l is the distance between the two points at which the voltage is measured, and A is the cross-sectional area perpendicular to the direction of the current. If the length, l, is 1m and the cross-sectional area, A, is $1m^2$ the conductivity ($\sigma$) $\Omega^{-}1]$ is the reciprocal of the resistivity, as seen in Equation 20. The resistivity is dependent on the free electron and hole densities n and p and their mobilities, $\mu_{\mathrm{n}}$ [$\mathrm{cm^2V^{-1}s^{-1}}$] and $\mu_{\mathrm{p}}$ [$\mathrm{cm^2V^{-1}s^{-1}}$], respectively, shown in Equation 20 [13]. This means that the resistivity of a semiconductor material depends on the level of doping. In doped material, resistivity will be dominated by the majority carrier density and mobility.

$$\rho = \frac{1}{q(n\mu_n + p\mu_p)} = \frac{1}{\sigma} \tag{20}$$

where $q$ [C] is the elementary charge. The electrical conductivity seen from Equation 20, is heavily dependent on the mobility of the charge carriers [14].

Another material property to consider when measuring the carrier lifetime is the sheet resistance $R_{sheet}$ [$\Omega/\square$], as this parameter influences the carrier lifetime measurements. The sheet resistance is directly proportional to the resistivity and reciprocal to the thickness of the sample, $W$, shown in Equation 21 [13].

$$R_{\mathrm{sheet}} = \frac{\rho[\Omega \cdot \mathrm{cm}]}{W[\mathrm{cm}]} = \frac{1}{q(n\mu_{\mathrm{n}} + p\mu_{\mathrm{p}})W} = \frac{1}{\sigma W} \quad [\Omega/\square] \tag{21}$$

The sheet resistance is related to the carrier lifetime in semiconductor devices because it is directly related to the recombination rate at the surface of the device. When measuring the lifetime, the instrument uses the sheet resistance and resistivity, and the value before and after passivation should stay the same as passivation does not change this property.

To ensure accuracy while measuring the carrier lifetime, the sheet resistance has to be investigated. This parameter is measured using a 4-point probe to measure the voltage output and its corresponding input current. These values can then be used to calculate the sheet resistance Section 4.3.

The conductivity and excess carrier density are related through Equation 22 [13].

$$\Delta n = \frac{\Delta\sigma}{q(\mu_{\mathrm{n}} + \mu_{\mathrm{p}})} \tag{22}$$

The excess carrier density relates to the lifetime, hence the conductivity and sheet resistance through the following

$$\tau = \frac{\Delta n}{U} = \frac{\Delta\sigma}{q(\mu_{\mathrm{n}} + \mu_{\mathrm{p}})U} = \frac{\Delta\sigma\rho}{U} = \frac{\Delta\sigma R_{sheet}W}{U} \tag{23}$$

which shows how the sheet resistance and the conductivity influence the lifetime, and the interdependencies.

# 3 Lifetime characterization techniques

There are different techniques to measure the carrier lifetime, two of these will be explained in this section. Carrier lifetime is measured based on the recombination dynamics of excess carriers. The

excess carrier density measurements are dependent on the time of illumination and the measurement technique. One technique involves a sharp pulse of illumination that is rapidly switched off and then the excess carrier density without illumination can be determined. This method is known as the transient photoconductive decay (PCD) technique and is usually used to measure high carrier lifetimes [6]. Another technique is the quasi-steady-state (QSSPC) method, first introduced by Sinton and Cuevas in 1996 [15]. This method includes slowly decaying light intensity til zero over several milliseconds. This slow decay ensures that the sample remains in a steady state in terms of the recombination processes. The QSSPC method has the advantage that a large range of the operating points easily can be explored [6].

Nagel et. al ([9]) proposes a generalized analysis procedure that covers both the PCD and the QSSPC technique regardless of the decay time of the illumination source. The expression found in the article [9] combines the bulk and surface recombination rates into an effective carrier lifetime $\tau_{\text{eff}}$ as seen in Equation 24

$$\tau_{\text{eff}} = \frac{\Delta n_{\text{av}}}{G_{\text{av}} - \frac{\mathrm{d}\Delta n_{\text{av}}(t)}{\mathrm{d}t}} \tag{24}$$

where $n_{\text{av}}$ and $G_{\text{av}}$ are the average excess carrier density and the average generation rate, respectively. In the case of the quasi-transient method, the generalized case can be simplified as $G = 0$.

$$\tau_{\text{eff}} = \frac{\Delta n_{\text{av}}}{\frac{\mathrm{d}\Delta n_{\text{av}}(t)}{\mathrm{d}t}} \tag{25}$$

This is only valid when the carrier lifetime is significantly higher than the decay of the illumination source. Quasi-steady-state presents a case that is under steady-state conditions, meaning $\mathrm{d}\Delta n/\mathrm{d}t \equiv 0$, which gives the following expression for the lifetime.

$$\tau_{\text{eff}} = \frac{\Delta n_{\text{av}}}{G_{\text{av}}} \tag{26}$$

which is only valid when the decay of the illumination source is significantly longer than the carrier lifetime.

From equation 24-26, one can observe that in order to determine the effective lifetime, the time dependence of the excess carrier density and the generation rate has to be measured. To measure the time dependence of the excess carrier density, different techniques can be used. For this reason, the quasi-steady state photoconductance technique (QSSPC) and the Transient photoconductive decay (PCD) method will be presented in the following.

## 3.1 Transient photoconductive decay method - (PCD)

The transient photoconductive decay (TPCD) method is a well-established technique that has been widely used for characterizing semiconductor materials and devices [16].

TPCD assumes a highly effective minority carrier lifetime determined by bulk and surface recombination mechanisms [16]. To determine the lifetime this technique uses a pulsed light source to generate electron-hole pairs in a sample biased under constant current conditions [16]. This changes the conductivity in the sample which results in a change in the voltage across the sample. The lifetime at each carrier density, $\Delta n$, can be determined through the following equation [6]

$$\tau = \frac{\Delta n}{\mathrm{d}\Delta n/\mathrm{d}t} \tag{27}$$

There are some limitations to the TPCD method, as the carrier lifetime is dependent on factors such as the semiconductor material, light source, filter thickness, and temperature [16]. To obtain accurate results, it is necessary to ensure that there is sufficient excess carrier density in the sample well after the flash has terminated. This requires that the flash turn-off time (50 $\mu$s) be shorter than the carrier lifetime. In other words, this technique is only valid for carrier lifetimes greater than 100 $\mu$s [5].

## 3.2 Quasi-steady-state photoconductance technique - QSSPC

An alternative method to the PCD method is to measure the photoconductance under steady-state illumination. This method, the quasi-steady-state photoconductance was first presented by Sinton Consulting in 1996 through the paper *Quasi-steady-state photoconductance, a new method for solar cell material and device characterisation* [4]. The technique developed is well-suited for measuring the carrier lifetime over a wide range of carrier injection levels [6].

The QSSPC method allows for direct measurements of the carrier injection level, without requiring device simulation. This method is a large signal technique that allows direct measurements of the carrier lifetime at any range of injection levels without integrating differential quantities. In addition, this technique provides accurate lifetime measurements over a large injection range in one flash [6].

The experimental work in the present study is based on the *BCT-300 Photoconductance Lifetime Tester* apparatus from Sinton consulting. The instrument includes a flash lamp that optically generates carriers in the sample being measured. The instrument coil measures the excess carrier density ($\Delta n$) through the excess photoconductance, in other words, changes in the excess photoconductance $\Delta\sigma(t)$ of the sample. The instrument then calculates the average excess carrier density through the following expression:

$$\Delta n_{av} = \frac{\Delta\sigma(t)}{q(\mu_n + \mu_p)W} \tag{28}$$

The photogenerated excess carrier density, $\Delta n = \Delta p$, results in an increase in wafer conductance given by:

$$\sigma_L = q(\Delta n\mu_n + \Delta p\mu_p) \tag{29}$$

Under a steady state, the generation of electron-hole pairs must be in balance with the recombination of these same pairs. The total recombination in the wafer can be expressed in terms of an effective minority carrier lifetime, $\tau_{eff}$ shown in Equation 26 [4].

# 4 Materials and methods

This chapter introduces the material used, sample preparation, and instruments used during the experimental work. The instruments used for this report are Sinton instruments BCT-300 and Jandel 4-point probe. The samples used in this report are described in Section 4.1. The lifetime spectroscopy instrument and its related processes will be explained in Section 4.2, followed by the Jandel four-point probe in Section 4.3.

## 4.1 Sample and sample preparation

The samples investigated in this report are p-type boron-doped monocrystalline silicon produced by Czochralski (Cz) method. The samples are cut out from an ingot produced in SINTEF's Heliosi lab with the Czhockralski furnace. From the ingot, a block was cut out. From the block, 8 samples were cut from the bottom, noted B, and from the top, noted T. The samples are also denoted by numbers. The lowest number represents the sample cut furthest into the sample, whereas the largest number represents the first cut sample. The thinnest samples ($\leq$ 200 $\mu$m) were found from another project, as it was not possible to polish the samples from the block to this desired thickness. From the block, five wafers were cut three from the bottom, 9B: 557 $\mu$m, 10B: 555 $\mu$m, 12B: 968 $\mu$m, and two from the top, 2T: 500 $\mu$m and 5T: 500 $\mu$m. Additionally, three bricks with a thickness of 1cm were cut from the bottom: 14B and 15B, and from the top: 7T. Lastly, the thinner wafers not from the block are denoted and have a thickness of the following: 1T: 166 $\mu$m, 2T: 164 $\mu$m, 3T: 166 $\mu$m, 4T: 166 $\mu$m, 1B: 200 $\mu$m, 2B: 200 $\mu$m, 3B:200 $\mu$m, 4B: 200 $\mu$m

To accurately measure the sample lifetime, the bulk recombination properties have to be determined. this requires a reduction in the impact of the surface recombination so that the only contribution when measuring the effective lifetime comes from the bulk. For this reason, the samples were sent to IFE (Institutt for energiteknikk) for passivation after the first measurements. Then the measurements were performed again on the passivated samples. The passivation performed by IFE included a CP5-ets etching to remove any unwanted substances on the surface [17]. Followed, an elimination of any organic residue on the substrate using a Piranha cleaning which is a mixture of sulfuric acid ($H_2SO_4$) and hydrogen peroxide ($H_2O_2$) on the wafers [18]. Before the Plasma enhanced chemical vapour deposition (PECVD), the oxide layer was removed, followed by passivating the wafers by depositing one layer of a-Si:H on each side.

## 4.2 BCT-300

The instrument used to measure lifetime is a Sinton Instrument BCT-300. To make sure that the instrument is properly working the instrument has to be qualified, calibrated, and then the lifetime can be measured.

The BCT-400 measurement systems use an eddy-current conductance sensor and a filtered xenon flash lamp to measure carrier lifetime in silicon samples. Measurements can be taken using either a Quasi-Steady-State-Photoconductance (QSSPC) method or a Transient Photoconductance Decay (Transient PCD) method. The instrument is mainly meant for lifetime measurements on monocrystalline or multi-crystalline silicon ingots or bricks that are either thinner than 1mm or larger than 1cm.

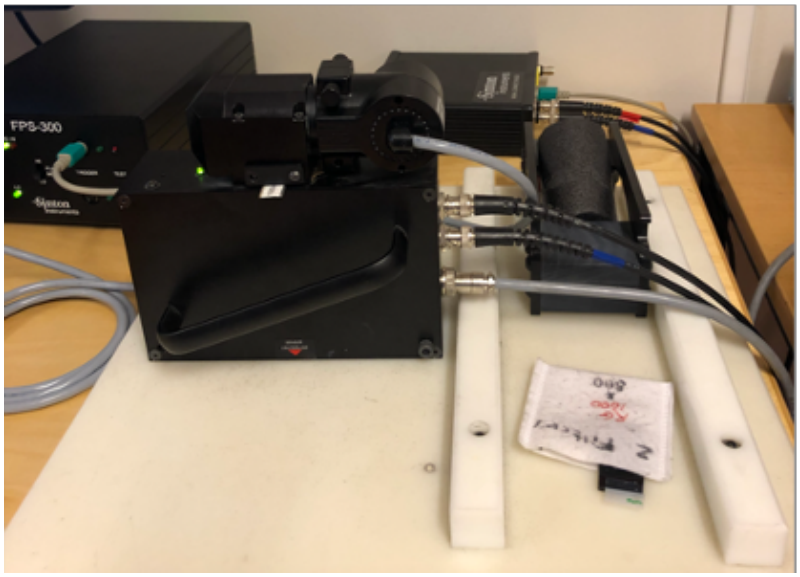


**Figure 9:** BCT-300 measuring device with flash lamp and flash device FPS-300.

The instrument allows for silicon quality assessment directly after growth without requiring surface passivation as the instrument is able to measure the bulk lifetime. The primary application of the BCT-400 system is the qualification of high-purity silicon with lifetimes in the 1-10 milliseconds range, qualifying as grown p-type-Cz silicon without special surface preparation, and the characterization of lifetime and trap density in multi-crystalline silicon blocks [5]. The instrument gives best lifetime measurements from 0.1$\mu$s to greater than 10ms, and the best resistivity measurement in the range of 0.5-20 $\Omega \cdot$ cm [5].

### 4.2.1 Qualifying the tester

Qualifying the tester is a crucial step to determine the accuracy of the results obtained by the instrument. When qualifying the instrument, the total sheet resistance is checked. This should lie in the range of $+/-$ 10% of a measured reference wafer. If that is not the case, the instrument has to be calibrated.

The first step when qualifying the tester is checking that the flash (FPS-300) was set to LO (LOW) flash mode and that the 1000nm filter is installed in the filter slot. The software used when qualifying the tester is the *WaferLifetimeSoftware*. In the software, the values of sample thickness (cm), and base resistivity ($\Omega \cdot$ cm) need to be updated for every sample. The instrument is then ready to be zeroed and pressing "Zero Instrument". The process of zeroing the instrument should be completed when a new sample is being measured. Then the instrument is ready to measure a sample. This is done by placing the sample on the plastic measurement platform and then placing the BCT-300 instrument on top. Then by pressing "Measure Wafer" a graph showing raw voltage, and a table depicting measurement results are shown as in Figure 10 and Figure 11. The row voltage plot shows whether the measurement is accurate or must be repeated. This is shown together with the scaling options, and the autoscale button. By autoscaling, the instrument takes the desired number of measurements and averages the results.

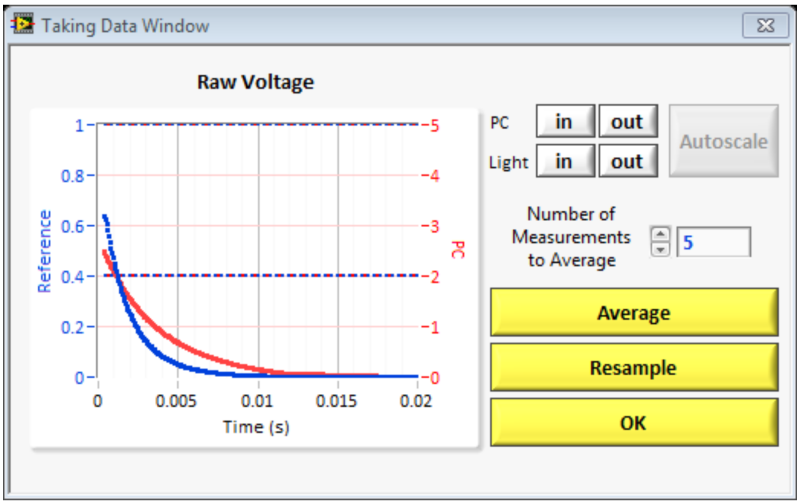


**Figure 10:** Information output of raw voltage as a function of time from the BCT-300 instrument during qualifying the tester with the *WaferLifetimeSoftware* Software. The graph is an indication of the quality of the measured sample.

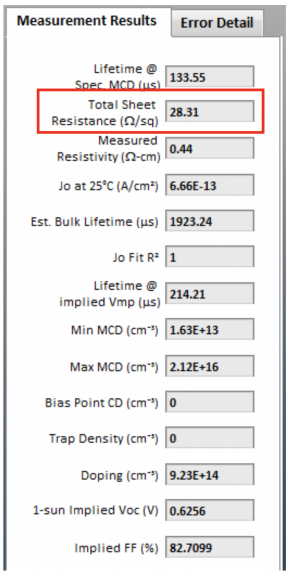


**Figure 11:** A snapshot of the results output in the *WaferLifetimeSoftware* during qualifying the tester, when the sheet resistance of reference wafer is determined.

### 4.2.2 Calibration

During wafer calibration, there was only information about the thickness and resistivity. Using Equation 21 the total sheet resistance can be calculated. Here $\rho$ is the resistivity, $R_S$ is the sheet resistance, and w is the thickness.

The calibration input values are the number of samples, and the sheet resistance values corresponding to each sample. This measures the output voltage of the instrument, on the sample. Then the sample is removed and the instrument is placed on the plastic measurement platform in order to measure the output air voltage [5]. Once all samples have been measured, the software will perform a fit to find the calibration constants. This gives calibration curves that will look similar to those shown in Figure 12 and Figure 13.

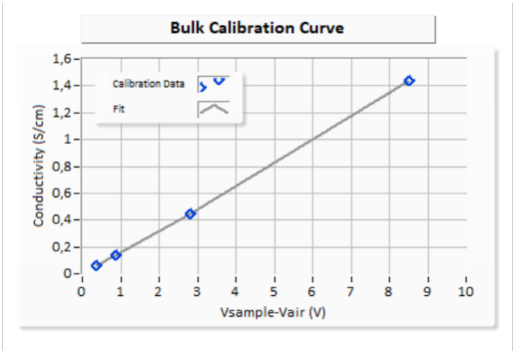


**Figure 12:** Calibration curve for bulk samples with conductivity as a function of the voltage, which is the sample voltage minus the air voltage.

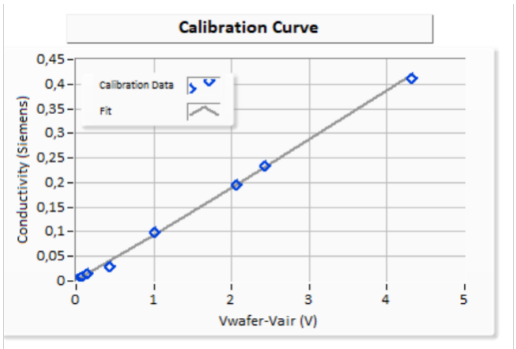


**Figure 13:** Calibration curve for wafers with conductivity as a function of the voltage, which is the sample voltage minus the air voltage.

Using

$$\sigma = A(V - C)^2 + B(V - C), \tag{30}$$

the voltage output of the instruments' eddy current sensor is converted to (a bulk or wafer) conductivity in Siemens [$\Omega^-1$]. Here A, B, and C are obtained from the calibration curves. This allows for the conversion of the instrument voltage output to a calibrated resistivity value [5]. "C" in the calibration curve corresponds to the voltage output from a theoretically perfect undoped wafer. The instrument's response to air should also be a theoretically perfect point which is usually at a voltage just below that of an undoped wafer [5]. The calibration curves shown in Figure 12 and Figure 13 show the difference between wafer voltage and air voltage on the x-axis, and wafer conductance in Siemens on the y-axis [5].

When using the BCT-400 instrument from Sinton instruments to measure the conductivity of semiconductor material, it is important to take into account the potential impact of changes in the instrument's operating temperature on the accuracy of the measurements. The calibration curve used to determine conductivity can be shifted to the right or left by changes in temperature, and an accurate measurement of conductivity depends on normalizing the calibration curve to the undoped ("zero"-conductivity) sample for any given operating conditions. To minimize errors in the measurements, the BCT-400 instrument subtracts the air voltage from the measured sample conductivity. The value C in Equation 30 represents the undoped conductivity and serves as a reference point on the calibration curves shown in Figure 12 and Figure 13. It is also important to "zero the instrument" between every measurement to ensure accurate results.

### 4.2.3 Measuring lifetime on wafers and silicon ingot/bulk

Lifetime measurements of the samples can take place after calibration and qualifying the tester. The instrument is not optimized for measuring wafers as the wafers easily break [5]. For this reason, the user manual recommends using the Sinton instruments' specific wafer measurement tools (the WCT-120) [5]. For this work Sintons' instrument, BCT-300 is used with great caution.

The first step is to turn on the instrument and ensure that all components are connected [5]. Then the instrument has to be left on for 30 minutes to reach a stable internal temperature. The instrument is ready to be used when the green LED is glowing. The red LED will turn on and off as it is keeping the instrument at a constant temperature, 25°C. Before starting the measurements the correct filter should be inserted in the filter slot. Then the measurements can be taken.

When measuring either wafers or bricks, the measurement mode is decided by the inserted filter. The mode and filter are decided depending on the lifetime of the sample measured, as shown in Table 1. When the filter is inserted the flash setting, Flash Power Supply(FPS) - 300, has to be on high (HI) during Transient analysis mode and low (LO) in QSSPC analysis mode. Before measurements could be taken, the base resistivity (in $\Omega \cdot$ cm) and the sample type (n- or p-type substrate) had to be specified. The minority carrier density (MCD) also had to be specified, and according to Table 1:

**Table 1:** Specified MCD based on analysis mode.

| Illumination mode | Analysis Type | Specified MCD ($cm^{-3}$) | Lifetime range $\mu$s | Filter |
|---|---|---|---|---|
| Quasi-Steady-State | QSS1000 | 1E15 $cm^{-3}$ (p-type) | $< 200$ | 1000nm |
| | QSS850 | 5E14 $cm^{-3}$ (n-type) | $< 2$ | 850nm |
| Transient | Transient | 1E15 $cm^{-3}$ (p-type) | $> 100$ | 850nm |
| | Transient | 5E14 $cm^{-3}$ (n-type) | $> 100$ | 850nm |

When these steps are done, the instrument can be zeroed. This is performed by placing the instrument on top of the plastic measurement platform and clicking the "Zero the instrument" button. Then the samples can be measured, by placing the instrument on top of the sample and making sure that the sensor region is completely in contact with the sample. The lifetime is usually reported as a function of MCD. The results obtained from the measurements are represented in a table, and the conductance sensor voltage and the light sensor voltage as a function of time are

visualized in a graph. The data obtained from each individual measurement was then collected and downloaded as a text file for later processing.

## 4.3 4-Point Probe

To perform resistivity measurements on wafers and bricks (W$\geq$ 5mm), a Jandel 4-point probe (4PP) instrument is used. The sample should have a clean and plain measurement area for accurate results.

### 4.3.1 Jandel 4PP

The instrument consists of a measurement probe holder (with dummy) (Figure 14), and a measurement probe (Figure 15), measurement probe holder (with probe) Figure 16), and steering unit (Figure 17)

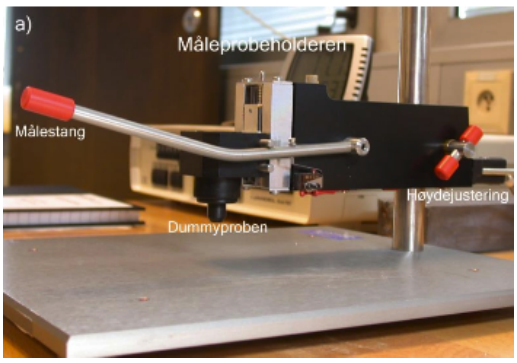


**Figure 14:** Measurement probe holder with a dummy, where "måleprobeholder" is the measurement probe holder, "målestang" is the measurement pole. "Dummyproben" is the dummy probe used to protect the pins on the measurement probe as they can easily be destroyed while adjusting the instrument height. lastly "høydejustering" is used to adjust the height of the instrument.

**Figure 15:** 4-point probe [19].

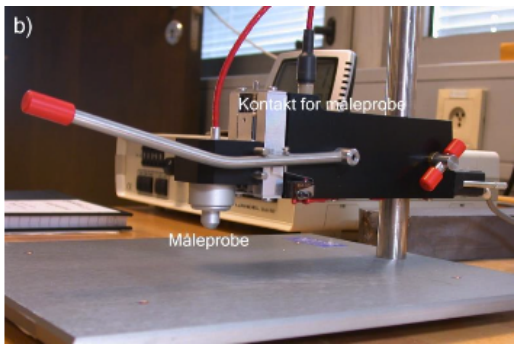


**Figure 16:** Measurement probe holder with the probe, where "kontakt for måleprobe" is the cord from the instrument to the probe that measures the resistivity. "Måleprobe" is the measurement probe.

**Figure 17:** Steering Unit that allows changing the applied current and shows the output voltage measured on the sample.

Before measuring, the instrument had to be adjusted to the correct height to ensure good contact between the sample and the probe. The dummy probe has to be inserted in the instrument when adjusting it to sufficient contact with the sample is achieved. The dummy has to be used

to prevent damage to the pins on the probe in the adjusting process. When the correct height is achieved the dummy probe can be changed with the measurement probe (Figure 15). There are two measurement probes following this instrument. For wafers and bricks (brick thickness > 10mm) the probe with the largest distance between the sticks (1.591mm) should be used. For bricks with a thickness between 5-10 mm the probe with the smallest distance between the sticks should be used. Which probe to use depends on the thickness and the quality of the sample.

When the probe is not measuring or in contact with the sample, the steering unit should be in standby (STBY) mode. It is recommended to have a current in, on 100 $\mu$A together with the x10 button, this will give a current of 1mA to the measurement probe. If the current is too high, results may be faulty. This is especially on samples with high lifetime and high resistivity. The voltage button should be on 200mV, as this decides the number of decimals in the output voltage window. The filter button should be turned off as it should only be used when measuring samples with high resistivity.

When measuring a sample the steering unit has to be in forward (FWD) mode. When the sample is being measured a click can be heard, which indicates that the probe and sample are in sufficient contact. Then FWD can be pressed. When the measured voltage has stabilised, press STBY and wait til 0V is shown in the display. Then reverse (REV) can be pressed. When the voltage in the display has stabilised, note the value. The absolute value of the voltage in REV and FWD mode should be approximately the same +/− a deviation of 1-2%. Before lifting the probe up, STBY should be pressed. When measuring a sample, it is normal with 5 measurements per sample.

If during a measurement, compliance volts start to light, it means that the steering unit is not able to apply the desired current. Then either the applied voltage can be reduced by turning the compliance button, or decrease the current. If compliance volts are lighting up for a sample with low resistivity, this may indicate a bad connection between the probe and the sample.

When the voltage has been found, this value can be used to calculate the resistivity in $\Omega \cdot$ cm for wafers using

$$\rho = \frac{4.532VW}{I} \tag{31}$$

where $W$ [cm] is the thickness of the sample in cm, $V$ [mV] is noted voltage and $I$ [mA] is the set current on the probe. To use Equation 31 the wafer has to be no thicker than 0.3 times the pin distance. For samples thicker than 0.3 times the pin distance, a correction factor has to be multiplied. 4.532 is a correction factor derived from $\pi/ln(2)$. This factor is included in the equation for the sheet resistance as the samples satisfy the constraint of W$\leq$s/2, where s is the distance between the pins on the measurement probe.

One assumption when measuring the resistivity is that the area measured has an infinite area. This means that the d$\gg$s, where d is the diameter or length of the sample and s is the distance between the pins on the probe, are shown in Figure 18. For very thin samples and samples with a thickness greater than 5% of the probe spacing, a correction factor has to be multiplied by the resistivity. The correction factor can be found in Figure 38 in the appendix. The correction factor is important as it accounts for an overestimation of the sheet resistance. This has to do with the current paths between the probes as they are limited by the proximity to the edges of the sample [14].

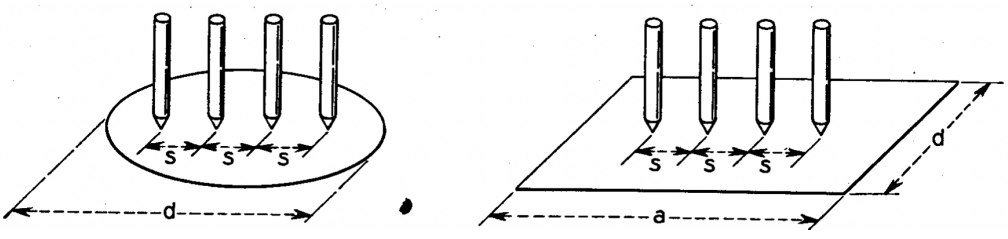


**Figure 18:** Schematic of 4 Point Probe dimensions [14].

# 5 Results and Discussion

This section will illustrate the results obtained during the experimental work and discuss the results in relation to the theory and relevant papers.

## 5.1 Preparation

To achieve high-quality lifetime measurements with the BCT-300 instrument, it had to be calibrated. Calibration required resistivity measurements of the wafers used for calibration. To ensure that the calibration was of good quality, the instrument had to be qualified.

### 5.1.1 Qualify the tester, BCT-300


**Figure 19:** three reference wafers used to Qualify the tester.

To qualify the tester three reference wafers (Figure 19) with known sheet resistance and resistivity were used. Table 2 shows the results obtained when qualifying the tester before calibration and after the first and second calibrations. The second column represents the known sheet resistance for the three wafers, and the third column represents the measured sheet resistance before calibration. These values differ more than $+/-$ 10% which is the given error interval in which the sheet resistance is acceptable. For this reason, the instrument had to be calibrated. After the first calibration, one can observe that a majority of the sheet resistance values obtained are outside the uncertainty range of $+/-$ 10%. Thus a new calibration had to be performed. The values obtained during qualifying the tester after 2nd calibration proved to be in the given range, as depicted in the last column in Table 2. However, the value of the sinton262 reference cell is outside this error interval but it was decided that this value was acceptable.

**Table 2:** Total Sheet resistance on reference wafers before and after calibration.

| Total sheet resistance ($\Omega \cdot$ cm) | | | | | | | |
|---|---|---|---|---|---|---|---|
| ID | Reference | Measured | % Abs diff | 1st Calibration | % Abs diff | 2nd Calibration | % Abs diff |
| Sinton262 | 26.2 | -145.7 | -287.7 | 30.4 | 14.8 | 29.9 | 13.5 |
| Sinton584 | 58.4 | 3.1 | 179.8 | 62.6 | 6.9 | 61.6 | 5.3 |
| Sinton1000 | >1000 | 4.7 | 198.1 | 1886.9 | 61.4 | 1013.7 | 1.4 |

### 5.1.2 Calibration


**Figure 20:** 6 wafers used for calibration of BCT-300, values can also be found in Table 4.


**Figure 21:** Bricks used for calibrating the BCT-300 instrument, in total 4 bricks. The known values of each brick can be found in Table 4.

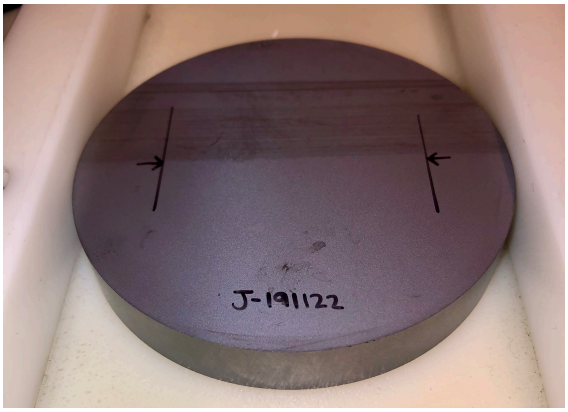


**Figure 22:** Brick used for brick calibration of BCT-300.

The calibration was performed using the method explained in Section 4.2.2. The wafer calibration was performed using the six wafers depicted in Figure 20 with properties found in Table 5 were used. The brick calibration was performed using the same method as for the wafers, on

four bricks depicted in Figure 21 and Figure 22 with properties found in Table 5. The obtained calibration curves for the second calibration for bricks and wafers are illustrated in Figure 23 and Figure 24, respectively. The calibration performed was depicted as a good fit and used throughout all experimental work.

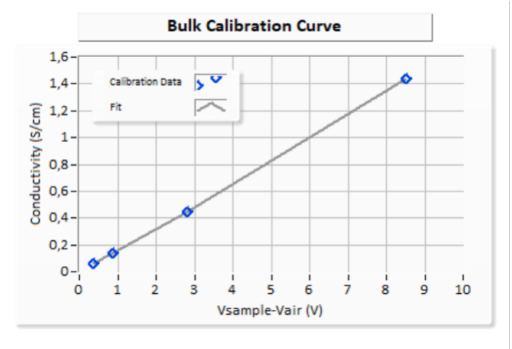


**Figure 23:** Calibration curve for brick samples.

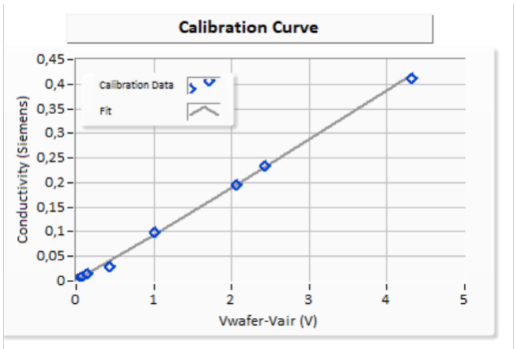


**Figure 24:** Calibration curve for wafers.

## 5.2 Resistivity measurements

The resistivity measurements were performed on the three reference wafers (Figure 19), both by 4PP method, following Section 4.3, and by the BCT-300 instrument as depicted in Table 3. In Section 4.3 it is stated that for very thin samples or for samples where an infinite surface area can not be assumed, for instance, due to breakage, a correction factor has to be added. The reference cell Sinton 58.4 is broken, meaning that an infinite surface area cannot be assumed. For this reason, a correction factor, which can be found in Figure 38 has to be used. The correction factor is found by dividing the sample thickness (0.0525 cm) by the pin spacing on the measurement probe (0.0635 cm). This gives a correction factor (0.0525cm/0.0635cm = 0.8) corresponding to 0.9662. Through Table 3 it is observed that the 4PP method gives accurate resistivity values for all wafers. From the values obtained from the BCT-300, it can be seen that for low resistivity the instrument measures resistivity values that are acceptable. This is however observed opposite for high resistivity. From Section 4.2 it is known that the BCT-300 is optimized to measure samples with a resistivity lower than 20 $\Omega \cdot$ cm [5] which causes more error while measuring higher resistivities.

**Table 3:** Resistivity ($\rho$) measurements from Jandel 4PP and BCT-300.

| ID | Reference $\rho$ [$\Omega \cdot$ cm] | 4PP $\rho$ [$\Omega \cdot$ cm] | BCT-300 $\rho$ [$\Omega \cdot$ cm] |
|---|---|---|---|
| Sinton262 | 1-2 | 1.40 | 1.57 |
| Sinton584 | 1-5 | 2.95 | 3.23 |
| Sinton1000 | 40 | 42.67 | 53.22 |

The assertion is supported by the data obtained from Sinton1000, which demonstrates a higher resistivity measured by the BCT-300 compared to the 4PP method. This can be attributed to the fact that as the resistivity increases, the voltage differences between the air and the sample become more similar, resulting in a larger margin of error in the measurement of resistivity when utilizing the BCT-300 [6]. The data obtained for resistivity measurements above 20 $\Omega$cm, utilizing the 4PP method yields more reliable data compared to the use of the BCT-300 instrument.

**Table 4:** Known values for the six wafers used for calibration, displayed in Figure 20, and the four brick samples used for brick calibration, displayed in Figure 21.

| Reference values of the six wafers | | | |
|---|---|---|---|
| ID | $\rho$ [$\Omega \cdot$ cm] | $W$ [cm] | $R_{\text{sheet}}$ [$\Omega/\square$] |
| Cal_6_0.5 | 0.51 | 0.025 | 20.33 |
| Cal_6_0.75 | 0.74 | 0.026 | 28.58 |
| Cal_6_1 | 0.97 | 0.026 | 37.03 |
| Cal_6_2 | 2.12 | 0.025 | 82.75 |
| Cal_6_4 | 4.35 | 0.025 | 170.66 |
| Cal_6_10 | 10.03 | 0.025 | 393.64 |

| Reference values of the four bricks | |
|---|---|
| ID | $\rho$ [$\Omega \cdot$ cm] |
| F-193531 | 0.69 |
| H-191083 | 7.37 |
| G-193558 | 2.24 |
| J-191122 | 17.37 |

The 4PP was also performed on the six wafers depicted in Figure 20 with results obtained displayed in Table 5. Table 4 displays the reference value of these six wafers, where the sheet resistance was calculated using Equation 21 and the reference values of resistivity and wafer thickness.

**Table 5:** Values obtained from 4PP with absolute error in relation to the reference sheet resistance value from Table 4.

| | Values calculated based on 4PP values | | | | | Values obtained from 4PP | | | | | | Error from reference value |
|---|---|---|---|---|---|---|---|---|---|---|---|---|
| ID | V [mV] | I [mA] | R [Ohm] | $R_{\text{sheet}}$ [$\Omega/\square$] | $\rho$ [$\Omega \cdot$ cm] | I [uA] | V #1 [mV] | V #2 [mV] | V #3 [mV] | V #4 [mV] | V #5 [mV] | Abs diff % |
| Cal_6_0.5 | 4.48 | 1 | 4.48 | 20.28 | 0.51 | 1000 | 4.49 | 4.48 | 4.48 | 4.46 | 4.47 | 0.28 |
| Cal_6_0.75 | 6.40 | 1 | 6.40 | 28.98 | 0.75 | 1000 | 6.37 | 6.38 | 6.40 | 6.41 | 6.43 | 1.41 |
| Cal_6_1 | 8.40 | 1 | 8.40 | 38.07 | 0.99 | 1000 | 8.41 | 8.42 | 8.41 | 8.39 | 8.39 | 2.80 |
| Cal_6_2 | 18.57 | 1 | 18.57 | 84.11 | 2.16 | 1000 | 18.58 | 18.56 | 18.55 | 18.55 | 18.6 | 1.65 |
| Cal_6_4 | 15.18 | 0.4 | 37.95 | 171.89 | 4.38 | 400 | 15.17 | 15.15 | 15.20 | 15.18 | 15.19 | 0.72 |
| Cal_6_10 | 8.90 | 0.1 | 88.96 | 402.99 | 10.27 | 100 | 8.87 | 8.92 | 8.91 | 8.91 | 8.87 | 2.37 |

Table 5 shows the set current value I, and the measured voltage output, V#1 − #5, measured 5 times, for accurate results. Using ohms law the resistance can be calculated, and using Equation 19 and Equation 21, the resistivity and sheet resistance was calculated. Looking at the absolute difference which compares the measured Table 5 and the known Table 4 the sheet resistance values obtained through the 4PP were acceptable and used to calibrate the BCT-300.

## 5.3 Lifetime measurements

Lifetime measurements were performed on the block and bricks using the transient analysis mode together with an 850nm filter and FPS-300 setting on high (HI). For all wafers measured the QSS1000 analysis mode was used together with the 1000nm filter, and FPS-300 setting on low (LO).

### Block

The block (Figure 25) was measured 4 times, labelled as measurement 1-4 in Figure 26 and Figure 27.

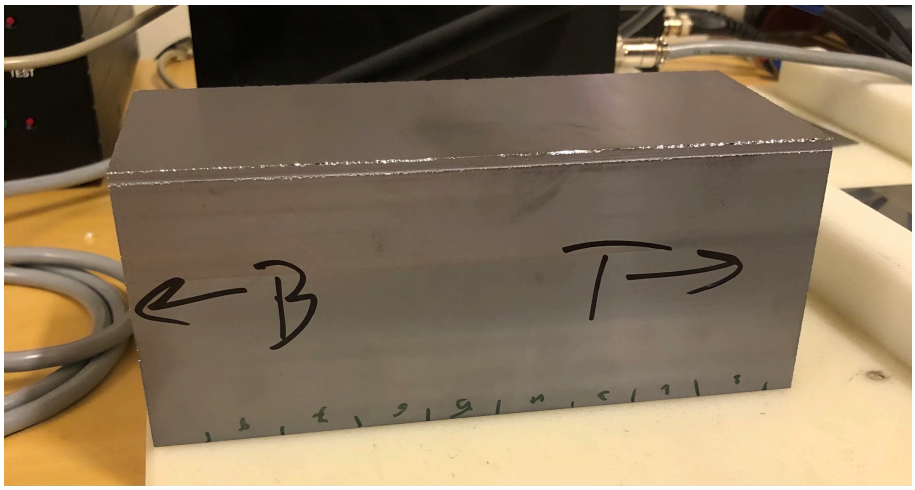


**Figure 25:** The block from which wafers and bricks are cut.

From Figure 26 and Figure 27 one can observe that both the resistivity and the estimated bulk lifetime through the block increase towards the bottom. According to Berthod, C. et. al, this increase observed may be caused by an increase in the boron concentration along the ingot height. In their paper *Experimental investigation of the optimal ingot resistivity for both the cell performances and the temperature coefficients for different cell architectures* it is also suggested that the average resistivity should be around 1.3 $\Omega \cdot$ cm [20]. To achieve this, the resistivity at the bottom of the ingot should be higher than that of the top [20], which is the observed trend for the block. The estimated bulk lifetime of the block (Figure 26) was plotted with a 5% error interval in order to understand where the bulk lifetime for the wafers could be excepted. In the case of the bottom samples, a lifetime between 255-290 $\mu$m can be expected from Figure 26 and in the case of the samples cut from the top a lifetime between 225-259 $\mu$m can be expected.

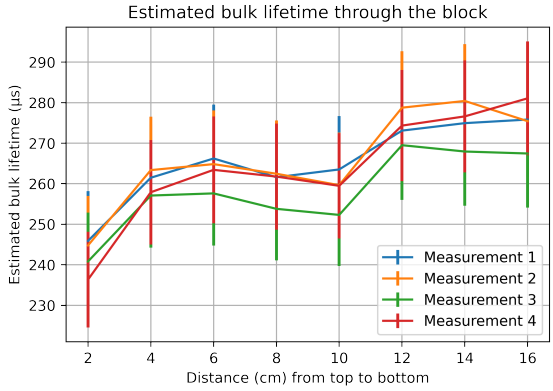


**Figure 26:** Lifetime measured through the block from top to bottom with a 5% error interval. A total of 4 measurements were performed on the block.

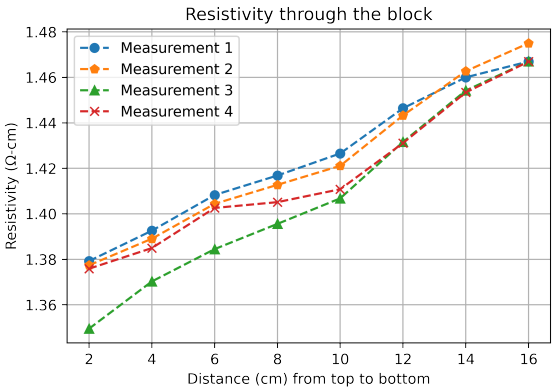


**Figure 27:** Resistivity through the block, measured from top to bottom. A total of 4 measurements were performed on the block.

### Bricks

Figure 29 illustrates the measured lifetime vs. carrier density for the three bricks displayed in Figure 28. The lifetime was measured using the transient mode, as the lifetime is greater than 100 $\mu$s. The lifetimes were measured twice for each sample, and can be seen to be identical from $3 * 10^{14} - 9 * 10^{15}\text{cm}^{-3}$. For carrier concentrations lower than $3 * 10^{14}\text{cm}^{-3}$ there is more variation shown in the measurements. The measurements were taken at 2 different times. The reason for the two obtained profiles of each sample can be dependent on the surface recombination, and doping

level variations in the sample if the measurements were not taken at the exact same position both times. From the lifetime as a function of carrier density profiles obtained it is observed that 7T which is cut from the top of the block and 15B, cut from the bottom of the block, have similar lifetime profiles compared to 14B, cut from the bottom. It was expected that both of the samples cut from the bottom would have similar lifetime profiles. The reason for this difference may be due to boron concentration variations in the samples or defects in the measured area.

The lifetimes are considered high, and the reason why the bricks obtain a high lifetime without being passivated can be seen in relation to the thickness of the samples together with the purpose of utilization area of the instrument. The reason is that the instrument is able to measure the lifetime in the bulk. From Equation 10, it can be seen that the effect that surface recombination has on the effective lifetime decreases with increasing wafer thickness. In other words, higher lifetimes will be measured on thicker samples [21].

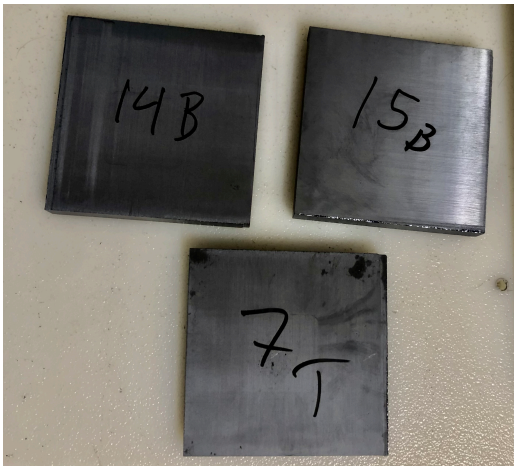


**Figure 28:** A total of three bricks were cut from the block.

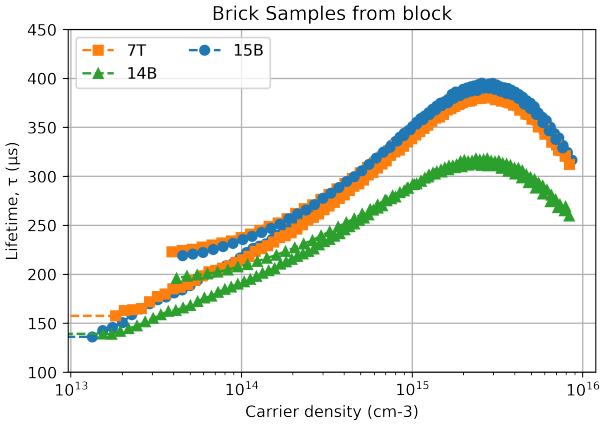


**Figure 29:** Lifetime [$\mu$s] as a function of the excess carrier density [$cm^{-3}$] for the three bricks displayed in Figure 28.

### Wafers

The measurements of wafers were performed on five samples cut from the bottom and the top of the block with a thickness of 500-970 $\mu$m shown in Figure 30, and thinner wafers (not from the block) with a thickness of approximately 200 $\mu$m and 164-166 $\mu$m Figure 32. During the passivation the samples were polished, and the thin wafers experienced breakage as observed in Figure 37. The wafers were measured using the QSSPC measuring method with the 1000nm filter using the *LifeTimeWaferSoftware*. This is because the transient technique passes light of higher intensity compared to that of the quasi-steady state technique [5]. After the samples were passivated and new measurements were to be taken, a few challenges arose with the BCT-300 instrument as it was not possible to use only the transient mode. For this reason, the Generalized (1/1) mode was used. This mode uses a combination of QSSPC and PCD mode, which may have influenced the results on the passivated samples.

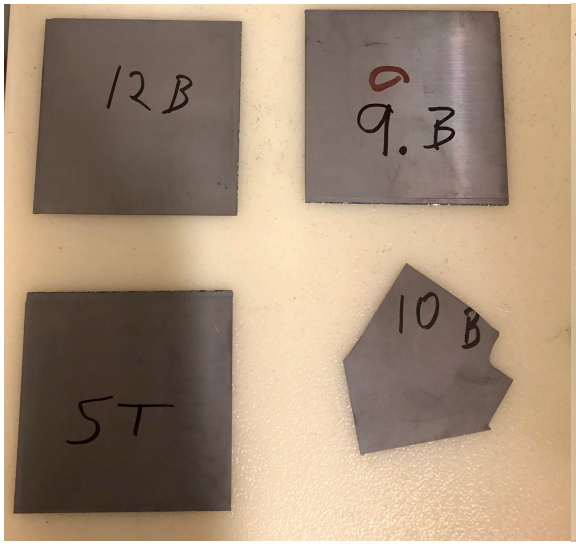


**Figure 30:** A total of 5 wafers were cut from the block.

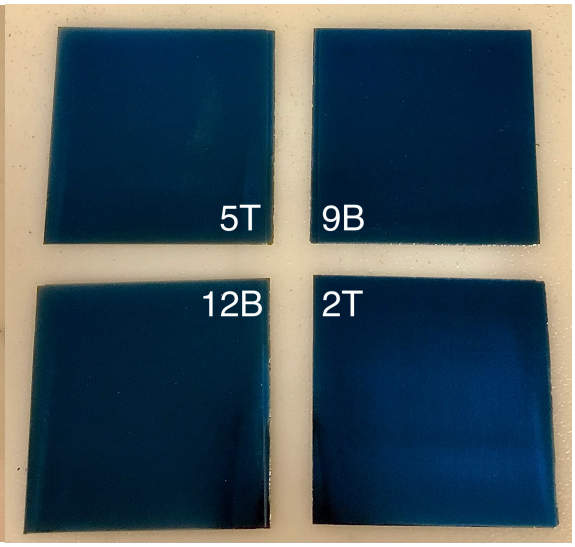


**Figure 31:** 4 out of 5 wafers in Figure 30 were passivated.

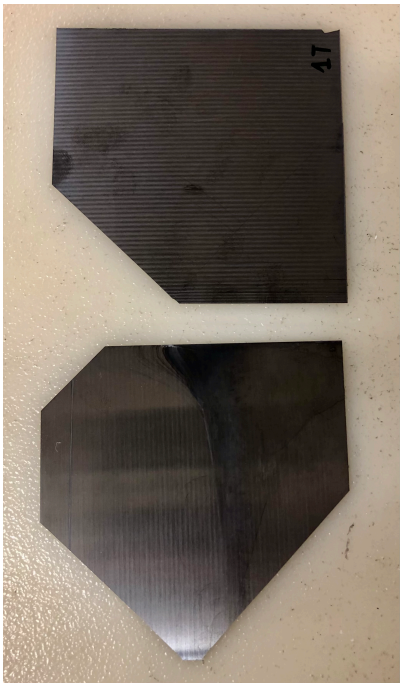


**Figure 32:** Eight samples which were not from the block was also measured.

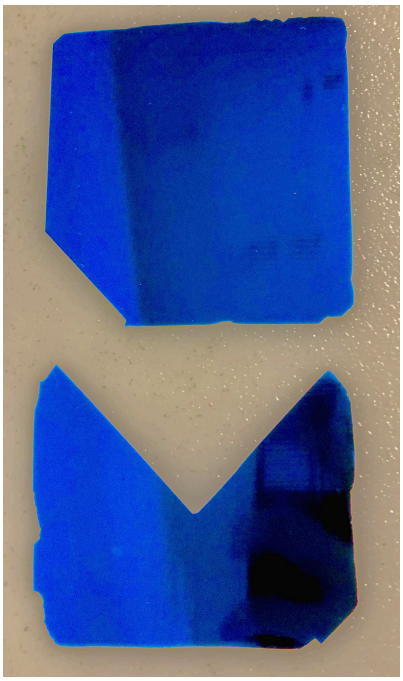

**Figure 33:** From the 8 wafers in Figure 32, six were passivated.

The lifetimes measured on the unpassivated samples (displayed in Figure 30 and Figure 32), the results obtained are illustrated in Figure 34 and Figure 36. For these samples, the lifetimes measured are very low compared to that of the brick samples in Figure 29. The observed short lifetimes can be explained through the dominant surface recombination in the wafers. This is due to the increased probability of carriers recombining at the surface, which results in a short carrier lifetime. The surface recombination depends on the wafer thickness, and this assertion is approved by Horfinyi T. S., et. al in [21] where it is stated that a thin wafer dominated by surface recombination will give shorter lifetimes. In the case of the thin wafers, the instrument is not able to detect the bulk recombination lifetime due to their thickness. However, the wafers from the block are thicker than the thin wafers, which is also approved by the longer lifetime shown in Figure 34 and Figure 36.

The results of the four wafers from the block (Figure 31) and six thin wafers (Figure 33) after passivation are displayed in Figure 31 and Figure 37. Comparing these to before passivation, the passivated wafers exhibit longer lifetimes and higher carrier densities. This is because passivation allows for the reduction of recombination through defects at the surface edges, which are typically the dominant recombination mechanism in unpassivated wafers. As a result, the instrument can measure the lifetime in bulk, rather than only measuring the surface recombination lifetime. This can be supported by S. Rein who previously reported that passivation increases carrier lifetimes as the lifetime is no longer dependent on the recombination rate at the surface [6]. Also investigating the efficient carrier lifetime in Equation 10, the surface recombination term can be neglected after passivation as it becomes equal to zero. This results in the bulk recombination lifetime being the only recombination lifetime that affects the lifetime shown in Equation 18, resulting in higher lifetimes measured.

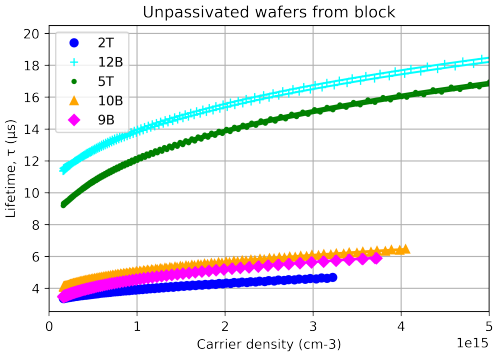


**Figure 34:** Lifetime [$\mu$s] as a function of the excess carrier density [cm$^{-3}$] for the five wafers displayed in Figure 30.

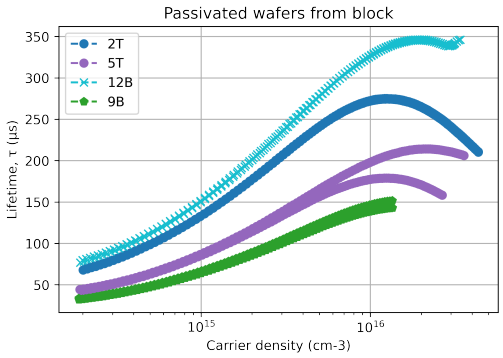


**Figure 35:** Lifetime [$\mu$s] as a function of the excess carrier density [cm$^{-3}$] for the four passivated wafers from the block displayed in Figure 31.

Figure 34 display the measures obtained for the five wafers cut from the block. It is observed different lifetimes for all of the measured wafers where 2T shows the lowest measured lifetime and 12B the highest. From the lifetime measurement through the block in Figure 26, the samples cut from the top were expected to have a shorter lifetime compared to the bottom-cut samples. In this case, however, there are also thickness variations in the wafers where 12B (968 $\mu$m) and 5T (970 $\mu$m) are the thickest samples and 9B (557 $\mu$m), 10B (555 $\mu$m), and 2T (500 $\mu$m) are the thinnest. The thickness variation is observed in the figure as the samples with the largest thickness also show the longest lifetimes and vice versa for the thinnest wafers. For the three thinner wafers from the block (9B, 10B, and 2T) it is observed that the bottom-cut samples have a higher lifetime than the sample cut from the top, which was expected.

The results from lifetime measurements on the four passivated wafers from the block are displayed in Figure 35. 12B and 2T are the wafers that show the longest lifetimes, and 5T and 9B have the shortest lifetimes. The reason for this change can be attributed to the quality of passivation or the measurement mode. It demonstrates a positive correlation between the carrier lifetime and injection level. This trend can be attributed to the reduction of recombination through defects in the material at higher carrier densities. As the carrier density increases, more defect states are filled, thereby reducing the likelihood of recombination [2]. A higher carrier density also means a higher probability for carriers to recombine, which is why the lifetimes are seen to decrease at high carrier density. From Equation 17 it can also be seen that with an increase in excess carrier density, the surface recombination rate will decrease which generally results in longer lifetimes.

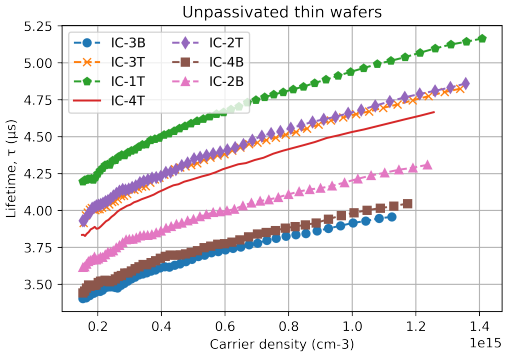


**Figure 36:** Lifetime [$\mu$s] as a function of the excess carrier density [cm$^{-3}$] for the 8 thin wafers displayed in Figure 32.

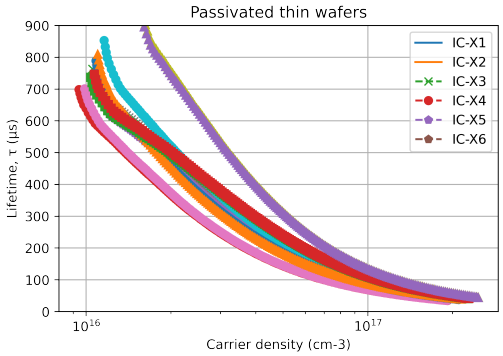


**Figure 37:** Lifetime [$\mu$s] as a function of the excess carrier density [cm$^{-3}$] for the six passivated thin wafers displayed in Figure 37.

Figure 36 displays the results obtained during lifetime measurements on the unpassivated thin wafers (Figure 32). The overall trend observed is an increase in the lifetime with increasing carrier density, which is the same trend observed for the five wafers from the block. Also, the wafers noted T are generally seen to have a higher lifetime compared to the wafers noted with a B. The variations between the samples may have been caused by different boron concentrations in the position of the sample where the lifetime was measured. These wafers were also very brittle so most of them had broken which may have affected the results. As these samples were thin and not passivated, a short lifetime was expected.

The lifetime measurements on the passivated thin samples (Figure 33) displayed in Figure 37 show a general trend where the carrier lifetime decreases as a function of increasing carrier density. This trend can be attributed to an increase in the concentration of defects and impurities in the wafer. Additionally, as the carrier density increases, the probability of recombination also increases, leading to a decrease in carrier lifetime as seen in the figure. It is noteworthy that the carrier lifetime after passivation is significantly longer compared to the lifetime before passivation (Figure 36). The reason for this increase in lifetime after passivation is that unpassivated samples have a layer where photogenerated carriers are not collected due to the high surface recombination, as stated in Section 2.5. The high surface recombination results in short lifetimes. Through passivation, the carriers are prevented to reach the surface and recombining which reduces the surface recombination velocity at the surface and increases the carrier lifetime.

# 6 Conclusion and further work

## 6.1 Conclusion

In this project, the resistivity and lifetime of silicon wafers and bricks were investigated. Through the experimental work, a comprehensive understanding of the Jandel 4PP instrument and the BCT-300 was obtained. The results of this study enabled the investigation and discussion of the thickness dependence on lifetime and the effect of passivation.

The findings from the lifetime measurements demonstrated that passivated samples displayed a significantly higher lifetime in comparison to unpassivated samples. This was due to the fact that the surface recombination rate was reduced through passivation. The results indicated that passivating silicon wafers are crucial for improving the conversion of solar energy into electrical energy.

The obtained resistivity and sheet resistance values were crucial for achieving high-quality calibration, which is fundamental for accurate lifetime measurements. It was determined that the BCT-300 had limitations in measuring resistivity above 20 $\Omega \cdot$ cm and that the 4PP yielded more precise results for all wafers measured.

The thickness dependence on the measured lifetime was mainly prominent in the unpassivated samples as the thin wafers showed a low lifetime, whilst the bricks and the block demonstrated a longer lifetime. The reason for the short lifetimes measured on the unpassivated samples is related to the thickness influence on the surface recombination rate. The results obtained indicate that as the thickness increases the effect of surface recombination becomes less relevant. This can be attributed to Equation 10, where it is seen that the surface recombination lifetime term decreases with increasing sample thickness. After passivation, the surface recombination term can be set to zero, which results in higher measured carrier lifetimes in the samples.

## 6.2 Further work

Based on the findings of this study, further investigation into the effects of temperature on carrier lifetime in both passivated and unpassivated samples with varying thicknesses would be of interest. This would provide insight into the thermal stability of the material and the temperature coefficient of resistance. Additionally, examining how bulk lifetime and surface recombination lifetime vary with wafer thickness would also be valuable. Furthermore, utilizing lifetime spectroscopy to characterize and identify defects in the material through the examination of recombination mechanisms would be a valuable avenue for future research.

# Bibliography


[1] *World Energy Outlook 2022 – Analysis - IEA — iea.org*. https://www.iea.org/reports/world-energy-outlook-2022. [Accessed 12-Jan-2023].

[2] J. Nelson. *The physics of solar cells*. World Scientific Publishing Company, 2003.

[3] Energy.gov. *Solar Photovoltaic Cell Basics*. URL: https://www.energy.gov/eere/solar/solar-photovoltaic-cell-basics. (accessed: 30.11.2022).

[4] R. A. Sinton, A. Cuevas and M. Stuckings. 'Quasi-steady-state photoconductance, a new method for solar cell material and device characterization'. In: *Conference Record of the Twenty Fifth IEEE Photovoltaic Specialists Conference-1996*. IEEE. 1996, pp. 457–460.

[5] Sinton Insturments Sinton R. A. *BCT-400/BLS-I Photoconductance Lifetime Tester User Manual*. English. Version V5.5. Sinton Instruments. 2016. 67 pp. Boulder, USA.

[6] S. Rein. *Lifetime spectroscopy: a method of defect characterization in silicon for photovoltaic applications*. Vol. 85. Springer Science & Business Media, 2006.

[7] WTRW Shockley and WT Read Jr. 'Statistics of the recombinations of holes and electrons'. In: *Physical review* 87.5 (1952), p. 835.

[8] R. N. Hall. 'Electron-hole recombination in germanium'. In: *Physical review* 87.2 (1952), p. 387.

[9] H. Nagel, C. Berge and A. G. Aberle. 'Generalized analysis of quasi-steady-state and quasi-transient measurements of carrier lifetimes in semiconductors'. In: *Journal of Applied Physics* 86.11 (1999), pp. 6218–6221.

[10] rscSiliconElement. *Silicon - Element information, properties and uses*. https://www.rsc.org/periodic-table/element/14/silicon. [Accessed 30-Dec-2022].

[11] Energy.gov. *Solar Photovoltaic Cell Basics*. https://www.energy.gov/eere/solar/solar-photovoltaic-cell-basics. [Accessed 30-Dec-2022].

[12] K. Mertens. *Photovoltaics: fundamentals, technology, and practice*. John Wiley & Sons, 2018.

[13] D. K. Schroder. *Semiconductor material and device characterization*. John Wiley & Sons, 2015.

[14] F. M Smits. 'Measurement of sheet resistivities with the four-point probe'. In: *Bell System Technical Journal* 37.3 (1958), pp. 711–718.

[15] R. A. Sinton and A. Cuevas. 'Contactless determination of current–voltage characteristics and minority-carrier lifetimes in semiconductors from quasi-steady-state photoconductance data'. In: *Applied Physics Letters* 69.17 (1996), pp. 2510–2512.

[16] R. L. Mattis and A. J. Baroody. *Carrier lifetime measurement by the photoconductive decay method*. Vol. 13. US Department of Commerce, National Bureau of Standards, 1972.

[17] *What Is Wafer Etching? — waferworld.com*. https://www.waferworld.com/post/what-is-wafer-etching. [Accessed 31-Jan-2023].

[18] *- Division of Research Safety — Illinois — drs.illinois.edu*. https://www.drs.illinois.edu/Page/SafetyLibrary/PiranhaSolutions. [Accessed 31-Jan-2023].

[19] MDC Materials Development Corp. SA. *Cylindrical Four Point Probe Head*. URL: https://www.mdc-europe.com/mdc-equipments/cylindrical-four-point-probe-head/. (accessed: 15.12.2022).

[20] C. Berthod, S. T. Søndergaard and J. O. Odden. 'Experimental investigation of the optimal ingot resistivity for both the cell performances and the temperature coefficients for different cell architectures'. In: *2018 IEEE 7th World Conference on Photovoltaic Energy Conversion (WCPEC)(A Joint Conference of 45th IEEE PVSC, 28th PVSEC & 34th EU PVSEC)*. IEEE. 2018, pp. 0293–0297.

[21] T. S. Horanyi, T. Pavelka and P. Tüttö. 'In situ bulk lifetime measurement on silicon with a chemically passivated surface'. In: *Applied Surface Science* 63.1-4 (1993), pp. 306–311.

# Appendix

| FPP Correction Factors for Sample Thickness t | | FPP Correction Factors for sample diameter d | |
|---|---|---|---|
| t/s | $C_1$ (t/s) | d/s | $C_2$ (d/s) |
| 0.3 | 1.0000 | 10 | 4.1712 |
| 0.4 | 0.9995 | 20 | 4.4364 |
| 0.5 | 0.9974 | 30 | 4.4892 |
| 0.6 | 0.9919 | 40 | 4.5080 |
| 0.7 | 0.9816 | 50 | 4.5167 |
| 0.8 | 0.9662 | 60 | 4.5215 |
| 0.9 | 0.9459 | 70 | 4.5244 |
| 1.0 | 0.9215 | 80 | 4.5262 |
| 1.2 | 0.8643 | 90 | 4.5275 |
| 1.4 | 0.8026 | 100 | 4.5284 |
| 1.6 | 0.7419 | 200 | 4.5314 |
| 1.8 | 0.6852 | □ | 4.5320 |
| 2.0 | 0.6337 | | |

**Figure 38:** 4PP correction factors based on sample thickness or diameter

# D - RISK ANALYSIS

# **RISK ASSESSMENT** (RiskManager alternative)

| | |
|---|---|
| **Unit/Institute:** | IMA |
| **Responsible line manager (name):** | Ida Westermann |
| **Responsible for activities being risk assessed (name):** | Vilma Kristiansson |
| **Participants in the risk assement (names):** | Marisa Di Sabatino Lundberg, Alfredo Sanche |

| **Description of the activity, process, area, etc.:** |
|---|
| The risk assessment applies to the activities related to the project work at the "MEKA guidelines for the instrument are given in the manual. As the instrument meets all th hazard, hot instruments and tools, and cabinets containing chemicals. None of these |

| **Activity / process** | **Unwanted incident** |
|---|---|
| Use of computer | Fire due to DAC misplaced and put on top of |
| Use of BCT instrument | Eye injury due to bright light |
| Use of lab | Fall acident due to little space |
| Use of Peltier element | Burn injury due to warm heat plate |

ez Garcia

ANISK LAB" (Room nr. E-112). The purpose of the experimental work is to measure the lifetime c
e given guidelines, it is safe to use and does not represent a risk. The work will be conducted or
apply to the planned lab work and, therefore, are not considered as part of the risk assessment

| **Existing risk reducing measures** | **Probability (P)** | **Consequence (C)** Evaluate the categories individualley. *He always be evaluated.* | | |
|---|---|---|---|---|
| | (1-5) | Health (1-5) | Material values (1-5) | Environment (1-5) |
| DAC is put on top of the computer (plas | 1 | 3 | 3 | 3 |
| Do not take the instrument apart and lo | 1 | 4 | 0 | 0 |
| Be cautious | 1 | 1 | 3 | 0 |
| Heat glowes for removing samples from the heat plate and tweezers to move samples | 1 | 1 | 0 | 0 |

| | |
|---|---|
| **Date:** | 01.02.2023 |
| **Revised:** | |

of silicon ingots by using the instrument BCT-400 Photoconductance Lifetime Tester. Safety
nly at the “Mekanisk lab”. The room card of the lab states different risks such as crushing
t for this project.

| *alth should* Reputation (1-5) | **Risk value (P x C)** | **Risk reducing measures - suggestions** Measures reducing the probability of the unwanted incident happening should be prioritized. | **Residual risk after measures being implemented (S x K)** |
|---|---|---|---|
| 1 | 3 | Do not move the DAC | 3 |
| 1 | 4 | Do not take the instrument apart and look into the lightbulb | 4 |
| 0 | 1 | Be cautious while walking around in the lab | 1 |
| 0 | 1 | Be cautions and use the extra tools available | 1 |

| | | Health | Material values | Reputation | Env |
|---|---|---|---|---|---|
| **Grade** | 1 | Minor injury/strain that requires simple treatment. Reversible injury. Short recovery time. | Operational shutdown, or shutdown of activities <1 day. | Little effect on credibility and respect. | Neg inju sho tim |
| | 2 | Injury/strain that requires medical treatment. Reversible injury/strain. Short recovery time. | Operational shutdown, or shutdown of activities <1 week. | Negative effect on credibility and respect. | Mir and rec |
| | 3 | Serious injury/strain that requires medical treatment. Lengthy recovery time. | Operational shutdown, or shutdown of activities <1 month. | Reduced credibility and respect. | Mir and rec |
| | 4 | Serious injury/strain that requires medical treatment. Possible disability /permanent disability. | Operational shutdown > 1/2 year. Shutdown of activities up to 1 year. | Credibility and respect considerably reduced. | Lor inju rec |
| | 5 | Death or disability / permanent disability. | Operational shutdown, or shutdown of activities >1 year. | Credibility and respect considerably and permanently reduced. | Ver last irre inju |

| vironment |
|---|
| gligible<br>ury and<br>ort recovery<br>ne. |
| nor injury<br>d short<br>overy time. |
| nor injury<br>d lengthy<br>overy time. |
| ng-lasting<br>ury. Lengthy<br>overy time. |
| ry long-<br>ting and<br>eversible<br>ury. |

**Risikoverdi = Sannsynlighet x Konsekvens:**

| KONSEKVENS | | | | |
|---|---|---|---|---|
| | 5. Svært alvorlig | 5 | 10 | 15 |
| | 4. Alvorlig | 4 | 8 | 12 |
| | 3. Moderat | 3 | 6 | 9 |
| | 2. Liten | 2 | 4 | 6 |
| | 1. Svært liten | 1 | 2 | 3 |
| | | 1. Svært liten | 2. Liten | 3. Middels |
| | | SANNSYNLIGHET | | |

| | |
|---|---|
| Red | Unacceptable risk. Measures needs to be implemented. |
| Yellow | Medium risk. Measures needs to be considered. |
| Green | Acceptable risk. Measures can be considered. |

| | | |
|---|---|---|
| | 20 | 25 |
| | 16 | 20 |
| | 12 | 15 |
| | 8 | 10 |
| | 4 | 5 |
| | 4. Stor | 5. Svært stor |

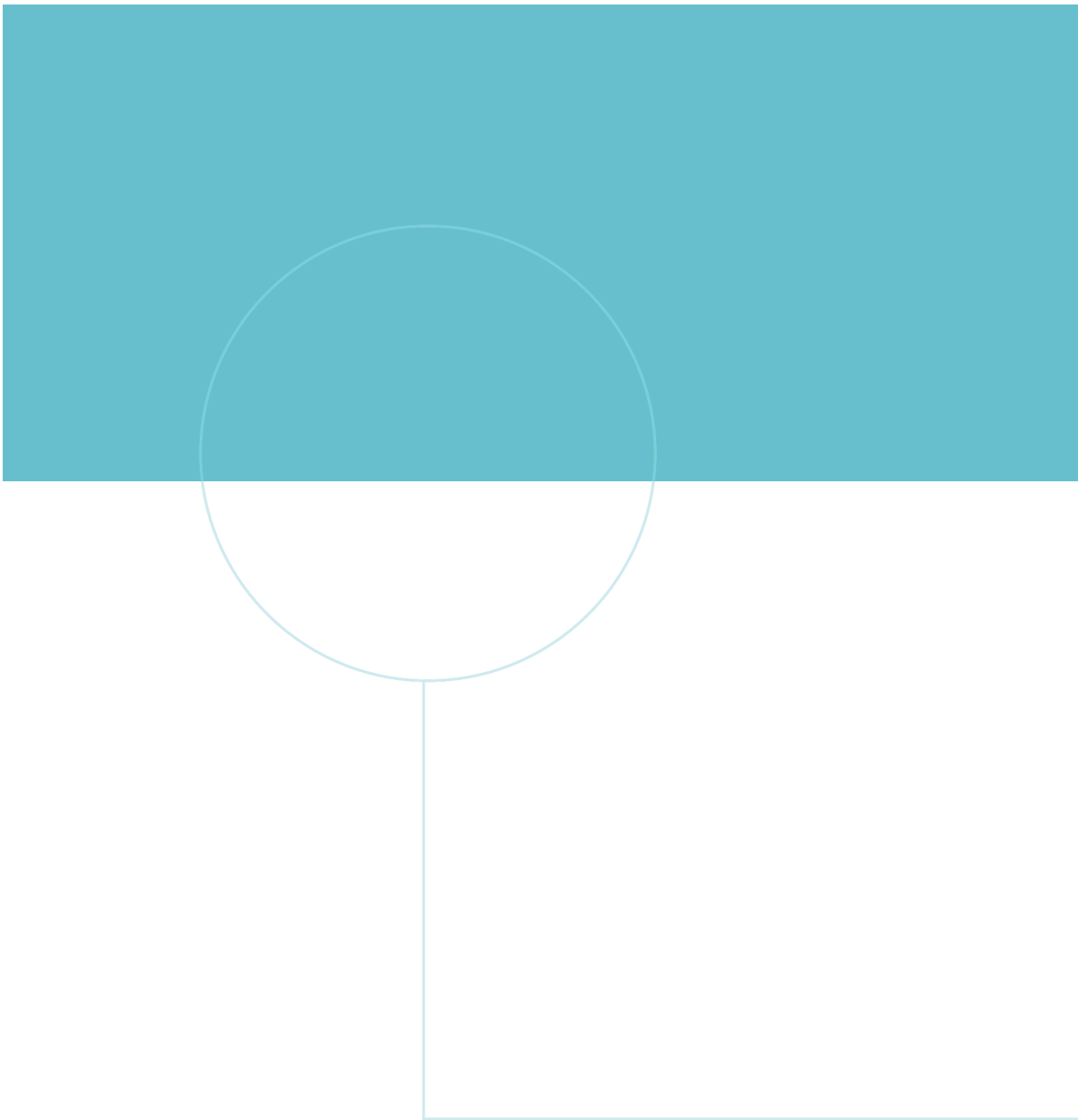

NTNU

Norwegian University of
Science and Technology